# Ion-selective microelectrode arrays for cell culture monitoring

Thèse présentée à la Faculté des Sciences
Institut de Microtechnique
Université de Neuchâtel

Pour l'obtention du grade de *docteur ès sciences*

par

Silvia Generelli

Accepte sur proposition du jury:
Prof. N. F. de Rooij, directeur de thèse
Prof. M. Koudelka-Hep
Prof. J.-F. Dufour
Prof. O. T. Guenat
Dr. P. D. van der Wal

Soutenue le 7 mars 2008

Université de Neuchâtel unine

FACULTE DES SCIENCES
Secrétariat-Décanat de la faculté
- Rue Emile-Argand 11
- CP 158
- CH-2009 Neuchâtel

# IMPRIMATUR POUR LA THESE

## Ion-selective microelectrode arrays for cell culture monitoring

**Silvia GENERELLI**

UNIVERSITE DE NEUCHATEL

FACULTE DES SCIENCES

La Faculté des sciences de l'Université de Neuchâtel,
sur le rapport des membres du jury

Mme M. Koudelka-Hep,
MM. N. de Rooij (directeur de thèse),
P. van der Wal, O. Guenat (Montréal)
et J.-F. Dufour (Berne)

autorise l'impression de la présente thèse.

Neuchâtel, le 20 mars 2008

Le doyen :
F. Kessler

UNIVERSITE DE NEUCHATEL
FACULTE DES SCIENCES
Secrétariat - décanat de la faculté
Rue Emile-Argand 11 - CP 158
CH-2009 Neuchâtel
Felix Kessler

# Abstract

**Keywords: silicon, micropipettes, ion-selective microelectrodes, *in vitro*, $K^+$, $Ca^{2+}$, cell death, lysis, electroporation.**

The design, microfabrication and characterization of a platform comprising an array of ion-selective microelectrodes ($\mu$ISE) aimed at *in vitro* cellular physiology and toxicology is described.
This study focusses on $K^+$ and $Ca^{2+}$ monitoring in cell culture environments. A potential promising application of such a platform is based on recent findings in molecular biology, revealing connections between certain diseases, as for example some types of cancer or parkinsonism, and a malfunction in cellular ion fluxes.

The silicon microfabrication of the platform allowed the realization of ion-selective microelectrode arrays comprising 16 electrodes with diameters ranging from 1.5 $\mu$m to 6 $\mu$m, and an interelectrode gap of 150 $\mu$m or 300 $\mu$m. The $\mu$ISE, inspired by the classical glass capillary microelectrodes, are based on a micropipette-like channel which, in two of the three realized geometries, protrude for 5 $\mu$m from the surface and are located in a 350 $\mu$m deep cavity. In the third geometry, the micropipettes are non-protruding, completely embedded in the silicon substrate. This planar platform allowed the implementation of an array of $K^+$-selective electrodes combined with planar platinum electrodes. The metallic electrodes placed near the ion-selective electrodes are designed for the application of electrical pulses for localised electroporation of cells. Preliminary tests showed the feasibility of localised electropo-

ration, and demonstrated that the application of several electroporation pulses does not affect the functionality of $K^+$-selective microelectrodes, however further investigation is necessary to optimize the electroporation protocol.

The characterization of the electrodes in physiological concentration ranges was performed using electrodes of 1.5 $\mu$m diameter in contact with simple buffer calibration solutions. The observed detection limits, $10^{-5}$ M for the $K^+$-selective electrodes and $10^{-9}$ M for the $Ca^{2+}$-selective electrodes, demonstrated that the $\mu$ISE are adapted for the use in cell culture concentration ranges. The functional lifetime of the sensors, when conditioned in $10^{-3}$ M KCl, or $10^{-4}$ M $CaCl_2$ respectively, varied from 30 to 45 days for $K^+$-selective electrodes, but is limited to 1 to 3 days for $Ca^{2+}$-selective electrodes. This difference in the functional lifetimes of $K^+$- and $Ca^{2+}$-selective electrodes is due to the use of calcium-selective sensors in their non-equilibrium state. After several days of use the calcium detection limit rises to the micromolar range, which is adapted for extracellular calcium concentrations, but not for intracellular monitoring. In this case, the lifetime of the sensors is comparable to those of $K^+$-selective microelectrodes.

Tests performed in presence of culture medium showed a drastic diminution of the electrodes lifetime down to several days. On the other hand, a short-time contact of the sensors with the cells or cellular debris does not affect their functional characteristics. A short-time *in vitro* test was thus used to verify the possibility of identification of cell necrosis. Cell death, induced by a hypoosmotic shock, was successfully followed in real time by monitoring the intracellular potassium release in the culture medium. The $\mu$ISE also allowed to quantify the necrotic cells, opening interesting possibilities in toxicological screening.
Further development of this technique might lead to monitoring of early stage apoptosis. The observation of apoptosis before the process becoming irreversible, causing the death of the cell, could bring new information on the physiology of the cell cultures.

# Contents

# List of Figures

# List of Tables

# Chapter 1

# Introduction

The development of new drugs is an extremely costly process which, for this reason, is mainly dominated by a few big pharmaceuticals companies. However, in the past decade, the situation of the pharmaceutical industry has changed: the predominance of big pharmaceutical companies is lowering, particularly because of the end of the long-term exclusivity patents on the so-called "blockbuster drugs", generating more than 1 billion dollars revenues per year. These drugs are the largest source of benefit for the pharmaceutical industry, and the end of the protection by patents leads to a loss of large and lucrative market segments. To find new potential blockbuster drugs, the research and development investment of the pharmaceutical industry has constantly increased over the last decade. In spite of these efforts, the success rate in identifying new therapeutic compounds remains rather low [1]. One of the main causes of this slowing down in drug development process has been identified to be a non effective testing phase of new potential therapeutics. This is especially the case of the efficacy and toxicity testing which is still largely performed in parallel by *in vivo* studies. This process is costly and time expensive. The efficacy and toxicity evaluations are usually performed during two distinct phases: drug discovery and preclinical drug development. Figure 1.1 illustrates a typical testing sequence followed in pharmaceutical industry. This division of the efficacy and toxicity eva-

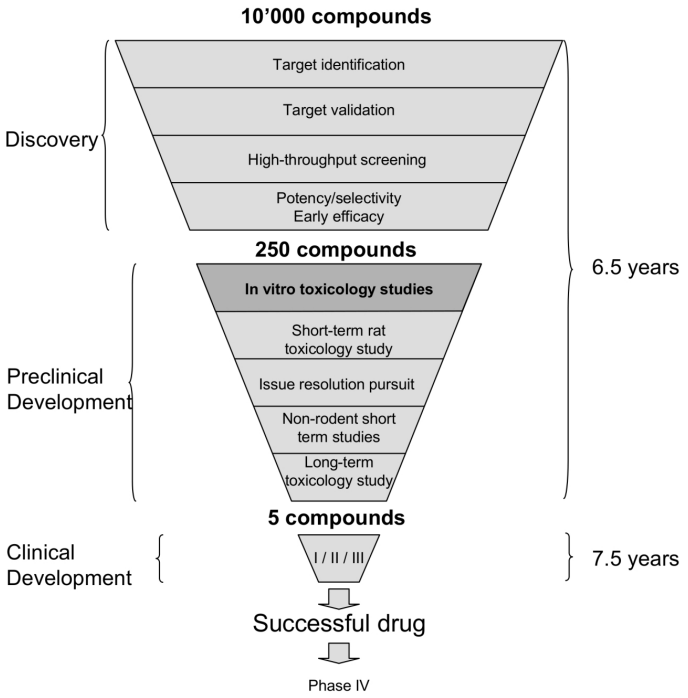


Figure 1.1: A prototypical pharmaceutical testing funnel. In the U. S. over 10'000 potential therapeutic compounds, only one is expected to be approved as a drug by the Food and Drug Administration. Figure adapted from [1] and [2].

luations result in a large number of compounds entering the preclinical study to fail due to their toxicity [2].

To render this process more cost- and time-effective requires a parallel evaluation of efficacy and toxicity in a high throughput *in vitro* toxicology assay format. Such assays allowing the physical/chemical efficacy, metabolic stability and toxicity to be assessed would greatly facilitate and accelerate the identification of the best candidates within the most promising chemical classes.

It can be noted that the need for new high throughput instruments for efficacy/toxicology tests is not limited to the pharmaceutical industry. The European Community has recently introduced a new set of regulations on chemical safety. The new REACH regulation, entered into force in June 2007, requires manufacturers and importers to provide information on the safe handling of their chemical substances [3]. The former global standard, the "Toxic Substances Control Act", edited by the U. S. in 1976, required testing on human and environmental toxicity only for chemicals introduced on the U. S. market after 1979. This corresponded to 30'000 compounds on the U. S. market for which only minimal toxicological characterization has been performed [4]. With the REACH regulation the number of compounds to be tested has greatly increased.

Toxicity tests are, to date, largely based upon well established markers or pathologies, however often with limited understanding of mechanisms involved [2]. Moreover, only 70% of the *in vivo* toxicology results in preclinical toxicological species had true positive rate for predicting human toxicity [2]. This highlights a second, and more fundamental problem: the lack of knowledge on the relation between disease and cellular mechanisms. Very little is known about intra- and intercellular mechanisms, continuously new roles and pathways for compounds known since decades are discovered. A striking example is that of Na,K-ATPase enzyme, a $Na^+$-$K^+$ transmembrane pump, discovered in 1957 by the Nobel prize winner Jens Christian Skou [5]. It is only very recently that new roles of this pump in the modulation of growth, apoptosis, cell adhesion and motility have been demonstrated [6]. A 2006 report of the United States Government Accountability Office on the trends in pharmaceutical industry research and development stating that the "lack of scientific understanding in treating diseases contributes to increased failure rates and increased research and development expenditures" [1], indicates very clearly this problem.
The development of toxicological platforms that would provide, next to the toxicity tests, also information on the cellular mechanisms involved are thus of great importance for an efficient high throughput screening of multiple potential drugs candidates, for enhancing the understanding of the mechanisms of diseases and consequently for improving their treatment.

## 1.1 $K^+$ and $Ca^{2+}$ sensing in biology

$K^+$ and $Ca^{2+}$ are ionic species having a particularly important biological role, and thus have been chosen as target analytes.

### Potassium

Potassium is a key ion involved in cell proliferation and progression through the cell cycle. The interest of potassium monitoring is mainly related to the role of potassium channels and pumps in cellular signalling processes [7]. Recent studies have highlighted relationships between ion channels and cancer [8]. Examples are breast cancer cells, presenting deregulated potassium fluxes. The study of ion fluxes can be a valuable method to find new targets for regulation or inhibition of ion channels for cancer cure [8].

Direct continuous visualization of $K^+$ fluxes is performed by the use of radioactive tracers as $^{42}K$, $^{86}Rb$ [9, 10, 11]. $K^+$-selective electrodes, were extensively used in physiological studies during the years 1970s and 1980s. Then, the patch clamp technique and other methods for the study of ion channels and pumps were preferred and found a wide application in the field. Glass capillary ion-selective microelectrodes are still used in physiological research, but in a less widespread way (some examples of recent publications: [12, 13, 14]). Spectroscopic techniques, as flame photometry, absorption spectroscopy or fluorescence spectroscopy by a fluorescent $K^+$ indicator are mainly used for dosage of potassium, for example in cell supernatant and in cell lysate, and are not used for continuous monitoring [15, 16].
Potassium fluxes are mainly observed indirectly, by following the dynamics of $K^+$ channels and pumps, targeted with fluorescent tags [17], or by patch clamp techniques. Patch clamp allows the recording of electrical current carried by the totality of the ion channels present in the cell membrane. Activation (or inhibition) of a specific ion channel or pump allows the identification of the electrical current generated by the flux of a specific ionic species. The use of artificial lipid bilayers or vesicles loaded with a specific ion channel allows the ion channel dynamics to

be studied down to the single channel. To discriminate potassium fluxes from other ions fluxes, glass capillary ion-selective electrodes have been used in parallel with patch clamp [14].

### Calcium

Calcium is a messenger regulating many diverse cellular processes, as fertilization, secretion, contraction, proliferation, neural signalling and learning. Cellular calcium signalling has been extensively described [18, 19, 20, 21]. Even if characteristics of this signalling have already been determined, such as for example the intracellular concentration ranges, from 10 nM to 1 $\mu$M, the duration, amplitude, spatio-temporal aspects [18, 22, 23], the exact mechanism of $Ca^{2+}$ role in cellular communication is still to be discovered. Some of the very recent reviews on calcium signalling report research on seizure-induced neuronal epilepsy [24], immune system diseases [25], asthma [26], early embryonic development [27], cardiac arrhythmias [28], cancer [29], demonstrating the universality of calcium signalling, and its importance in disease mechanisms. This makes $Ca^{2+}$ ion a target of choice of intercellular communication studies.

The use of the radioactive tracer $^{45}Ca^{2+}$ for the direct monitoring of calcium fluxes has been reported, but this method is not widely applied [30]. Glass capillary ion-selective microelectrodes have been in the past a valuable tool to measure intracellular calcium activities [23], but the advent of fluorescence has lead to the partial abandon of alternative techniques for calcium monitoring in cell cultures.
Direct calcium visualization is possible by fluorescent markers extremely sensitive in the intracellular concentration range, as for example fura-2 [31]. Indirect fluorescence techniques to visualize calcium use fluorescent calcium-sensitive proteins, as aequorin or compounds based on the green fluorescent protein [31]. Quantum dot bioconjugates are promising compounds for application in fluorescence spectroscopy [32]. Quantum dots used in fluorescence imaging are metallic nanoparticles with emission spectra related to their size. In principle, they could be associated with any biological marker, and thus have a wide spectrum of potential applications.

Relations between signalling pathways and calcium have also been followed by patch clamp techniques [30].

## 1.2 Requirements for an ion-sensing platform for cell culture monitoring

### 1.2.1 Detection limit and selectivity: the cellular concentration ranges

Cellular electrolytes concentration and activity ranges in cellular environment are reported in table 1.1.
Free calcium intra- and extracellular activities are very different: in the millimolar range in extracellular space, and in the sub-micromolar range in the cytosol. Ion-selective electrode are thus particularly adapted to the monitoring of calcium activities, due to the large activity range covered, going from $10^{-10}$ M to $10^{-1}$ M $Ca^{2+}$. The needed dynamic range for the potassium ion is less demanding, and is comprised between $10^{-4}$ M and $10^{-1}$ M.

Table 1.1: Intra- and extracellular concentration and activity ranges [23].

| Ion | Concentration [M] | Activity [M] |
|---|---|---|
| *Extracellular* | | |
| $Na^+$ | 0.135 - 0.150 | 0.102 - 0.112 |
| $K^+$ | $3.5{\cdot}10^{-3}$ - $5{\cdot}10^{-3}$ | $2.6{\cdot}10^{-3}$ - $3.7{\cdot}10^{-3}$ |
| $Mg^{2+}$ | $4.5{\cdot}10^{-4}$ - $8{\cdot}10^{-4}$ | $1.6{\cdot}10^{-4}$ - $2.8{\cdot}10^{-4}$ |
| $Ca^{2+}$ | $1{\cdot}10^{-3}$ - $1.2{\cdot}10^{-3}$ | $3.4{\cdot}10^{-4}$ - $4.1{\cdot}10^{-4}$ |
| $H^+$ | $4.3{\cdot}10^{-8}$ - $5.6{\cdot}10^{-8}$ | $3.34{\cdot}10^{-8}$ - $4.35{\cdot}10^{-8}$ |
| *Intracellular* | | |
| $Na^+$ | $5{\cdot}10^{-3}$ - $18{\cdot}10^{-3}$ | $3.8{\cdot}10^{-3}$ - $14{\cdot}10^{-3}$ |
| $K^+$ | $8{\cdot}10^{-2}$ - $16{\cdot}10^{-2}$ | $61{\cdot}10^{-3}$ - $116{\cdot}10^{-3}$ |
| $Mg^{2+}$ | $1{\cdot}10^{-3}$ - $5{\cdot}10^{-3}$ | $4{\cdot}10^{-4}$ - $1.8{\cdot}10^{-3}$ |
| $Ca^{2+}$ | $5{\cdot}10^{-8}$ - $2.5{\cdot}10^{-6}$ | $1.7{\cdot}10^{-8}$ - $8.7{\cdot}10^{-7}$ |
| $H^+$ | $6{\cdot}10^{-8}$ - $8{\cdot}10^{-8}$ | $4.7{\cdot}10^{-8}$ - $6.2{\cdot}10^{-8}$ |

The activities are calculated from the corresponding concentrations, with ionic strength of I=0.149 M for extracellular medium and I=0.139 M for intracellular medium (see section 3.2.3).

### 1.2.2 Response time

Calcium oscillations in non-excitable cells have been observed for the first time in 1986, when injecting aequorin, a fluorescent protein binding to $Ca^{2+}$, in liver cells [33]. The calcium signalling can transmit different information, the modulation of the information is obtained by frequency and amplitude modulation [21]. Calcium signalling can take the form of waves that propagate through the cell, and even through a whole tissue. The two major kinds of intracellular calcium oscillations, baseline transients and sinusoidal oscillations [22, 34], have a decay time in the order of minutes. So, to follow these signals, the sensors should have a response time in the order of seconds to dozens of seconds.
Targeted potassium concentration changes are related to cell death. In this case, the timescale is not so stringent, and can be in the order of dozens of seconds to minutes.

### 1.2.3 Lifetime

Physiological assays would require a lifetime of the platform going from several hours to a few days, depending on the system studied. As the cell culture grows continuously, the timescale of the test is limited by the duration of the cell cycle. Toxicological studies are performed on a relatively short timescale, of several minutes to hours.

### 1.2.4 Multi-point measurements

Metallic electrode arrays are widely used tools in electrophysiology for the recording of electrical signals (action potentials) in electrogenic cells, as for example neurones. Action potentials (see for example [35]), are caused by an exchange of ions across the cell membrane. Using ion-selective electrodes instead of metallic electrodes, would allow discriminating for the contribution of a single ion to the overall signal. Moreover, ionic fluxes in non electrogenic cells can be followed.
An array configuration of the ion-selective electrodes would allow the recording of the ionic activities at different points of the cellular culture, to obtain a mapping of the cellular comportment over a culture network.

### 1.2.5 Cellular measurements

#### Cells on chip

The presence of biological material can lead to biofouling of the sensor surface. This is a well known issue in cell-based assays. Long term contact of biological material with the sensors should be, if possible, avoided. Short term direct on-chip culture (6-7 hours) can be considered, but in this case, the possibility of reutilization of the platform for other assays is very limited, or even impossible. If cell cultures are directly performed on-chip, the platform should also allow sterilization and the accurate control of a number of parameters such as temperature, oxygen and carbon dioxyde concentrations, the composition of the culture medium.
Another option for measurements on a whole cell culture is to perform the cultures on a substrate that will be placed in contact with the sensor platform only during the time of the assay. The culture medium would be in this case replaced by a simple electrolyte solution, minimizing the biofouling problem. If accurate cell positioning is needed, the cells can be patterned by dielectrophoretic forces, using metallic microelectrodes [36], or also be trapped by a pressure difference in an array of microholes [37], patterned to match the ion sensor array design. This approach is used for example in multiple patch clamp assays, and allows parallel measurements on a population of single cells. The multiple recording sites will minimize the dispersion of results due to cell biological variability [38].
After the cell assay, elimination of the cellular debris and preparation of the platform for new measurements should be readily done, without affecting the sensors functionality.

#### Extra- and intracellular ion sensing

Cellular measurements are performed in complex cell culture media, containing many potentially interfering and fouling compounds. The contact of the sensors with the cell culture medium and/or with the cells can lead to a degradation of the signal and a shortening of the sensor lifetime.
As "true" intracellular on-chip measurements are not straightforward to

obtain, the analysis of cell lysate is widely used nowadays in lab-on-chip platforms [39]. Cells lysis can be performed by two methods: chemically, by addition of detergent like Triton X100 or SDS, or mechanically, by rupture of the membrane by shear stress, hypoosmotic shock, electrical lysis. Irreversible electroporation induces cell membrane rupture and the leakage of intracellular components without the addition of chemicals, and is consequently of particular interest. The lysis of the cells liberates the intracellular content in the surrounding medium, allowing measurements of the intracellular components.

## 1.3 Objectives and outline of the present thesis

In the present work, the development of a microfabricated ion-sensing platform aimed at *in vitro* studies, for both physiological investigation and toxicology is presented. To this aim, the glass capillary ion-selective microelectrodes technology, successfully used in the past decades for cell physiology investigation [23], has been adapted for the realization of a silicon-based platform. Ion-selective electrodes technology has been chosen because of its unique characteristic enabling a direct measurement of ionic activities, which is a physiological parameter of primary importance. The possibility to perform ionic measurements directly, locally, and without the need of markers is thus of particular interest.

To allow physiological investigation on a cell culture network, a local multi-point measurement system on the cell scale is necessary. Thus an array of micron-size silicon-based micropipette electrodes has been realized. Its fabrication is presented in detail in chapter 2. Characterization of $K^+$- and $Ca^{2+}$-selective microelectrode arrays in physiological concentration ranges, as well as several considerations on the array use in cell media are presented in chapter 3. The applicability of the platform for *in vitro* investigations, and in particular the possibility to adapt the platform for toxicology studies is presented in chapter 4. For this, we focussed on the relationship between $K^+$ cell efflux and apoptosis/necrosis [40] to identify and quantify necrotic cells. In chapter 5, the possibility

of accessing the interior of the cells, by an electroporation system or by perforated patch clamp are discussed, and some preliminary tests going in this direction are presented.

As the subjects treated in this thesis are very different, more specific introductions on each topic are provided in the corresponding chapters.

# Bibliography

[1] New drug development. Science, business, regulatory, and intellectual property issues cited as hampering drug development efforts. Technical Report GAO-07-49, United States Government Accountability Office, 2006. http://www.gao.gov.

[2] Gross C and Kramer JA. The role of investigative molecular toxicology in early stage drug development. *Expert Opin. Drug Saf.*, 2:147–159, 2003.

[3] Registration, Evaluation, Authorisation and Restriction of Chemical Substances (REACH) regulamentation, regulation (EC) No 1907/2006. Technical report, European Chemical Agency, 2006. http://www.reach-compliance.eu.

[4] Schapiro M. New power for "old Europe". *The Nation*, December 27, 2004.

[5] Skou JC. *The identification of the sodium-potassium pump*, pages 179–194. Nobel Lectures, Chemistry 1996-2000. World Scientific Publishing Co., 2003.

[6] Aperia A. New roles for an old enzyme: Na,K-ATPase emerges as an interesting grug target. *J. Internal. Med.*, 261:44–52, 2007.

[7] Shieh CC, Coghlan M, Sullivan JP, and Gopalakrishnan M. Potassium channels: molecular defects, diseases, and therapeutic opportunities. *Pharmacol. Rev.*, 52:557–593, 2000.

[8] Le Guennec J-Y, Ouadid-Ahidouch H, Soriani O, Besson O, Ahidouch A, and Vandier C. Voltage-gated ion channels, new targets in anti-cancer research. *Rec. Pat. on Anti-Cancer Drug Discov.*, 2:189–202, 2007.

[9] Junankar PR, Karjalainen A, and Kirk K. Osmotic swelling activates two pathways for $K^+$ efflux in a rat hepatoma cell line. *Cell. Physiol. Biochem.*, 14:143–154, 2004.

[10] Pesantes-Morales H, Lezama RA, Ramos-Mandujano G, and Tuz KL. Mechanisms of cell volume regulation in hypo-osmolality. *Am. J. Med.*, 119:S4–S11, 2006.

[11] Gill S, Gill R, Wicks D, and Liang D. A cell based $Rb^+$ flux assay of the Kv1.3 potassium channel. *Assay Drug Deliv. Technol.*, 5:373–380, 2007.

[12] Messerli MA, Corson ED, and Smith PJS. Measuring extracellular ion gradients from single channels with ion-selective microelectrodes. *Biophys. J.*, 92:L52–L54, 2007.

[13] Knowles A and Shabala S. Overcoming the problem of non-ideal liquid ion-exchanger selectivity in microelectrode ion flux measurements. *J. Membrane Biol.*, 202:51–59, 2004.

[14] Kang TM, Markin VS, and Higelmann DW. Ion fluxes in giant excised cardiac membrane patches detected and quantified with ion-selective microelectrodes. *J. Gen. Physiol.*, 121:325–347, 2004.

[15] Lahet JJ, Lenfant F, Courderot-Masuyer, Bouyer F, Lecordier J, Bureau A, Freysz M, and Chaillot B. Comparison of three methods for oxidative stress-induced potassium efflux measurement. *Biomed. Pharmacotherapy*, 61:423–426, 2007.

[16] Wible BA, Wang L, Kuryshev YA, Basu A, Haldar S, and Brown AM. Increased $K^+$ efflux and apoptosis induced by the potassium channel modulatory protein KChAP/PIAS3$\beta$ in prostate cancer cells. *J. Biol. Chem.*, 277:17852–17862, 2002.

[17] Beeton C, Wulff H, Singh S, Botsko S, Crossley G, Gutman CA, Cahalan MD, Pennington M, and Chandly KG. A novel fluorescent toxin to detect and investigate Kv1.3 channel up-regulation in chronically activated T lymphocytes. *J. Biol. Chem.*, 278:9928–9937, 2003.

[18] Berridge MJ, Lipp P, and Bootman MD. The versatility and universality of calcium signalling. *Nature Rev. Mol. Cell Biol.*, 1:11–21, 2000.

[19] Bootman MD, Collins TJ, Peppiatt CM, Protheo LS, MacKenzie L, De Smet P, Travers M, Tovey SC, Seo JT, Berridge MJ, Ciccolini F, and Lipp P. Calcium signalling - an overview. *Seminars Cell Develop. Biol.*, 12:3–10, 2001.

[20] Campbell AK. *Intracellular calcium, its universal role as regulator.* John Wiley and Sons, 1983. ISBN: 0-471-10488-4.

[21] Berridge MJ. The AM and FM of calcium signalling. *Nature*, 386:759–760, 1997.

[22] Thomas AP, Bird GSJ, Hajnóczki, Robb-Gaspers LD, and Putney JW. Spatial and temporal aspects of cellular calcium signaling. *FASEB J.*, 10:1505–1517, 1996.

[23] Ammann D. *Ion-selective microelectrodes, principles, design and application.* Springer-Verlag, 1986. ISBN 0-387-16222-4.

[24] Henshall DC. Apoptosis signalling pathways in seizure-induced neuronal death and epilepsy. *Biochem. Soc. Trans.*, 35:421–423, 2007.

[25] Feske S. Calcium signalling in lymphocyte activation disease. *Nature Rev. Immunol.*, 7:690–702, 2007.

[26] Hirota S, Helli P, and Janssen LJ. Ionic mechanisms and $Ca^{2+}$ handling in airway smooth muscle. *Eur. Resp. J.*, 30:114–133, 2007.

[27] Webb SE and Miller AL. $Ca^{2+}$ signalling and early embryonic patterning during zebrafish development. *Clin. Exp. Pharmacol. Physiol.*, 34:897–904, 2007.

[28] West DJ and Williams AJ. Pharmacological regulators of intracellular calcium release channels. *Curr. Pharmaceut. Des.*, 13:2428–2442, 2007.

[29] Boelens J, Lust S, Offner F, Bracke ME, and Vanhoecke BW. The endoplasmic reticulum: a target for new anticancer drugs. *In Vivo*, 21:215–226, 2007.

[30] van den Brink GJ, Bloemers, van den Blink B, Tertoolen LGJ, van Deventer SJH, and Peppelenbosch MP. Study of calcium signaling in non-excitable cells. *Microsc. Res. Tech.*, 46:418–433, 1999.

[31] Monteith GE. Seeing is believing: recent trends in the measurement of $Ca^{2+}$ in subcellular domains and intracellular organelles. *Immunol. Cell Biol.*, 78:403–407, 2000.

[32] Smith AM, Ruan G, Rhyner MN, and Nie S. Engineering luminescent quantum dots for *in vivo* molecular and cellular imaging. *Ann. Biomed. Eng.*, 34:3–14, 2006.

[33] Woods NM, Cuthbertson KS, and Cobbold PH. Repetitive transient rises in cytoplasmic free calcium in hormone-stimulated hepatocytes. *Nature*, 319:600–602, 1986.

[34] Aizman O, Uhlén P, Lal M, Brismar H, and Aperia A. Ouabain, a steroid hormone that signals with slow calcium oscillations. *PNAS*, 98:13420–13424, 2001.

[35] Morin FO, Takamura Y, and Tamiya E. Investigating neuronal activity with planar microelectrode arrays: achievements and new perspectives. *J. Biosci. Bioeng.*, 100:131–143, 2005.

[36] Voldman J. Electrical forces for microscale cell manipulation. *Annu. Rev. Biomed. Eng.*, 8:425–454, 2006.

[37] Greve F, Seemann L, Hierlemann A, and Lichtenberg J. A hybrid microsystem for parallel perfusion experiments on living cells. *J. Micromech. Microeng.*, 17:1721–1730, 2007.

[38] Finkel A, Wittel A, Yang N, Handran S, Hughes J, and Costantin J. Population patch clamp improves data consistency and success rates in measurement of ionic current. *J. Biomolec. Screening*, 11:488–496, 2006.

[39] El-Ali J, Sorger PK, and Jensen KF. Cells on chip. *Nature*, 442:403–411, 2006.

[40] Remillard CV and Yuan JJ-X. Activation of $K^+$ channels: an essential pathway in programmed cell death. *Am. J. Physiol. Lung Cell. Mol. Physiol.*, 286:L49–L67, 2004.

# Chapter 2

# Microfabrication of the ion-selective array

## 2.1 Introduction

The technological platform has been inspired by the glass micropipette-based ion-selective microelectrodes used in cell physiology investigations during the late 1970s and 1980s [1]. An array of completely independent microchannels has been realized. These are formed by micrometer size channels etched through a silicon substrate (the "micropipettes") each one connected to a microchannel etched in a Pyrex substrate. The silicon and Pyrex sub-units are assembled by anodic bonding and the microchannels subsequently filled with the ion-selective (IS) membrane by capillarity. The internal metallic electrode is patterned on the silicon sub-unit and is in direct contact with the IS-membrane. A schematic cross-section of the platform is shown in figure 2.1.

Three different platform designs have been realized. The first two, called IKP and MGH, comprise an array of 30 $\mu$m to 50 $\mu$m long, 1.5 $\mu$m to 5 $\mu$m diameter micropipettes, with 5 $\mu$m of the micropipette tip protruding from the platform surface. The electrodes are situated in a 360 $\mu$m deep recess. The only difference between the IKP and MGH designs is

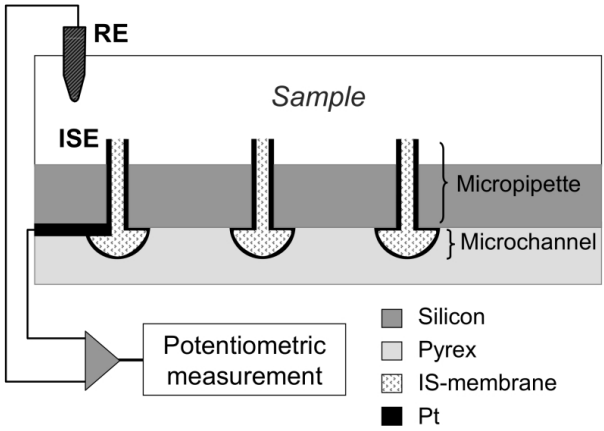


Figure 2.1: Schematic cross sections of the ion-selective platform.

the geometry of the recess. In the IKP platform, it is a square cavity of 2x2 $mm^2$ etched by anisotropic KOH wet etch, in the MGH platform, the cavity comprises two 1 mm diameter circular reservoirs, connected by a central channel of 1.2 mm length and 200 $\mu$m width. The IKP and MGH designs, as well as the micropipette layout, are illustrated in figure 2.2.

The IKP platform was originally designed to study ionic signalling in sections of hepatic tissues. This design was conceived for a study in collaboration with the research group of Prof. Jean-François Dufour of the "Institut für Klinische Pharmakologie" (IKP), of the University of Bern, Switzerland. Prof. Dufour's group research is focussed on the physiology of liver and liver diseases. One of the main research topics is the study of inositol 1,4,5-triphosphate receptor function, which is related to calcium signalling. To better understand the calcium signalling mechanism and its relations with diseases, a platform for the monitoring of calcium in hepatic cell cultures and in biliary ducts has been designed. The two rows comprising 8 electrodes each, in the central part of the array (see figure 2.2) having an inter-electrode gap of 150 $\mu$m were conceived to monitor the ionic activity over all the length of a biliary duct. The 8

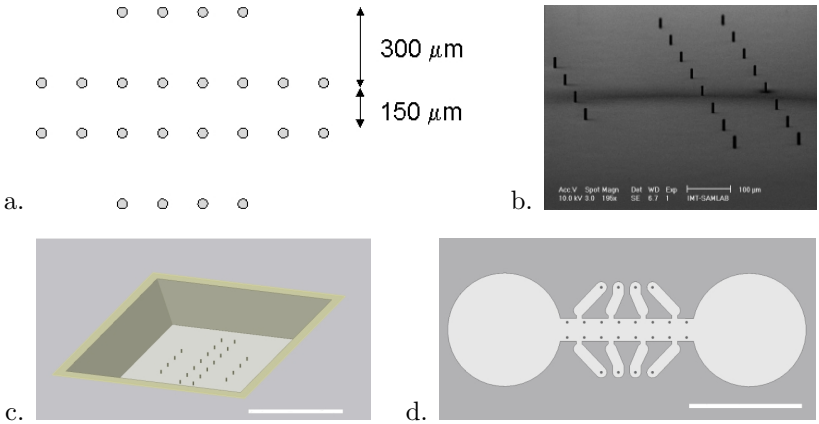


Figure 2.2: a. The design of the micropipette array. b. A SEM image of the array. c. Electrodes layout in the IKP platform. d. Electrodes layout in the MGH platform. Scale bars in c. and d. are 1 mm.

micropipettes placed at the sides were aimed either at drug delivery or at monitoring of the extracellular medium.

A second design, comprising two 1 mm diameter reservoirs connected by a 200 $\mu$m wide channel where the micropipettes are situated, was designed for a project that took place in the group of Prof. Martin Yarmush in the Massachusetts General Hospital (MGH), at Harvard Medical School, Boston, USA. The project was aimed at the development of a tool to monitor the differentiation of stem cells into hepatocytes [2, 3], in view of establishing a solid protocol for the differentiation of large quantities of cells. Embryonic stem cells, deposited in one of the reservoirs at the extremities of the microchannel (see figure 2.2.d), will grow in the central channel. Growth factors and hormones will be delivered via the 8 lateral channels. One of the characteristics of the hepatocytes is their ability to eliminate excess of ammonia, which is toxic for the organism, by converting it to urea. A lower ammonia concentration can be thus expected in differentiated cell cultures than in non

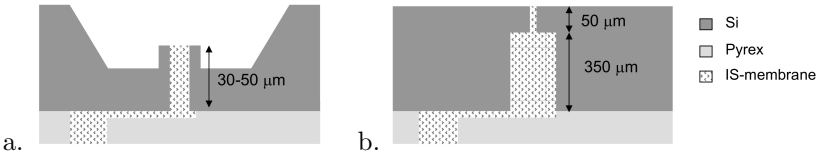


Figure 2.3: Schematic cross-section of the platforms. a. IKP/MGH platforms, comprising an array of 30 $\mu$m to 50 $\mu$ long protruding micropipettes. b. SQUARE platform, comprising an array of 400 $\mu$m overall length non protruding micropipettes.

differentiated stem cell cultures. $NH_3$ being in equilibrium with $NH_4^+$, the detoxification capacity of the cell culture can be followed by monitoring the decrease of ammonium ion concentration in the extracellular space in the vicinity of the cells, using the $NH_4^+$-selective microelectrode array situated at the bottom of the microchannel.

The main drawback of the two described platforms is the presence of the recess that renders further implementation of functionalities on-chip difficult. For this reason, a third design has been implemented. To avoid the recess, the micropipettes have been etched through the whole thickness of the silicon substrate, and are formed by a first section of 50 $\mu$m length and 1.5 $\mu$m to 5 $\mu$m diameter, connected to a second segment of 350 $\mu$m length, and 45 $\mu$m diameter, as shown in figure 2.3. This third design, called SQUARE (from the square geometry of the platform mounted on the printed circuit board, shown in figure 2.13), comprises then micropipettes of an overall height of 400 $\mu$m, without a protruding tip. With the present design, the flat chip surface obtained allowed the implementation of a metallic microelectrode array aimed at local cell electroporation.

Each platform has been employed in a different phase of the project. The IKP platform was used for the characterization of the electrodes in standard electrolyte solutions (chapter 3). The MGH platform was used for electrodes characterization and cellular assays, where an induced cellular $K^+$ efflux was recorded in real time (chapter 4). Due to their

smaller cavity volume, avoiding the excessive dilution of the ionic signal, the MGH platforms were more adapted than the IKP chips for this task. The third SQUARE design has been used to verify the possibility to perform local electroporation in the immediate vicinity of the ion-selective microelectrodes without affecting their functionality (chapter 5).

The fabrication process is partially based on the technologies presented in [4, 5]. Part of this chapter, concerning the IKP and MGH platforms, has been presented in [6]. In the following sections, the micromachining processes, followed by some highlights on the microfabrication technology, is described. The detailed fabrication processes can be found in appendix B.

## 2.2 The silicon sub-unit

### 2.2.1 The protruding micropipettes: IKP and MGH platforms

A double side polished, 390 $\mu$m thick, $\langle 1\ 0\ 0 \rangle$ silicon wafer is coated on the back side with AZ1518 positive photoresist and photostructured with arrays of 24 circular patterns of 1.5 $\mu$m to 5 $\mu$m in diameter. The center-to-center spacing of these micropatterns is 150 $\mu$m or 300 $\mu$m, as shown in figure 2.2. The patterned wafer is then etched by deep reactive ion etching (DRIE) forming cylindrical cavities with depths between 30 $\mu$m and 50 $\mu$m. After DRIE etching, a thermal wet silicon dioxide layer is grown at 1100°C to reduce the diameter of the cavities to the desired size. Thicknesses of the dioxide layer have been modulated from 0.2 $\mu$m to 3.5 $\mu$m, in order to vary the final diameter of the micropipettes. A layer of 300 nm low stress $Si_xN_y$ layer is then deposited by low pressure chemical vapour deposition (LPCVD) to form the walls of the micropipettes. Low stress silicon nitride is preferred to standard LPCVD silicon nitride, since this non-stochiometric film that contains more silicon is nearly stress free [7], which is an important feature for the mechanical stability of the micropipettes. The deposition of the low stress $Si_xN_y$ is performed in three steps: first, a 15 nm thin stochiometric

$Si_3N_4$ seed layer is deposited by using a gas ratio of $NH_3$ to dichlorosilane (DCS) of 3:1. Then, the ratio of ammonia to DCS is inversed to 1:5 for the deposition of the low stress silicon nitride layer. Finally, a 20 nm thin stochiometric $Si_3N_4$ layer is grown, as a protective layer preventing further oxidation. The deposition temperature is set at 800°C.
Next, the silicon dioxide and nitride layers of the wafer top side are etched simultaneously by reactive ion etching (RIE) with square (IKP) or channel (MGH) patterns facing the cavities of the micropipettes (figure 2.2). Subsequently, the silicon is etched until the micropipettes oxide tips are exposed. These 360 $\mu$m deep cavities are etched by KOH (40%, 60°C) or by DRIE, respectively (figure 2.4). The oxide part of the tips is wet etched in buffered HF, while the nitride caps of the tips are removed by RIE, using a $SF_6$ gas mixture. Finally, a 200 nm thin thermal oxide layer is grown onto the top side silicon surface as an electrical insulation. The platinum thin film internal electrodes of the ion-selective sensors are then patterned at the wafer backside by a lift off process.

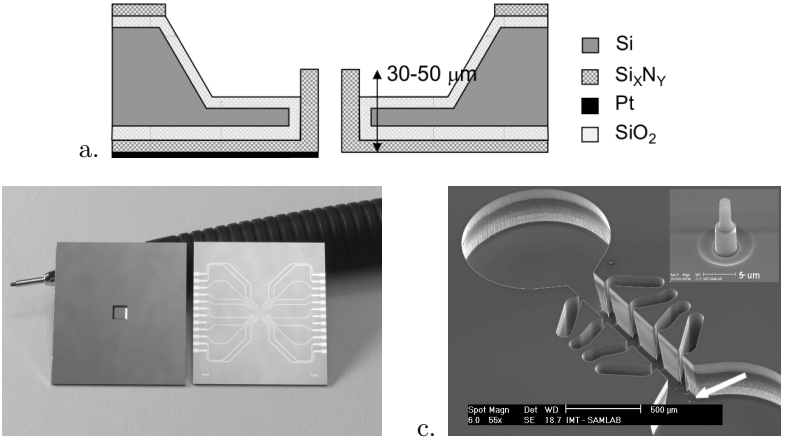


Figure 2.4: a. Schematic cross-section of the IKP and MGH silicon sub-units. b. Topside and backside of the silicon sub-unit of the IKP design. The platforms have an overall dimension of 18x20 $mm^2$. c. SEM image of the MGH design recess.

Micropipettes with a diameter down to 250 nm, 120 nm internal diameter and 15 $\mu$m overall length were fabricated using the $SiO_2$-$Si_xN_y$ two layer technique [6].
The detailed fabrication processes for the design IKP and MGH can be found in the appendix, in sections B.1 and B.2, respectively.

### 2.2.2 Growth of thermal silicon oxide in deep circular holes

Oxidation in micrometer size holes leads to a lowering in the oxidation rate in respect to the oxidation rate observed on planar surfaces. As the diameters of the micropipettes fabricated in this study range from 1.5 $\mu$m to 3.5 $\mu$m, this phenomenon must be taken into account. Figure 2.5 illustrates the difference in oxidation growth in silicon cavities of different diameters. Oxidation conditions for the formation of a $SiO_2$ layer of 1.4 $\mu$m thickness on a planar surface have been applied, and $SiO_2$ grown in Si cavities of different diameters. Subsequently, the diameter of the resulting $SiO_2$ cylinders and the thickness of the $SiO_2$ walls have been measured and are reported in figure 2.5. The $SiO_2$ walls thickness reaches about 80% of the nominal thickness for cylinders larger than 4 $\mu$m, whereas it reaches about 30% of the nominal value for cylinders smaller than 2 $\mu$m [6]. As a matter of fact, the stress associated with the non-uniform deformation of the oxide [8, 9, 10] and the limited gas diffusion in extremely small apertures are responsible for the slower oxide growth.

The dependence of the oxidation rate on the crystal orientation of the silicon surface is another phenomenon that can be observed when diameters are small. The orientation of the vertical surface of a cylindrical structure on a $\langle 1\ 0\ 0 \rangle$ silicon wafer varies periodically from $\langle 1\ 0\ 0 \rangle$ to $\langle 1\ 1\ 0 \rangle$ around the periphery. The $\langle 1\ 1\ 0 \rangle$ surface tends to oxidize faster than the $\langle 1\ 0\ 0 \rangle$ surface. Figure 2.6 depicts this phenomenon for a 1 $\mu$m internal diameter cavity obtained by growth of 2 $\mu$m $SiO_2$, resulting in a square section micropipette.

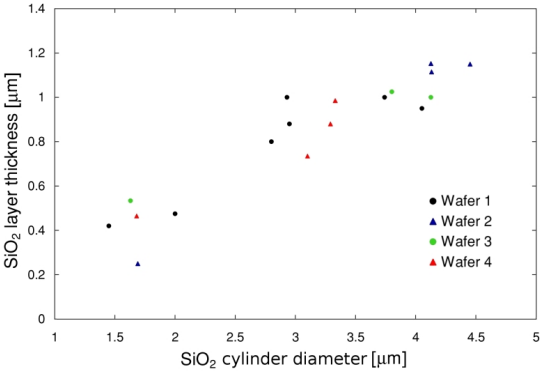


Figure 2.5: Oxidation growth in silicon cavities of different diameters, see text for details [6].

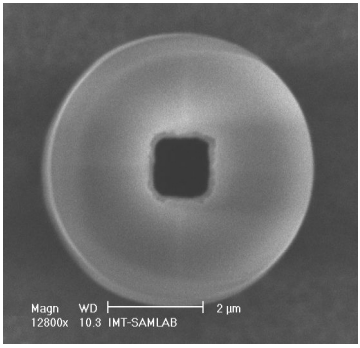


Figure 2.6: The dependence of $SiO_2$ growth rate on the silicon crystal orientation in small circular cavities leads to the formation of square section cavities.

### 2.2.3 Low stress silicon nitride for the micropipettes wall

Once the oxide layer is grown in the holes, the silicon nitride layer is subsequently deposited to form the micropipettes walls. LPCVD low stress silicon nitride was chosen since this non-stochiometric film has a number of features that are interesting for the micropipette applications. Besides its almost stress-free feature [7] and Young modulus about half of that of stochiometric silicon nitride [11], making it less vulnerable to stress [12], it can also be deposited uniformly with regards to film thickness, composition and conformal step coverage [13].
Another important aspect, general to all silicon nitride films, is the possibility of etching them selectively by reactive ion etching techniques. Unlike wet etching, reactive ion etching is inherently very directional [14, 15] and thus preserves the sidewalls of the micropipettes. In this study, we used the Alcatel plasma etching system GIR 263 equipped with a confined (RGV) and deconfined system (RIE).
For both micropipettes located at the bottom of a 2x2 $mm^2$ KOH groove at a depth of 360 $\mu$m (IKP design) and at the bottom of a 200 $\mu$m wide, and 365 $\mu$m deep microchannel (MGH design), the diameter sizes were obtained with a precision of $\pm 0.5$ $\mu$m on wafer level.

#### Geometry of the protruding micropipettes

The two-layer $SiO_2$-$Si_xN_y$ technique allows the reduction of the micropipettes diameter, while preserving the micropipette length and cylindricity obtained during the DRIE process. The tapered angle of the emerging micropipette is only $0.5^\circ$ over a length of 18 $\mu$m for a 4 $\mu$m internal diameter micropipette. It is slightly larger for a 3 $\mu$m micropipette [6].
The bottle-like shape visible in figure 2.7 is obtained by silicon oxide BHF etching followed by an additional KOH etching. The two cylindrical $SiO_2$ and $Si_xN_y$ layers are clearly visible.

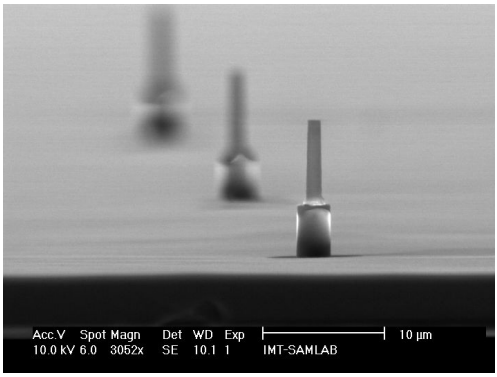


Figure 2.7: Geometry of the protruding micropipettes.

### Mechanical properties of the micropipette array

The mechanical stability of the micropipettes was qualitatively tested by pressing a 6.3 $\mu$m thin Al foil (Alcan Aluminium Valais SA, Sierre, Switzerland) on a micropipette array. This technique was already used by Griss et al. [16] to demonstrate the robustness of larger microfabricated microneedles. As an example, an array of 20 $\mu$m protruding and 4 $\mu$m diameter micropipettes was used for this test. The Al foil was pressed with a small rubber probe (10x10 $mm^2$) against the micropipette array with an estimated force of 2 N. After the mechanical stability assay, the Al foil and the micropipettes were inspected by scanning electron microscopy. Figure 2.8 illustrates a micropipette emerging without any damage from the Al foil. During the operation, a portion of the latter remained on the top part of the micropipette.

The force applied on one micropipette is in the order of 0.25 mN. For comparison, this corresponds to more than six times the force required to puncture skin (theoretical pressure to puncture skin: 3.18 MPa [17]), approximately 30 times the force needed to puncture a mouse oocyte [18] and approximatively 2000 times the force needed to puncture a human NB4 promyelocytic leukaemia cell [19]. The robustness of the

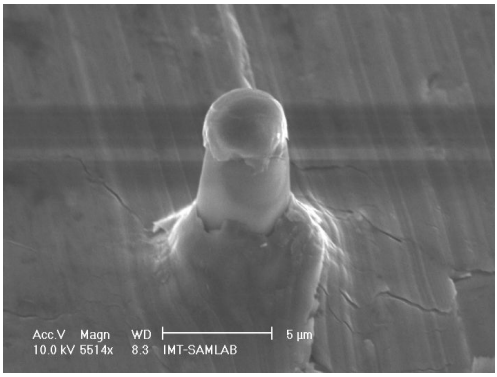


Figure 2.8: Micropipettes mechanical robustness assay. A 4 $\mu$m internal diameter micropipette emerging from the Al foil without damage.

micropipettes could be used to perform measurements in the bulk of a tissue slice, where the tissue should be less damaged than on the surface. For this purpose, platinum has been successfully electrodeposited into the micropipettes. The resulting microneedles could for example be employed in neuronal electrophysiology for recording neuronal activity of a brain slice of cells located at the core of the sample.

### 2.2.4 The non protruding micropipettes: SQUARE platform

The planar microelectrode array on the SQUARE platform is based on the same design used for the realization of the IKP and MGH platforms. It should be noted that in the present case, what is called the wafer back side during the fabrication process will become the platform top side.
The detailed fabrication process can be found in the appendix, section B.3.
For these platforms also, the fabrication is performed on a 390 $\mu$m thick double sided $\langle 1\ 0\ 0 \rangle$ silicon wafer. DRIE openings of 3 $\mu$m to 5 $\mu$m diameter and 50 $\mu$m depth are etched in the wafer back side in an analogous way to that of the IKP and MGH chips. A wet oxidation is then

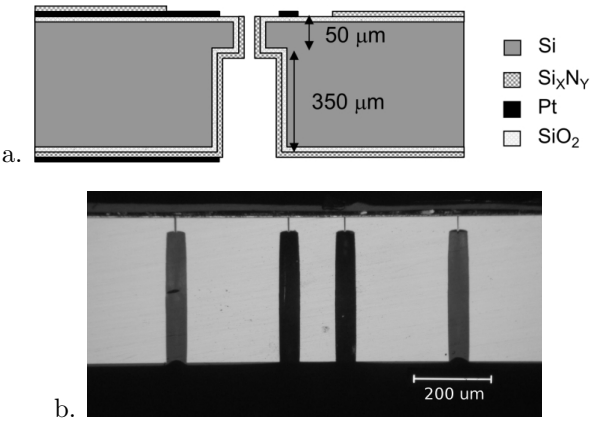


Figure 2.9: a. Schematic cross-section and b. Photograph of the SQUARE silicon sub-unit.

performed to obtain a silicon dioxide layer at least 1 $\mu$m thick. Circular patterns of 45 $\mu$m diameter, having the same layout as the first series of DRIE cavities are then obtained by photolithography at the wafer top side using a thick film of AZ4562 positive photoresist. The silicon dioxide mask is then opened to allow the DRIE etching of the silicon substrate to a depth of 350 $\mu$m. The two DRIE etched cylindrical cavities are now divided only by the silicon dioxide covering the walls of the small cavities, partially visible in figure 2.11. The silicon dioxide is completely removed by a vapour HF etch, and a new silicon dioxide layer of thickness comprised between 200 nm and 3.5 $\mu$m is grown by wet oxidation, to shrink the cavities diameter to the desired value. To allow the assembling of the silicon sub-unit and the Pyrex sub-unit by anodic bonding, the silicon dioxide at the top side of the wafer is thinned by RIE etch to obtain a 200 nm thick layer.

The platinum electrodes at the wafer back side are at this point deposited by evaporation and patterned by a lift off process. The design of this metallic electrode array aimed at electroporation is identical to the one used for the metallic internal contacts of the ion-selective microelec-

trodes, illustrated in figure 2.10. First, an adhesion layer of 20 nm tantalum is evaporated, followed by a layer of 120 nm of platinum. These electrodes are passivated by a layer of 300 nm thickness of low stress $Si_xN_y$, grown by LPCVD. The passivation layer is opened by RIE over a circular area of 45 $\mu$m diameter concentric to the DRIE cavity, as shown in figure 2.10.d, and over the electrical connections pads. The electrodes obtained have an area of 1300 $\mu m^2$.
The last step for the completion of the silicon part of the platform is the patterning of platinum thin film internal electrodes by a lift off process.

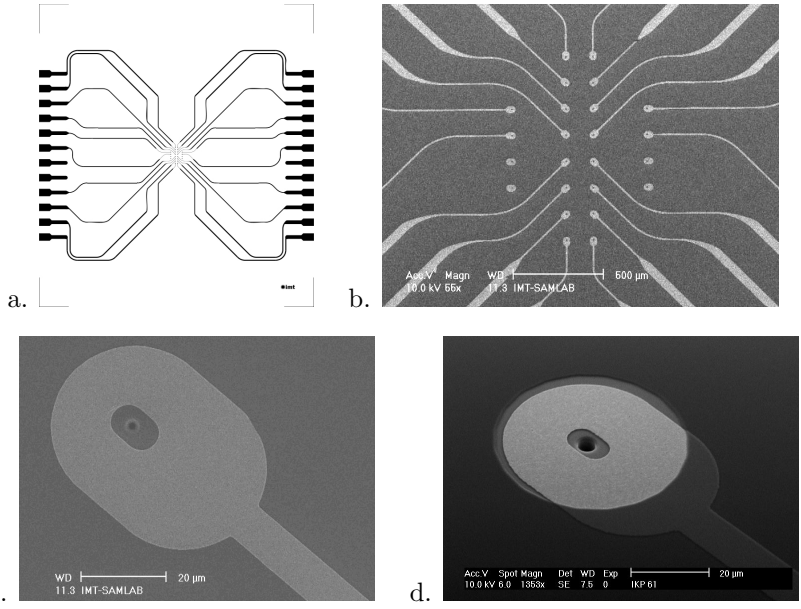


Figure 2.10: a. Schematic representation of the Pt electrodes layout. b. SEM photograph of the center of the array. c. SEM photograph of a $\mu$ISE Pt internal electrode. The hole present at the center of the structure corresponds to the basis of the micropipette. d. SEM photograph of a Pt electroporation electrode on the surface of a SQUARE platform, based on the same design as the $\mu$ISE Pt internal electrodes.

### The 400 $\mu$m long micropipettes

After the two DRIE etch steps, a residual silicon dioxide wall separates the two etched holes. To open the channel, this wall, grown at the same time as the mask for the deep 350 $\mu$m DRIE etch, has to be removed. The dry etching by RIE at the bottom of the 45 $\mu$m diameter, 350 $\mu$m deep holes has been shown to be ineffective. To completely remove silicon dioxide in geometries where the access is difficult with conventional liquid processing, vapour HF etching can be very effective. On the other hand, it is impossible to selectively etch only the residual silicon oxide wall between the DRIE channels without etching the oxide on the walls of the smaller cavity. For this reason, the silicon dioxide is completely removed before a new oxide layer is grown by wet oxidation. Figure 2.11 shows the cross-section of a SQUARE chip, where the residual $SiO_2$ wall is partially etched.

To protect the silicon during the DRIE etch of the 350 $\mu$m deep section of the micropipettes, a thick silicon oxide mask is necessary. As mentioned before, the silicon dioxide rate growth depends on the substrate geometry, thus the growth rate in the cavities and at the opening of the cavities, at the wafer surface, is different. Thus, the growing and

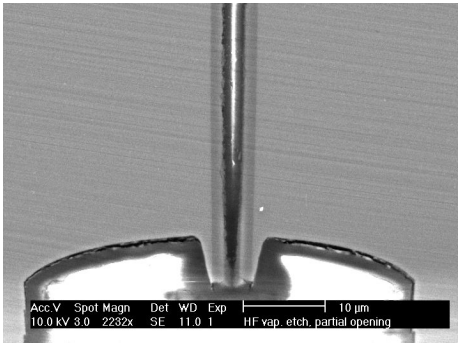


Figure 2.11: SEM photograph of a micropipette cross-section on the SQUARE platform. The residual $SiO_2$ wall between the two cavities is partially etched. The oxide wall in the small channel is clearly visible.

subsequent removal of the 3.5 $\mu$m thick silicon dioxide in the 3 $\mu$m to 5 $\mu$m diameter sections of the micropipettes leads to the formation of a conical micropipette tip instead of maintaining the cylindrical geometry, as shown on figure 2.14.d.

## 2.3 The Pyrex sub-unit and chip assembly

The 0.5 mm or 1 mm thick Pyrex substrates were purchased with micromachined 1 mm holes placed on a 4 mm x 3 mm grid, as shown in figure 2.12. The ion-selective microelectrodes are individually addressed by an array of 50 $\mu$m wide microchannels. These channels are wet etched using 20% HF, and an etch mask of 400 nm thick polysilicon mask, deposited in two steps to prevent pinholes.
To ensure an optimal contact between the $\mu$ISE Pt thin film internal electrodes and the ion-selective membrane, the Pyrex microchannels have been designed to follow the geometry of the Pt electrodes, patterned at the silicon sub-unit backside.

The silicon and the Pyrex chip sub-units are then prepared for assembly by cleaning the silicon sub-unit with a *piranha* solution (concentrated sulfuric acid + hydrogen peroxide) for 10 minutes and the Pyrex sub-unit with fuming nitric acid for 30 minutes. Immediately after the cleaning, the sub-units are assembled by anodic bonding, applying a 1200 V potential for 4 minutes (no force applied, T=500°C).

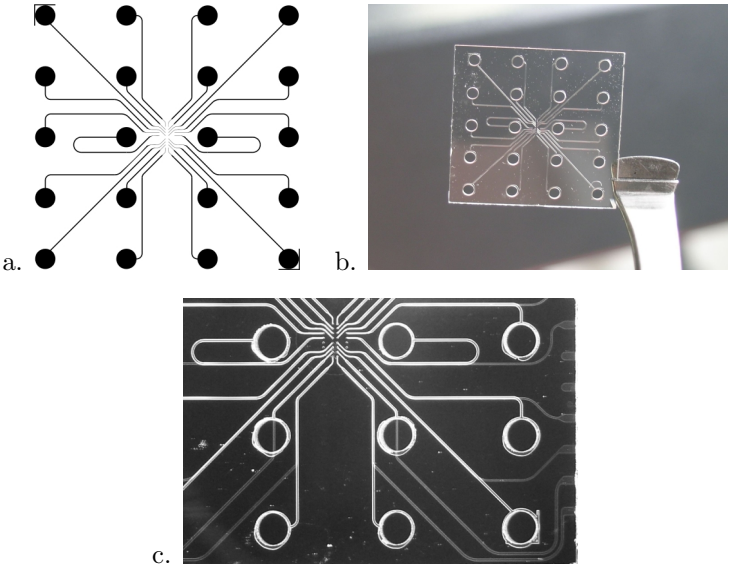


Figure 2.12: a. The Pyrex microchannels design. The black circles correspond to the 1 mm diameter holes. The microchannels connect the 1 mm holes to the micropipettes in the silicon sub-unit. b. Photograph of the Pyrex sub-unit. The sub-unit has an overall dimension of 15x15 $mm^2$. c. Close-up photograph on a section of the Pyrex substrate, assembled with the silicon chip sub-unit. The Pyrex microchannels superpose on the Pt electrodes.

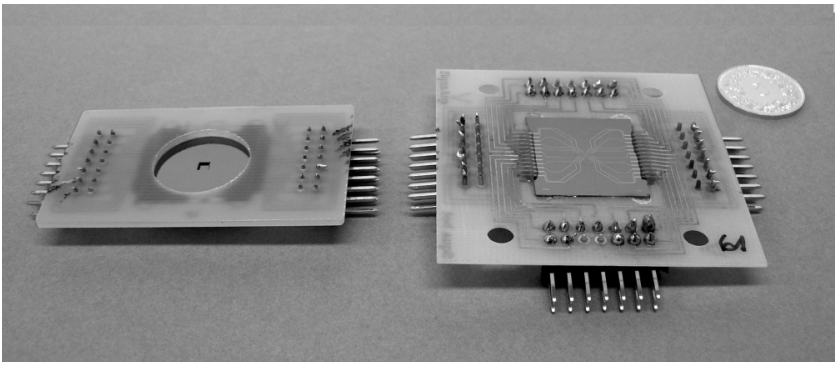

Figure 2.13: Photograph of the IKP and SQUARE platforms mounted on their printed circuit boards.

## 2.4 Micropipette-based $\mu$ISE

### 2.4.1 The Pt internal electrodes

Silver or silver/silver chloride are materials usually employed for internal metallic electrodes. However, silver is not adapted to the use on substrates undergoing anodic bonding, because of the electromigration phenomenon, which destroys the silver patterns and prevents the bonding. Preliminary tests performed in coated wire configuration using glass micropipette electrodes have shown no significant difference in signal stability when platinum, silver or silver/silver chloride were used, so platinum has been chosen as the metal for the internal electrodes.

### 2.4.2 Micropipette geometry applied to the ion-selective electrodes

The use of a micropipette geometry, comprising a capillary filled with an ion-selective membrane presents several advantages over the simpler planar electrode design. One of the main causes of the short lifetime of the microfabricated planar ISE is the loss of adhesion of the IS-membrane,

with the subsequent loss of functionality of the sensors. The anchoring of the ion-selective membrane in the microcapillary prevents the detachment of the membrane and offers a mechanical stability to the electrodes. Analogous designs were for example proposed by Uhlig et al. [20], or more recently by Sundfors et al. [21]. They proposed a microfabricated platform comprising a large reservoir, where the ion-selective membrane was dispensed, or a (non microfabricated) recessed ion-selective microelectrode, respectively. The extremely large volume to active area ratio could also have a positive influence on the lifetime of the sensors. The microchannel filled with the IS-membrane can function as a reservoir for the ion-selective membrane components susceptible to leak from the electrode, thus increasing the sensor lifetime.

### 2.4.3 Microelectrodes filling with the ion-selective cocktail

To render the microchannel walls hydrophobic, and thus allow the capillary filling of the sensors with the organic ion-selective cocktail, a treatment of the chip surface by silanization is necessary. This step is performed before mounting the chips on the printed circuit board. After at least 30 min of dehydration in an oven at 150°C, the silanizing agent N,N-dimethyltrimethylsilylamine (Fluka) is added and another 30 min at 150°C are allowed for the vapour phase reaction.
It has been observed that the surface-treated chips can be stored for years in a dry environment without losing their surface hydrophobicity. If the chips are not stored in a dry environment, it is recommended to dehydrate them under vacuum or in an oven, at 120°C, for 30 min before the filling with the IS-membrane cocktail. Both the protruding and non protruding micropipettes are sufficiently small to avoid the membrane cocktail overflow. Images of microelectrodes filled with IS-membrane are presented in figure 2.14.

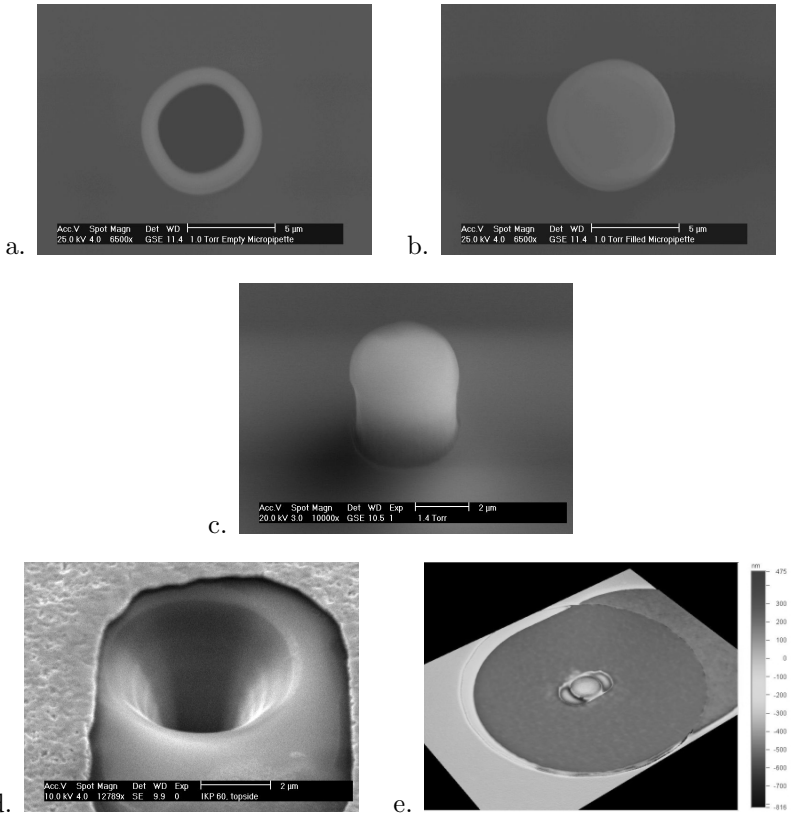


Figure 2.14: Environmental SEM photographs of protruding pipettes. a. A 5 $\mu$m diameter empty micropipette. b. The same type of micropipette as in a., now filled with a 5 wt% PVC containing ion-selective membrane. c. A micropipette filled with a 14 wt% PVC containing ion-selective membrane. d. SEM photograph of an empty 5 $\mu$m diameter planar electrode. e. Interferometry image of an electrode of the same type shown in d., now filled with a liquid (0 wt% PVC)ion-selective membrane.

## 2.5 Summary

The IKP and MGH platforms comprise 5 $\mu$m protruding micropipettes, of 30 $\mu$m to 50 $\mu$m overall length and 1.5 $\mu$ to 6 $\mu$m diameter, situated in a 360 $\mu$m deep recess. The SQUARE platform comprises non protruding micropipettes, of 400 $\mu$m overall length and 1.5 $\mu$ to 5 $\mu$m tip diameter. This platform presents a combined $\mu$ISE-Pt electrode array. The arrays comprise 24 micropipettes, with an inter-electrode gap of 150 $\mu$m or 300 $\mu$m. The micropipettes are individually addressed by an array of Pyrex microchannels and a Pt thin film electrode array. The micropipettes have been successfully filled with $K^+$- and $Ca^{2+}$-selective membranes. Figure 2.15 summarizes the main characteristics of the three realized designs.

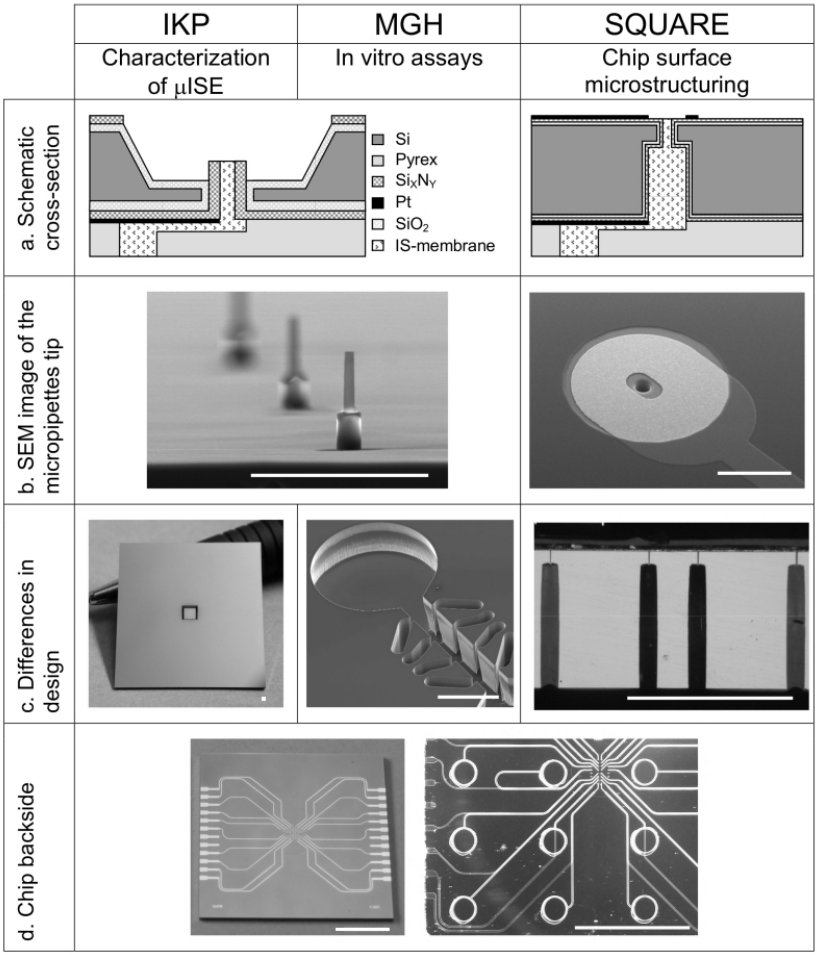


Figure 2.15: Summary of the three platform designs. Scale bars in b. are 20 $\mu$m, in c. are 500 $\mu$m, and in d. are 5 mm.

# Bibliography

[1] Ammann D. *Ion-selective microelectrodes, principles, design and application.* Springer-Verlag, 1986. ISBN 0-387-16222-4.

[2] Hamazaki T, Iboshi Y, Oka M, Papst PJ, Meacham AM, Zon LI, and Tereda N. Hepatic maturation in differentiating embryonic stem cells *in vitro*. *FEBS Lett.*, 497:15–19, 2001.

[3] Cantz T, Manns MP, and Ott M. Stem cells in liver regeneration and therapy. *Cell Tissue Res.*, 331:271–282, 2008.

[4] Luginbuhl P, Indermuhle P-F, Grétillat M-A, Willemin F, de Rooij NF, Gerber D, Gervasio G, Vuilleumier J-L, Twerenbold D, Düggelin M, Mathys D, and Guggenheim R. Femtoliter injector for DNA mass spectrometry. *Sens. Actuators B*, 63:167–177, 2000.

[5] Chun K, Hashiguchi G, Toshiyoshi H, and Fujita H. Fabrication of an array of hollow microcapillaries used for injection of genetic materials into animal/plant cells. *Jpn. J. Appl. Phys.*, 38:L729–L281, 1999.

[6] Guenat OT, Generelli S, Dadras M, Berdondini L, de Rooij NF, and Koudelka-Hep M. Generic technological platform for microfabricating silicon nitride micro- and nanopipette arrays. *J. Micromech. Microeng.*, 15:2372–2378, 2005.

[7] van Zeijl HW, Mijacovic S, and Nanver LK. Electrical detection and simulation of stress in silicon nitride spacer technology. *J. Mater. Sci., Mater. Electron.*, 12:339–341, 2001.

[8] Kao DB, McVittie JP, Nix WD, and Saraswat KC. Two dimensional thermal oxidation of silicon I. Experiments. *IEEE Trans. Electron Devices*, 34:1008–1017, 1987.

[9] Kao DB, McVittie JP, Nix WD, and Saraswat KC. Two dimensional thermal oxidation of silicon II. Modeling stress effects in wet oxides. *IEEE Trans. Electron Devices*, 35:25–37, 1988.

[10] Xu Y, Sudhama C, Hong S, Sellers JA, Ambadi S, Kamekona K, Averett G, Ruiz B, Wan I, Cai W, Wu Y, Costa JC, and Davies RB. A physically-based model for oxidation in a circular trench in silicon. *Proc. Nanotech.*, 2002.

[11] Kieswetter L, Zhang JM, Houdeau D, and Steckenborn A. Determination of Young's moduli of micromechanical thin film using resonance method. *Sens. Actuators A*, 35:153–159, 1992.

[12] Fan LS, Howe RT, and Müller RS. Fracture toughness characterization of brittle thin films. *Sens. Actuators*, A21-A23:872–874, 1990.

[13] Gardeniers JGE, Tilmans HAC, and Visser CCG. LPCVD silicon rich nitride films for applications in micromechanics studied with statistical experimental design. *J. Vac. Sci. Technol. A*, 14:2879–2892, 1996.

[14] Jansen H, Gardeniers H, de Boer M, Elwenspoek M, and Fluitman J. A survey on the reactive ion etching of silicon in microtechnology. *J. Micromech. Microeng.*, 6:14–28, 1996.

[15] Oehrlein G, Doemling M, Kastenmeier B, Matsuo P, Rueger N, Schaepkens M, and Standaert T. Surface science issues in plasma etching. *IBM J. Res. Dev.*, 43:181–197, 1999.

[16] Griss P and Stemme G. Novel, side opened out-of-plane microneedle for microfluidic transdermal interfacing. *Proc. MEMS*, pages 467–470, 2002.

[17] Aggarwal P and Johnson CR. Geometric effects in mechanical characterizing of microneedles for biomedical applications. *Sens. Actuators B*, 102:226–234, 2004.

[18] Sun Y, Wan K-T, Roberts KP, Bischof JC, and Nelson BJ. Mechanical property characterization of mouse zona pellucida. *IEEE Trans. Nanobiosci.*, 2:279–286, 2003.

[19] Boukallel M. personal communication.

[20] Uhlig A, Lindner E, Teutloff C, Schnakenberg U, and Hintsche R. Miniaturized ion-selective chip electrode for sensor application. *Anal. Chem.*, 69:4032–4038, 1997.

[21] Sundfors F, Bereczki R, Bobacka J, Tóth K, Ivaska A, and Gyurcsanyi RE. Microcavity based solid-contact ion-selective microelectrodes. *Electroanalysis*, 18:1372–1378, 2006.

# Chapter 3

# Ion-selective microelectrodes

## 3.1 Introduction

### 3.1.1 Glass capillary ion-selective microelectrodes

Ion-selective electrodes are unique devices, allowing the direct measurement of free ionic activities, not possible with other techniques [1], they do not need the addition of chemicals in the sample solution, it is thus expected that their use will interfere in a minimal extent with the physiology of the cell. Microelectrodes offer the possibility of a very local measurement, that has permitted in the past to perform measurements in cell organelles [1, 2], with a relatively simple apparatus.

From the mid 1970s to the mid 1980s, the research on glass capillary ion-selective microelectrodes was at its highest point. Hundreds of studies were reported for both *in vitro* and *in vivo* recording of cellular $H^+$, $Na^+$, $K^+$, $Ca^{2+}$, $Mg^{2+}$ [1]. These studies were performed using capillary glass microelectrodes similar to the one illustrated in figure 3.1. In the case

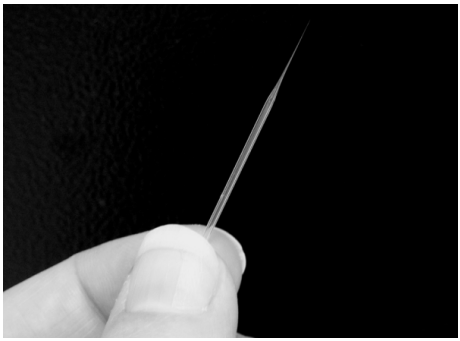

Figure 3.1: Photograph of a glass capillary $\mu$ISE.

of intracellular measurements, the cells were punctured manually (figure 3.2.a-c). The present technique is still used in physiological research, but in a less widespread way.

To follow intracellular ion concentrations, the changes in cell membrane potential should be followed in parallel [3, 4]. Monitoring of the membrane potential in a large cell is performed by insertion of a second reference electrode (RE) in the cell (figure 3.2.a) and its signal is recorded in respect to an external RE. For small cells, where impalement of two electrodes is not possible, "double barreled" electrodes have been implemented. They comprise an ISE and a RE on the same electrode body, as shown in figure 3.2.b. If it can be assumed that in a cell culture, all the cells have the same membrane potential, two different cells can be impaled, one with the ISE, and the other with the RE [3], as shown in figure 3.2.c. The difference in ISE and RE signals is used to verify the quality of the sealing of the cell membrane around the $\mu$ISE tip, to insure that the ISE signal corresponds to a real intracellular change and is not generated by cell leakage [5].
Double-barreled glass capillary microelectrodes have also been used to perform intracellular measurement of $H^+$ using a technique combining patch clamp and potentiometry. The microelectrodes accessed to the intracellular space not by mechanical impalement, but by sealing of the electrode tip to the cell membrane, and subsequent cell membrane rup-

ture, as in patch clamp [6] (figure 3.2.d). Self-referencing glass capillary $\mu$ISE are vibrating electrodes (figure 3.2.e). The difference in signal between the extreme positions of the electrode gives a measurement of the ion concentration (knowing the concentration of the analyte ion in the background solution) or the ion flux [7]. Vibrating glass capillary ion-selective electrodes have been used in parallel with patch clamp to monitor ionic fluxes through ion channels [8].

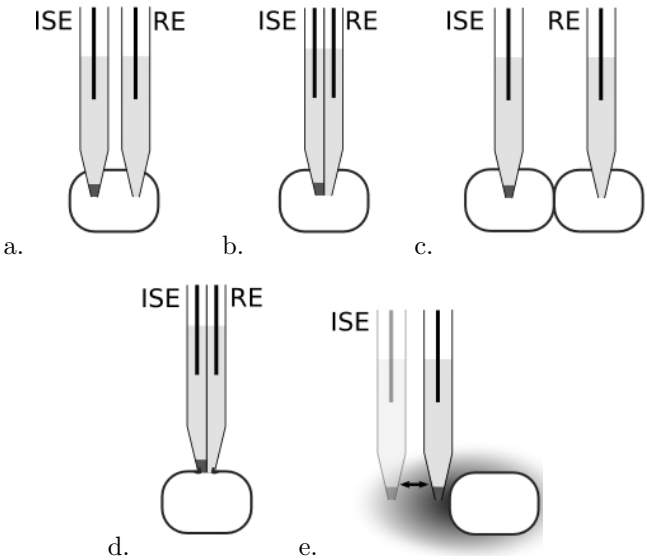


Figure 3.2: Different configurations for the use of glass capillary $\mu$ISE in cell cultures. a. ISE and RE impale the same cell. b. Double barreled microelectrode combining ISE and RE. c. ISE and RE impale two different cells presenting the same transmembrane potential. d. Double barreled glass capillary microelectrode used in patch clamp configuration. e. Vibrating, self-referencing ISE.

### 3.1.2 Microfabricated ion-selective microelectrodes

The major biological application of the ISE in present days is clinical analysis. Several microfabricated potentiometric ion-selective platforms for the measurements in biological fluids have been micromachined in silicon [9, 10, 11, 12, 13, 14] and glass or glass/PDMS [15, 16]. Although screen-printing is used for the fabrication of biochemical sensors since the 1980s, namely for disposable glucose sensors, its use for fabrication of ISE is not widespread. Screen-printed electrodes micromachined on plastic substrates are promising devices for single-use measurements [17, 18, 19], but before ISE can be microfabricated on a large scale using planar thin or thick film technology, a solid microfabrication technology should be established. This microfabrication technology should avoid the main causes of failure of these sensors, namely the loss of adhesion between the different solid layers and the lack of a stable response, due to an unadapted internal electrolyte. More information on the subject can be found in section 3.2.8.

Extremely few papers report the use of microfabricated ion-selective electrodes for *in vivo* or *in vitro* monitoring. Cosofret et al. [20] reported in 1995 the microfabrication of a polyimide-based $H^+$- and $K^+$-selective electrode array for *in vivo* monitoring of ionic variations in muscle tissues during ischemia. The replacement of the polyimide with a substrate rigid at room temperature but soft after implantation, permitted the minimization of tissue damage [21]. This second array, comprising 9 electrodes of a diameter of several hundreds of microns, for measurements of $H^+$, $K^+$, $Na^+$ and $Ca^{2+}$, has been successfully tested *in vivo* [21].
A second microelectrode array, aimed at extracellular monitoring of $Ca^{2+}$, has been recently reported [22]. This silicon-based platform comprises an array of 16 square cavities of 150 $\mu$m side length, filled with IS-membrane. The IS-membrane in each cavity is contacted by the mean of 4 Ag/AgCl internal electrodes. The platform has been used for the monitoring of extracellular calcium fluctuations of fern spores in microgravity.

## 3.2 Principles of ion-selective electrodes

### 3.2.1 Ion-selective membrane components

Liquid polymeric IS-membranes based on neutral carriers are lipophilic organic solutions into which, ideally, only the primary ion can be extracted. The components of such a membrane are the following:

**Plasticizer or membrane solvent.** It is the solvent for the membrane components. It is a lipophilic liquid with low vapour pressure. The selectivity of the IS-membrane can be influenced by the polarity of the plasticizer: more polar solvent will increase the selectivity of divalent over monovalent ions [1]. The most commonly used plasticizers are bis(2-ethylhexyl)sebacate (DOS, dielectric constant 4) and 2-nitrophenyl octyl ether (o-NPOE, dielectric constant 24).

**Ionophore or ion carrier.** The term ionophore ("which carries ions") indicates a compound that facilitates the transmission of an ion across a lipid barrier by combining with the ion or by increasing the permeability of the barrier to it. In ion-selective electrodes, the properties of an ionophore to form a hydrophobic complex with a specific ion are exploited to allow the solubilization of the ion in the ion-selective membrane phase. In the ideal case, it forms a strong but reversible complex exclusively with the primary ion. Typical concentrations of ionophore in the membrane are $10^{-2}$ mol kg$^{-1}$ to $10^{-1}$ mol kg$^{-1}$, but can go down to about $10^{-4}$ mol kg$^{-1}$ [1].

**Lipophilic ion exchangers or ionic sites.** To achieve an ideal response, the permselectivity of the IS-membrane should be ensured. This phenomenon, also called Donnan exclusion, means that no significant amount of ions of opposite charge to the primary ion may enter the membrane [23]. In neutral carrier-based membranes, permselectivity is given by counterions confined to the membrane phase. Early liquid membrane ISE were realized without the addition of lipophilic ionic sites [24], but a response improvement was observed when these components were present. Usually a tetraphenylborate salt is added to cation-selective electrodes, a tetraalkylammonium salt to anion-selective electrodes [23].

An excess of ionic sites with respect to the complexing capacity of the ionophore should be avoided [25]. As the lipophilic ionic sites have also ion-exchanger properties (see for example [26, 27]), an excess of ionic sites will enter in competition with the ionophore and extract cations into the membrane phase. As the selectivities of the lipophilic sites are different (and obviously less favourable) than those of the ionophore, the selectivity will in this case be dictated by the ion exchanger properties.
The addition of the ionic sites is also profitable to decrease the electric resistance of the membrane.

**Matrix.** Provides mechanical stability to the membrane. In small microelectrodes, surface tension phenomena avoid the organic IS-membrane overflowing from the electrode tip, so the addition of a polymeric matrix could be avoided. Even though the term liquid membrane is often encountered in the literature to indicate the whole family of IS-membranes, in the present work, this term will indicate the membranes that do not comprise a polymeric matrix.
The most commonly used matrix is PVC. Other polymers have been explored, such as polyurethanes and silicone rubber, used in biomedical devices because of their enhanced biocompatibility [28, 29, 30, 31]. Because they do not need the addition of a plasticizer, and thus present a diffusion coefficient of several orders of magnitude lower than classical PVC-based ISE, self-plasticizing membranes based on polyacrylates [32], ethylene-vinyl-acetates [33], acrylonitrile [34], isodecylacrylate [34], polysiloxanes [35] have recently attracted the interest of researchers, and might be useful for future use in miniaturized ISE [36] and for minimization of ion fluxes through the membrane [37] (see section 3.2.7 for further information). Porous materials, like porous glassy carbon [38] or porous silicon [39] have been used recently as solid supports for IS-membranes. The polymer matrix being one of the main components of the IS-membrane, it has an influence on the membrane polarity.

**Additives.** Other membrane components that can be used to improve the electrode performance are mixtures of lipophilic cations and anions [40], which lower the membrane electrical resistance and rises the upper detection limit by reducing the anionic interfer-

ence. An example of a widely used lipophilic salt of this type is ETH 500, tetradodecylammonium tetrakis(4-chlorophenyl)borate. Lipophilic inert nanoparticles have also been added to lower the ionic fluxes into the membrane phase [41].

### 3.2.2 Potentiometric response mechanism

In figure 3.3, a schematic view of an electrochemical cell, comprising a reference electrode and an ion-selective electrode is presented.

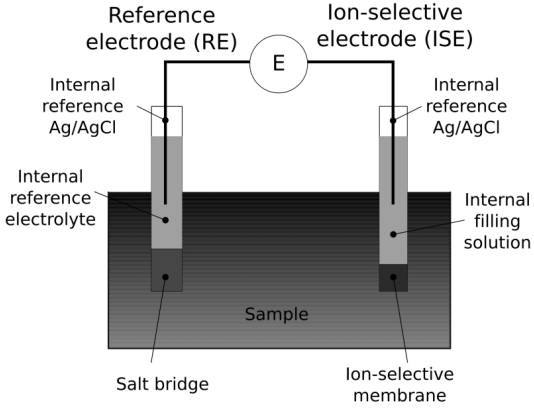


Figure 3.3: Schematic view of a generic ion-selective potentiometric cell.

The cell can also be presented as follows:

$$\underset{E_1}{\text{Ag}} \mid \underset{E_2}{\text{AgCl}} \mid \underset{E_3}{\text{KCl}} \mid \underset{E_J}{\text{salt bridge}} \mid \underbrace{\text{sample} \mid \text{IS-membrane} \mid}_{E_M} \underset{E_4}{\text{internal solution}} \mid \underset{E_5}{\text{AgCl}} \mid \text{Ag}$$

The potential response of the electrochemical cell is the sum of all interfacial local potentials:

$$E = (E_1 + E_2 + E_3 + E_4 + E_5) + E_J + E_M \tag{3.1}$$

For a given temperature, $E_1 - E_5$ are constant, moreover, the electrolyte combinations are usually chosen to have the liquid junction potential $E_J \approx 0$.
The membrane potential $E_M$ can be subdivided in two parts, the first comprises the interfacial potential at the sample ($E_{M,\text{sample}}$) and internal electrolyte ($E_{M,\text{intl sol}}$) boundaries, and the second is a membrane-internal contribution ($E_D$), called diffusion potential:

$$E_M = E_{M,\text{sample}} + E_{M,\text{intl sol}} + E_D \tag{3.2}$$

If we assume that a zero current steady state is maintained, $E_D$ will be zero [42]. The membrane potential $E_M$ for an ideally selective membrane will thus depend only on the activities of the primary ion I in the contacting solution at either side of the membrane.

$$E_M = \frac{RT}{z_I F} \, ln \, \frac{a_I^{\text{sample}}}{a_I^{\text{intl sol}}} \tag{3.3}$$

where $z_I$ is the charge of the ion I, R the gas constant, T the temperature, in kelvin, F the Faraday constant and $a_I^{\text{sample}}$ and $a_I^{\text{intl sol}}$, the activity of the ion I in the sample and internal solution, respectively. This equation is called the Nernst equation. As the internal solution composition is kept constant, the following theoretical response is expected:

$$E = E_I^0 + \frac{RT}{z_I F} \, ln \, a_I^{\text{sample}} = E_I^0 + \frac{S}{z_I} \, log \, a_I^{\text{sample}} \tag{3.4}$$

For T = 25°C, S = 59.16 mV.
According to this equation, for a constant temperature, 1 mV is equivalent to $z_I \cdot 4\%$ change in $a_I^{\text{sample}}$.

### 3.2.3 Activity calculations

For well defined, simple electrolyte solutions, the ion activities can be calculated from the ion concentrations by the Debye-Hückel method,

corrected for the high concentrations [43, 44]. This correction makes the model applicable to ionic strength up to ca. 1 M (see eq. (3.7)). Parameters for more complex ionic species, as for example proteins, have not been specified. The ionic activities $a_X$ are related to the ionic concentrations $c_X$ by the mean of the activity coefficients $\gamma_X$:

$$a_X = \gamma_X \, c_X \tag{3.5}$$

The mean activity coefficient can be calculated by the Debye-Hückel theory:

$$log\,\gamma_{\pm} = \frac{-A \mid z_- z_+ \mid \sqrt{I}}{1 + B'\sqrt{I}} + C'I \tag{3.6}$$

Where:
A: is a temperature-dependent coefficient.
At 25°C, in water, A = 0.5108 $M^{-1/2}$
$z_+, z_-$ : are cation, anion charge numbers
B', C': are specific coefficients for different electrolytes [45]. In table 3.1, several values of interest for the present work are summarized.

Table 3.1: Modified Debye-Hückel parameters for some selected salts in aqueous solutions, at 25°C [45].

| Electrolyte | B' [$M^{-1/2}$] | C' [$M^{-1}$] |
|---|---|---|
| NaCl | 1.4225 | 0.02626 |
| KCl | 1.2796 | 0.00393 |
| $MgCl_2$ | 1.7309 | 0.05195 |
| $CaCl_2$ | 1.5800 | 0.04570 |

The ionic strength is defined as:

$$I = \frac{1}{2} \sum_X c_X z_X^2 \tag{3.7}$$

From the mean activity coefficients, the activity coefficients for the cation or anion can be calculated:

$$log\gamma_+ = \frac{\mid z_+ \mid}{\mid z_- \mid} log\gamma_\pm \tag{3.8}$$

$$log\gamma_- = \frac{\mid z_- \mid}{\mid z_+ \mid} log\gamma_\pm \tag{3.9}$$

### 3.2.4 Detection limits and sensitivity

At high and low ionic activities, the ISE response does not follow the ideal Nernstian behaviour. Usually, the response is of the type presented in figure 3.4. The lower detection limit recommended by IUPAC is the activity of the primary ion I corresponding to the point of intersection of the two linear extrapolations of the response curve. For the upper detection limit, the point of intersection of the linear range of the response with the limiting high activity response may be taken [46]. The upper detection limit is caused by the coextraction of counterions, also called Donnan exclusion failure, which causes a loss of membrane permselectivity. Addition of ionic sites in the IS-membrane insures the membrane permselectivity, and thus raises the upper detection limit. The lower detection limit can have two main causes. The first can be the interference of competing species: the electrode does not respond to the low activity of the primary ion I, but it records the activity of an interfering species J. The response in the low primary ion activity region can also be limited by the leaching of primary ions from the IS-membrane into the sample, which rises the local interfacial ionic concentration to higher levels than the true sample activity [47].

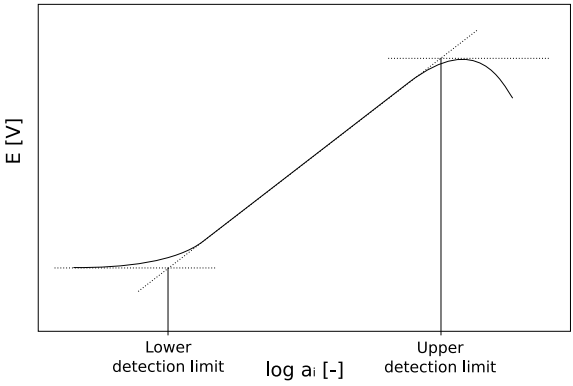


Figure 3.4: Determination of the upper and lower detection limits.

In the presence of an ionic flux across the IS-membrane causing an uptake of primary ion from the sample solution, the interfacial sample ionic activity is lowered compared to the sample bulk ionic activity and a super-Nernstian response similar to the one presented on figure 3.5 is observed [48]. In this case, the Nernstian response is observed only for higher concentrations, and intersection of the linear extrapolation of the Nernstian section of the calibration curve with the lowest measured value of $E$ will give a detection limit lower than the true detection limit. The lower detection limit is in this case defined in an analogous way as the IUPAC definition, but extrapolating the linear range of the super-Nernstan response, as illustrated in figure 3.5.

The sensitivity of the ISE is defined as the slope of the linear part of the calibration plot $E$ versus log $a_I$, and is $2.303\frac{RT}{z_I F}$ for ideal Nernstian electrodes.

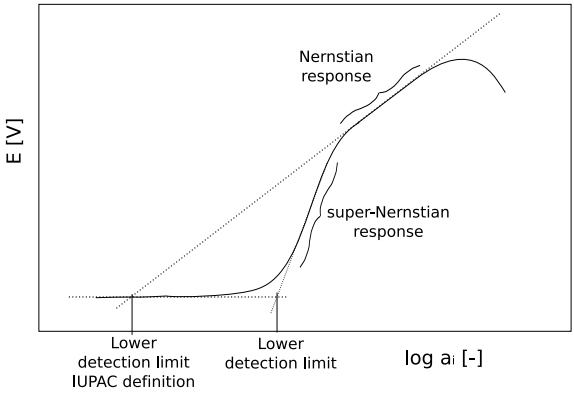


Figure 3.5: Lower detection limit in presence of a primary ion uptake from the sample.

### 3.2.5 Selectivity

The selectivity of a sensor is its preference to detect a specific ion I relative to an interfering ion (or other species) J. The potentiometric response of an ISE in presence of an interfering species J has been described in a semi-empirical form by Nikolskii and Eisenman [42, 46]:

$$E = E_I^0 + \frac{RT}{z_I F} \, ln \, a_I^{sample} + \sum_{J \neq I} K_{IJ}^{pot} \, a_J^{z_I / z_J} \tag{3.10}$$

This equation is valid only for ions of the same charge number. For other combination of ions, more general equations have been derived [49]. The factor $K_{IJ}^{pot}$, called the potentiometric selectivity coefficient, allows the quantification of the ISE selectivity. If the Nikolskii-Eisenman equation is applicable ($\mid z_i \mid = \mid z_j \mid$, Nernstian responses for both I and J), the selectivity coefficient, measured with the fixed interference method is [50, 51]:

$$K_{IJ}^{pot} = \frac{a_{I,DL}}{a_J^{z_I / z_J}} \tag{3.11}$$

where $a_{I,DL}$ is the activity of primary ion I at the detection limit. Knowing the medium where the measurements will be performed, the minimal selectivity requirements can be calculated with the following equation, giving the highest tolerable value of the selectivity coefficient [1]:

$$K_{IJ,max}^{pot} = \frac{a_{I,min}}{a_{J,max}^{z_I/z_J}} \cdot \frac{p_{IJ}}{100} \tag{3.12}$$

where $a_{I,min}$ and $a_{J,max}$ are the lowest expected activity of the primary ion and highest expected activity of the interfering ion, respectively, and $p_{IJ}$ is the highest tolerable error in the measured activity of the primary ion, in percent.

If the Nikolskii-Eisenman equation is not applicable, the selectivity coefficients calculated with equations 3.11 and 3.12 cannot be considered as physical constants [51, 52]. In this case as indication of the sensors selectivities, the detection limit, completed with the composition of the sample solution should be preferred.

### 3.2.6 Response time

The response time is defined by IUPAC as the time needed after a change in concentration of the primary ion for the slope $\Delta$E/$\Delta$t of the response curve to reach a limiting value. This definition is advantageous over the definitions $t_{95}$ (time to reach the 95% of the activity change corresponding span) and t* (time to reach E to 1 mV from the steady state value) because the equilibrium value does not need to be known. The limiting value of $\Delta$E/$\Delta$t is chosen on the basis of the experimental conditions and the accuracy needed [46].

### 3.2.7 Ion fluxes through the ion-selective membrane

Potentiometric electrodes are well-known instruments, currently used in clinical laboratories for automated screening of physiological samples. After the great advances in this field that took place in the 1970s,

the interest for ion-selective electrodes for *in vitro* and *in vivo* applications faded because of their non competitive detection limits, around $10^{-6}$ M, versus the new fluorescence techniques. Lower detection limits, in the nanomolar range, could be obtained when the sample solution was buffered for primary ions [53], but no further investigation on the mechanisms leading to such a low detection limit was performed [54]. During the 1990s, further research started with the observation of not well understood phenomena appearing with the use of a new heparin-selective electrode [55]. This has lead to an important improvement of the understanding of ionic diffusion processes in the IS-membrane. From these studies, it was demonstrated that the detection limit on the micromolar level presented by ISE was not an intrinsic property of the IS-membrane, but was either due to leaching of primary ions from the IS-membrane into the sample, thus rising the measured concentration at the IS-membrane/sample interface above the sample bulk concentration [56] or to the coextraction of primary and interfering ions from the inner solution at the inner side of the IS-membrane [57].

The choice of an appropriate inner solution allows the control of the ionic fluxes into the IS-membrane phase, resulting in an improvement of the detection limit [56, 58]. In the ideal case, to avoid any transmembrane ion flux, the inner solution should have the same composition than the sample solution. A too high primary ion concentration in the inner reference solution can lead to poor detection limits, and a too low value will induce an uptake of ions from the sample solution and a lower than expected ISE response ("super-Nernstian step") [59], as presented in figure 3.5.

A number of theoretical studies on the transmembrane ionic fluxes have been performed, [48, 59, 60, 61, 62, 63, 64] leading to the calculation and measurement of the correct thermodynamic ISE characteristics, in particular potentiometric selectivities [47, 50, 54, 65, 66]. This will permit a more rational design of future ISE [37, 67] as well as the possibility to perform preliminary virtual experiments [68]. These new approaches to potentiometry lead to the development of a number of strategies of transmembrane ion fluxes control to measure free and total (multiple) ion concentrations [69, 70, 71], realize sensors particularly sensitive in a critical concentration range [72], prevent or enhance these ionic fluxes [73, 74, 75], calibrate the ISE from the IS-membrane inner side (backside calibration) [76].

### 3.2.8 Alternatives to a liquid internal solution for $\mu$ISE

Electrodes where the IS-membrane is in direct contact with the metal, without an internal electrolyte solution or a redox layer between the metallic internal electrode and the IS-membrane are known to suffer from drift, and thus need frequent recalibration. Instabilities are related to the absence of an electrochemically well defined interface, having a common charge carrier between the IS-membrane (ion-conducting phase) and the metallic internal electrode (electron-conducting phase). These so-called blocked interfaces have initially been described as functioning on capacitive coupling between the IS-membrane surface and the metallic surface [77], and thus suffering from intrinsic instabilities. More recently, the potential instabilities have been associated to the formation of a thin water layer at the metal/IS-membrane interface, sensitive to sample changes in oxygenation [13] or ionic concentration changes [78]. Covalent bonding of the polymeric matrix to the metallic substrate [79, 80] may avoid the formation of this water layer and thus improve the ISE stability. The slow diffusion rate in non plasticized polymeric matrices [32] may also be beneficial to the signal drift, by minimizing the composition changes of the water layer.

As miniaturization renders difficult the use of a liquid internal electrolyte, the recent research in the $\mu$ISE field is focussed on strategies to overcome the problem of the lack of stability of the blocked interfaces by the use of an internal solid electrolyte layer. The internal liquid solution has been replaced by a hydrogel [13], different types of conducting polymers [81, 82], self-assembled monolayers [78, 83, 84], which provide a ion-to-electron transducer layer placed between the IS-membrane and the metallic contact, giving rise to a class of electrodes called all-solid-state ion sensors. The self-assembled monolayers have been reported not only to stabilize the potentiometric response by the adjunction of a defined redox couple, but also to inhibit the formation of the water layer at the metal electrode surface [78]. The addition of a redox couple into the IS-membrane has also been reported [81, 85]. Recently, silver and vanadium-based glasses, presenting both electronic and ionic conductivities have been proposed [86]. These latter materials are inspired by the widely used metal salts based internal contacts, e.g. Ag/AgCl [87].

# 3.3 Characterization of the ion-selective electrode array

## 3.3.1 Materials and methods

### Chemicals

The ionophores valinomycin, N-N-N'-N'-tetracyclohexyl-3-oxapentanediamide (ETH 129), the ionic additives potassium tetrakis(4-chlorophenyl)borate (KTClPB), potassium tetrakis[3,5-bis(trifluoromethyl)phenyl]-borate (KTFPB), the membrane matrix high molecular weight poly(vinyl chloride) (PVC), the plasticizers bis(2-ethylhexyl) sebacate (DOS), 2-nitrophenyl octyl ether (o-NPOE), 2,3-dimethyl nitrobenzene (DMNB), the lipophilic salt tetradodecylammonium tetrakis(4-chlorophenyl)borate (ETH 500) and the membrane solvent cyclohexanone were of Selectophore quality from Fluka, whereas all the metal chloride salts except $MgCl_2$ were of Suprapur quality from Merck. $MgCl_2$ was from Fractopur quality, from Merck. The pH and calcium buffers N-(2-hydroxyethyl)piperazine-N'-(2-ethanesulfonic acid) (HEPES), BioChemika Ultra quality, and ethylene glycol o-o'-bis(2-aminoethyl)-N,N,N'-N'-tetraacetic acid (EGTA), BioUltra, for molecular biology were also from Fluka. The silanizing agent N,N-dimethyltrimethylsilylamine (purum) was also purchased from Fluka. Aqueous solutions were prepared with cleanroom grade deionized water (>20 MΩ cm specific resistance). Dulbeccos modified Eagle medium (DMEM), foetal bovine serum (FBS), and penicillin-streptomycin (PS) were purchased from Invitrogen Corp.

### Microfabricated platforms

The results presented in the following paragraphs have been obtained using chips comprising an array of 1.5 $\mu$m diameter, 50 $\mu$m long $\mu$ISE. IKP design chips were used for all the experiments except the experiments in KCl + 150 mM NaCl solutions, where MGH chips have been employed. IKP and MGH design chips have an identical electrode design. Functionality of SQUARE design chips was tested with the potassium-selective membrane $K^+$-B (see table 3.2), and presented characteristics similar

to the IKP and MGH chips in terms of selectivity, sensitivity, drift and lifetime.

### Experimental setup

Up to 16 microelectrodes were tested simultaneously using a 16-channel homemade system realized by O. T. Guenat and G. Boulard. A 16-channel high-impedance input ($10^{14}$ Ω) amplifier, was constructed using the INA116 ultra low imput bias current amplifiers, and connected to a PC and a data acquisition card (DAQCard 6024E, National Instruments) in combination with a Labview 7.0 software. A low-pass filter stage with a cut-off frequency of 10 Hz was integrated in the amplifier. An estimation of the resistance, based on conductivity values of similar IS-membranes reported in literature [1], gave, for a 1.5 μm diameter, 50 μm long cylindrical μISE, a value around $5{\cdot}10^{12}$ Ω, indicating that the microelectrodes can be used with our amplifying system [1]. The response time of the overall electronics has been measured to be 2.5 s. As the μISE setup has an overall response time in the tenths of seconds (section 3.3.5), the long response time of the electronics will not limit the potentiometric response.

The μISE technology is very sensitive to changes in the conformation of the measuring system. For this reason, it is important to fix the places of the electrodes, ISE and RE, and to protect the system from external electrical perturbations and light interferences by a Faraday cage [88, 89]. The system should be accessible without the opening of the Faraday cage, and thus, a microfluidic chamber in PMMA has been realized, which permits to pump the sample solutions from the exterior. The chips were placed in the PMMA flow-through cell integrating a mini reference electrode (DRIREF-2, World Precision Instruments, Inc.), located downstream (figure 3.6). The volume of the measurement chamber was 15 μl. A correct shielding of the measuring chamber is of capital importance to avoid parasitic signals and current loops. The cables connecting the chip to the 16-channel acquisition card are also individually shielded. The correct grounding of the system is also important to avoid signal instabilities and earth loops [90]. Figure 3.7 gives a scheme of the earthing of the electronic setup.

a.

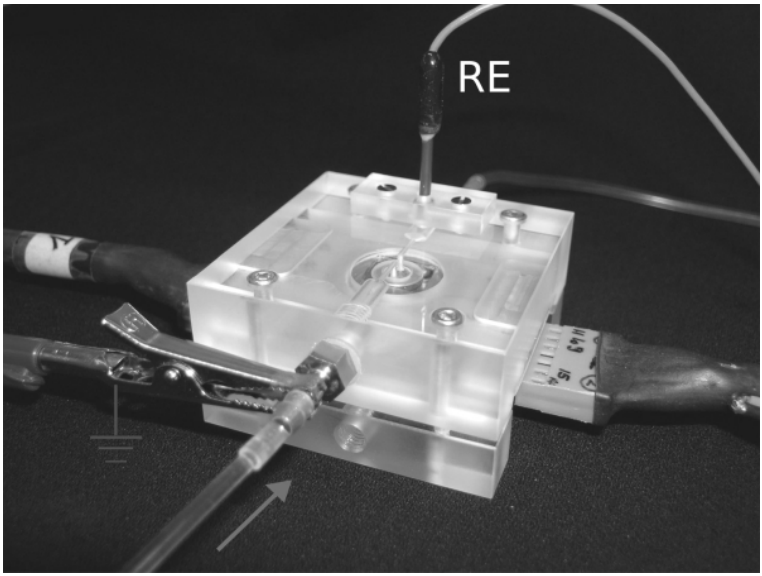


b.

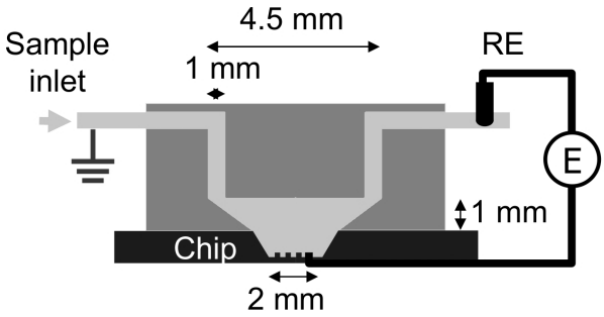


Figure 3.6: a. Photograph of the PMMA flow-through cell. b. Schematic cross-section of the flow-through cell.

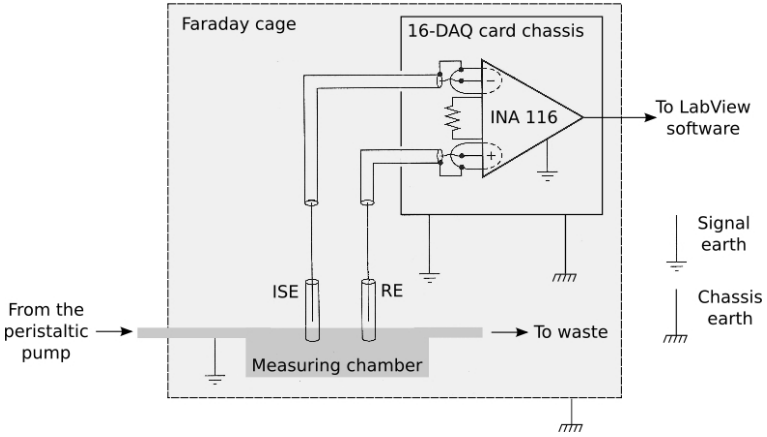


Figure 3.7: Simplified scheme of the used setup earthing. For clarity, only one $\mu$ISE channel is shown.

### Potassium calibration solutions

To eliminate all traces of residual metallic ions, the laboratory glassware was cleaned for one night with a solution of 0.01 M nitric acid.
The potassium concentration range tested was from $10^{-7}$ M to $2{\cdot}10^{-1}$ M. Interferences in both intracellular and extracellular ionic ranges have been tested. Intracellular interfering ion concentrations in calibration solutions were 15 mM for $Na^+$ and 5 mM for $Mg^{2+}$, obtained with the corresponding chloride salts. As the pH buffer HEPES is currently used for cellular assays, 5 mM HEPES buffer were added to fix the pH to 7.4. Further tests were performed with KCl solutions comprising a constant background of 150 mM NaCl, corresponding to extracellular activities of this ion. Magnesium ion concentrations are in the millimolar range in both extracellular and intracellular space. The corresponding activities are calculated using the modified Debye-Hückel model (section 3.2.3).

### Calcium calibration solutions

To eliminate all traces of residual metallic ions, the laboratory glassware was cleaned for one night with a solution of 0.01 M nitric acid.
The calibration solutions have been prepared for the testing of the ISE in intracellular space, where the lowest calcium activities are around $5{\cdot}10^{-8}$ M. The concentrations of the main interfering ions have been chosen to fit the typical intracellular values, namely 150 mM for $K^+$, 15 mM for $Na^+$ and 5 mM for $Mg^{2+}$, whereas the concentrations of calcium vary from $10^{-10}$ to $10^{-4}$ M. During all experiments, chloride salts were used. To realize very low free activity calcium solutions, two different approaches are possible: fix the pH and change the calcium buffer or keep the same calcium buffer, and adapt the pH to shift its effective buffering range. As the use of commercial calcium calibration solutions (CALBUF-1, World Precision Instruments, Inc.) based on different calcium buffers was problematic, the second alternative has been chosen: EGTA buffer was chosen, and the pH varied between 7.4 and 9. To avoid variations in the calibration solutions composition, all the calcium calibration solutions are based on 5 mM EGTA and 5 mM HEPES, even if, for low free calcium concentrations, the pH was out of the buffering range of HEPES and $Ca^{2+}$ buffering is not necessary at high calcium concentrations. To solubilize the EGTA, 50 mM KOH has been added, giving a background of 50 mM $K^+$ in all solutions. The pH was subsequently adjusted with HCl.

The calculations of the contribution of HEPES and EGTA to the ionic strength of the calibration solutions, as well as the total concentrations of $Ca^{2+}$ and $Mg^{2+}$ to be added to the solutions have been performed using the MaxChelator software, written by Chris Patton [91, 92]. This software is available at www.stanford.edu/∼cpatton/maxc.html.
All the calculations have been performed for a temperature of 25°C. With this software, the free and total ionic concentrations are calculated, to obtain activity values, the modified Debye-Hückel model, presented in the section 3.2.3 was applied. Tables of the buffer solutions compositions are reported in appendix C.

### Calibration procedure

The sensors have been designed for use in cellular media, where the ionic concentrations are within a restricted concentration range. The most appropriate calibration method in this case is the fixed interference method, where the calibration solutions present different primary ion concentrations and a fixed interfering ion background.
Calibration curves were obtained by measurements in standard solutions with incremented concentrations and plotting the measured $E$ versus $loga_i$. The slope and detection limit of the potassium calibration curves were calculated in the linear concentration range between $10^{-5}$ M and $10^{-1}$ M. The slopes and detection limits of the calcium calibration curves have been obtained from the (generally super-Nernstian) linear range comprised between $10^{-9}$ M and $10^{-5}$ M.

Calibration curves were recorded under stop-flow conditions. The complex geometrical shape of the fluidic network could strongly affect the response. In order to ensure the reproducibility of the conditions, the experimental procedure was strictly followed:
The flow rate used was 31 $\mu$l s$^{-1}$. First, the system was rinsed for 3 min with deionized water in order to clean the device of any residual ionic species. Then the lowest concentration sample solution was pumped in the flow-through cell for 1.5 min. As the electrodes are conditioned in a solution of primary ion of higher concentration than that of the first calibration solution, a resting time of 30 to 60 min was allowed to stabilize the electrodes response before the calibration. After stabilization, the following calibration sequence was repeated for increasing primary ion concentrations: pump 0.93 ml of calibration solution (flow rate 31 $\mu$l s$^{-1}$), rest period 2.5 min. The potential data values were recorded and averaged over the last 10 s of the rest period.
All measurements were carried out at room temperature at 25$\pm$2°C. This temperature variation theoretically affects the slope sensitivity by 1.4%.

### 3.3.2 Ion-selective membranes composition

Four membrane compositions, two for potassium-selective electrodes and two for calcium-selective electrodes, were used. Their compositions are given in table 3.2. The membranes $K^+$-A and $Ca^{2+}$-A are liquid membranes, not containing any PVC. Membranes $K^+$-B and $Ca^{2+}$-B contain 5 wt% and 14 wt% PVC respectively. To allow the filling of the microelectrodes, the components of the PVC containing membranes were solubilized in a solvent. Because of its lower evaporation rate, cyclohexanone was preferred to tetrahydrofuran, which is generally used as a membrane solvent. The ion-selective cocktail will thus remain liquid for a longer time, allowing an easier manipulation of the membrane cocktail and a more reproducible microchannels filling.

The classically used IS-membranes employed in glass capillary microelectrodes are liquid membranes, i.e. without a polymeric matrix, like membranes $K^+$-A and $Ca^{2+}$-A. Because of the surface tension effects, the liquid IS-membrane in the microelectrode tips will not overflow, rendering the addition of PVC not necessary. However, the addition of PVC can be beneficial because of the subsequent lowering of the diffusion coefficient in the membrane phase. The concentration of PVC has been limited to between 5 wt% and 14 wt% to minimize the risks of an excessive membrane shrinkage upon cyclohexanone evaporation, the

Table 3.2: Ion-selective membranes compositions.

| IS-membrane | $K^+$-A | $K^+$-B * | $Ca^{2+}$-A | $Ca^{2+}$-B ** |
|---|---|---|---|---|
| Ionophore | valinomycin | valinomycin | ETH 129 | ETH 129 |
| wt% | 5 | 5 | 0.5 | 0.46 |
| conc. [mmol $kg^{-1}$] | 45.0 | 45.0 | 10.9 | 10.0 |
| Ionic sites | KTClPB | KTFPB | KTClPB | KTClPB |
| wt% | 2 | 1 | 0.1 | 0.09 |
| conc. [mmol $kg^{-1}$] | 40.5 | 11.1 | 2.0 | 1.8 |
| Plasticizer | DMNB | DOS | o-NPOE | o-NPOE |
| wt% | 93 | 89 | 99.4 | 85.45 |
| Polymeric matrix | - | PVC | - | PVC |
| wt% | - | 5 | - | 14 |
| $\frac{\text{Ion exchanger}}{\text{Ionophore}}$ mol. ratio | 0.9 | 0.25 | 0.19 | 0.18 |

*: 100 mg of IS-membrane solubilized in 210 $\mu$l cyclohexanone.

**: 100 mg of IS-membrane solubilized in 105 $\mu$l cyclohexanone.

fraction of solvent needed to keep the IS-cocktail liquid becoming very high as the PVC fraction rises. The components (totalling 100 mg) of the PVC containing membranes were dissolved in cyclohexanone, 210 $\mu$l for membrane $K^+$-B [93], and in 105 $\mu$l for membrane $Ca^{2+}$-B.

The applicability of the ion-selective liquid membrane principle to the micromachined platform was verified by using the $K^+$-A membrane, a variant of a valinomycin-based membrane cocktail based on a PVC-free liquid ion-selective membrane employed in microelectrodes [94, 95]. Potassium-sensitive microelectrodes based on valinomycin are known to be very selective. Valinomycin is a cyclic, naturally occurring antibiotic produced by several Streptomyces bacterial strains, and, because of the hydrophobic surface of the valinomycin-$K^+$ complex, it allows the transport of potassium across the cellular membrane. Its well-known high selectivity of potassium over sodium has lead to its choice as ionophore in $K^+$-selective electrode membranes [24].

The absence of polymeric matrix avoids eventual drawbacks upon the shrinkage of the ion-selective cocktails occurring when cycloxexanone evaporates. The advantage of the plasticizer DMNB is its low impedance. This cocktail permitted to verify the functionality of the silicon-based micropipette electrodes. For the tests in presence of cells, presented in chapter 4, another IS-membrane has been employed. The composition chosen for the membrane comprises in this case the more apolar plasticizer DOS, and 5 wt% PVC as membrane matrix (membrane $K^+$-B, table 3.2). Having a dielectric constant of 4 vs around 24 for nitroaromatic compounds [1], DOS is more adapted than DMNB to optimize the ISE selectivity for monovalent ions over divalent ions [1, 42].

An excessively high ion exchanger to ionophore molar ratio will lead to a loss of selectivity of the IS-membrane. If an excess of lipophilic anionic sites is present, the amount of cations extracted in the IS-membrane phase will cause the total complexation of the ionophore, and the remaining uncomplexed cations will form ionic pairs with the anionic sites in excess. The selectivity of the ionophore will thus be lost and the observed sensor characteristics will depend on the lipophilic anions selec-

tivity. As the ion exchanger to ionophore ratio of 0.9 used in membrane $K^+$-A is quite high, subsequently it has been decreased to 0.25 in the membrane $K^+$-B.

The best calcium ionophores known so far are complexes synthesized at the ETH Zurich in the late 1970s [96, 97]. We chose one of them, the ETH 129, a bidentate ligand which has a calcium coordination number in PVC/o-NPOE membranes reported to be between 2 and 3 [53, 98], as ionophore for the present $\mu$ISE.The detection limit of an ISE depends on the equilibrium between the ionic species at the sample/IS-membrane interface. The presence of primary ions in the IS-membrane phase is due essentially to the presence of the ionophore. A lowering of the ionophore concentration in the IS-membrane phase will influence the concentration of primary ion in the IS-membrane. A shift of the interfacial equilibrium of primary ions to the lower concentrations is then observed, with a subsequent improvement of the detection limit.
For this reason, three concentrations of ETH 129 have been tested, 5 wt%, 0.5 wt% and 0.05 wt%. Electrodes prepared with the lowest concentration were not responsive. Electrodes having a concentration of 0.5 wt% ionophore, as expected, revealed to present a lower detection limit than the highest concentration.

For calcium sensing the membrane composition is of much higher importance than for potassium, where a non-optimized membrane composition already gives excellent results in physiological concentration ranges. For this reason, a particular effort has been made to optimize the calcium membrane composition. The plasticizer of choice has a high dielectric constant, which enhances the selectivity of multivalent ions over monovalent [42]. For this reason o-NPOE, which has a dielectric constant of about 21 and is less volatile than DMNB, is usually chosen for the use in $Ca^{2+}$-selective sensors [53, 71, 99]. It must however be kept in mind that the dielectric constant of an IS-membrane depends on all the components of the membrane, and not only on the plasticizer.
Membrane resistivity did not seem to be an issue, so further addition of highly lipophilic salts, as for example tetradodecylammonium tetrakis(4-chlorophenyl)borate (ETH 500), was not necessary. This kind of salt affects the ionic activities in the membrane phase. The effects of

the activities changes are especially noticeable in nonpolar membranes [40, 100], with an improvement of the selectivity of divalent over monovalent ions, but have a limited influence in high dielectric constant membranes, as it is the case when using o-NPOE as the plasticizer [40]. Experiments did not reveal any improvement of the membrane characteristics in ETH 500-containing electrodes.

### 3.3.3 Calibration curves: detection limit, sensitivity and selectivity

#### $K^+$-selective microelectrode arrays

The preconditioning of the electrodes before use is necessary not only for the hydration of the membrane, but also to approach a stationary state in the IS-membrane phase, and thus reach a stable $E$. For the ion-selective membranes based on neutral carriers, a stationary state is possible only if primary ions are present in the bulk of the membrane. In the present valinomycin-based IS-membranes formulations, potassium is already present in the membrane as the counter-ion of the lipophilic anionic sites necessary to insure the membrane permselectivity, in the salts KTClPB and KTFPB. The electrodes will be functional as soon as the membrane is hydrated, and thus the preconditioning does not need to be very long: good responses were observed after one hour preconditioning. The preconditioning time has however been kept longer, normally 24 hours, to allow the membrane internal ionic concentrations to stabilize.

The selectivity tests of membrane $K^+$-A have been performed with calibration solutions presenting typical intracellular levels of interfering ions, namely 15 mM $Na^+$, 5 mM $Mg^{2+}$. As often HEPES is present to buffer the solutions used in cellular tests, 5 mM of HEPES was added to our solutions, to fix the pH to 7.4. In the three cases the detection limit was pK 5.2, as reported in figure 3.8.a and table 3.3.
Sodium ions are the main interfering ionic species when working with valinomycin, and are 10 times more concentrated in the extracellular

Table 3.3: Detection limit and sensitivity of potassium-selective microelectrodes after 1 day preconditioning in KCl 1 mM.

| IS-membrane | J | n | Detection limit log $a_{K^+,DL}$ [-] | Sensitivity [mV dec$^{-1}$] |
|---|---|---|---|---|
| $K^+$-A | - * | 12 | -5.24 ± 0.08 | 60.3 ± 0.8 |
| | $Na^+$ 15 mM * | 11 | -5.18 ± 0.03 | 59.2 ± 0.9 |
| | $Mg^{2+}$ 5 mM * | 14 | -5.24 ± 0.01 | 58.8 ± 0.1 |
| $K^+$-B | $Na^+$ 150 mM | 13 | -5.83 ± 0.07 | 54.5 ± 0.5 |

*: in HEPES 5 mM background

Table 3.4: Highest tolerable and observed selectivity coefficients of potassium-selective microelectrodes after 1 day preconditioning in KCl 1 mM.

| IS-membrane | J | n | log $K^{pot}_{KJ}$ [-] | log $K^{pot}_{KJ,max}$ intracell. [-] | log $K^{pot}_{KJ,max}$ extracell. [-] |
|---|---|---|---|---|---|
| $K^+$-A | $Na^+$ 15 mM * | 14 | -3.12 ± 0.02 | -1.36 | -3.63 |
| | $Mg^{2+}$ 5 mM * | 14 | -3.96 ± 0.01 | -1.84 | -2.81 |
| $K^+$-B | $Na^+$ 150 mM | 13 | -5.00 ± 0.07 | -1.36 | -3.63 |

*: in HEPES 5 mM background

$p_{IJ}$=1%, $a_{i,min}$ and $a_{j,max}$ from table 1.1

space than in the cytosol. Microelectrodes filled with membrane $K^+$-B have been characterized in ionic background of 150 mM $Na^+$, corresponding to the more critical ion interference encountered in cell culture media. These latter conditions were also employed to perform the cellular assays presented in chapter 4. In this case, the detection limit is pK 5.8 and the response is slightly sub-Nernstian. The characteristics of the potassium-selective microelectrodes are summarized in table 3.3 and figure 3.8.

Assuming that the $K^+$-selective electrodes present also a Nernstian response towards interfering ions, the selectivity coefficients $K^{pot}_{KJ}$ can be calculated (section 3.2.5). The $K^{pot}_{IJ}$ values, in combination with the $K^{pot}_{IJ}$ required to perform measurements in cellular concentration ranges are reported in table 3.4. As $z_{K^+} \neq z_{Mg^{2+}}$, the value of $K^{pot}_{K,Mg}$ calcu-

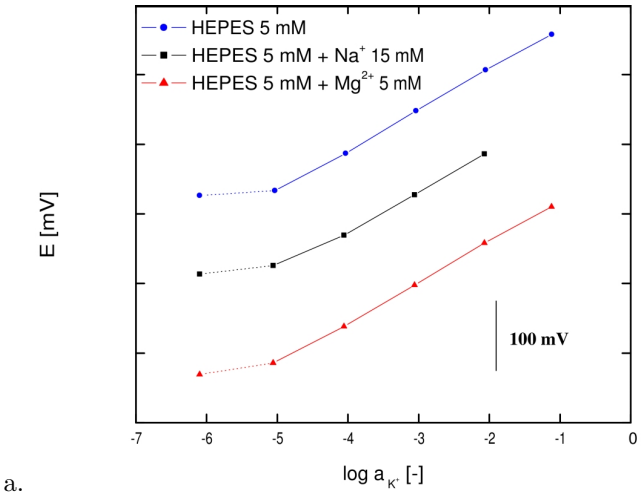


a.

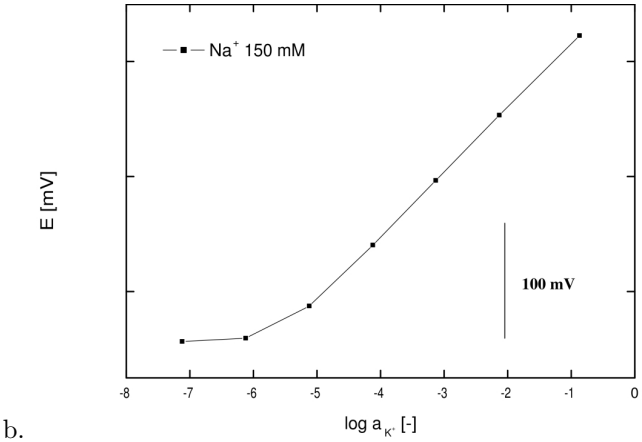


b.

Figure 3.8: Potassium calibration curves. The 1.5 $\mu$m diameter microelectrodes were preconditioned during one night in a 1 mM KCl solution. a. Membrane $K^+$-A. The potassium activity is measured in presence of intracellular levels of the main interfering ions, with a constant background of 5 mM of HEPES. b. Membrane $K^+$-B, tested in presence of extracellular concentrations of $Na^+$. The curves are offset for the sake of clarity. The electrode characteristics are summarized in table 3.3

lated with the equation 3.11 for $Mg^{2+}$ interference does not correspond to a correct theoretical constant, but it depends strongly on the experimental conditions. The values in table 3.4 give only an indication on the selectivity towards magnesium, and should be used with caution for comparison with other $K^+$-selective electrodes.
The interference of pH on $K^+$-selective electrodes is indicated to become significant only for extremely acidic conditions, near pH 2 for a concentration of potassium of 1 $\mu$M. As this value is around the detection limit of the sensors (see for example [24], one of the first valinomycin-based electrodes), the pH interference has not been tested.

### $Ca^{2+}$-selective microelectrode arrays

As it has been discussed in the previous section and in the section 3.2.4, the response of a sensor is strongly dependent on the ionic fluxes in the membrane bulk. In the calcium-selective membranes there is no calcium ion present directly after the preparation, contrary to the case of potassium ISE. The preconditioning in calcium solutions will cause an exchange of ions between the IS-membrane phase and the preconditioning solution. The cations present in the membrane, counterions of the lipophilic anionic sites are here $K^+$ coming from the salt KTClPB. During the preconditioning, $K^+$ will be exchanged for the preferred $Ca^{2+}$ ions.

The presence of the $Ca^{2+}$ flux going to the inward of the membrane is the phenomenon that allows these sensors to reach a detection limit in the nanomolar range. Usual electrodes comprising an inner filling solution can have a chelating agent for the primary ion [72] or an ion-exchange resin [58] in the inner filling solution. This will cause a continuous intake of primary ions from the sample solution, keeping the primary ion concentration at the sample/IS-membrane interface low and thus the detection limit in a low range. In all-solid-state electrodes, due to the difficulty to maintain a low and constant primary ion activity in the inner electrolyte, a super Nernstian behaviour stable over time is difficult to obtain.
We exploited the lack of primary ions in the freshly prepared $Ca^{2+}$-selective membrane, and the subsequent calcium flux taking place when binding

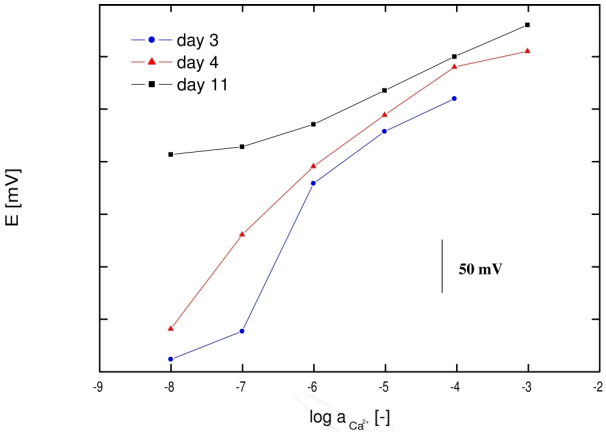


Figure 3.9: Calcium calibration curves for 1.5 $\mu$m diameter microelectrodes, membrane $Ca^{2+}$-A, conditioned in a $10^{-4}$ M $CaCl_2$ solution. The important super-Nernstian step observed in the first days lowers with time until a Nernstian response is reached. The measurements are performed in fresh unbuffered $CaCl_2$ solutions. The curves are offset for the sake of clarity.

sites for calcium in the membrane phase are not completely occupied, to induce a similar behaviour. This calcium influx permits to achieve an extremely low detection limit, however only for a limited time. The geometry of the electrode itself, comprising a large IS-membrane reservoir, makes the saturation of the entire IS-membrane with primary ions very slow compared to the usual times observed with thinner IS-membranes, thus permitting the exploitation of the electrodes in the non-stationary state. After a few days (typically 10 days for $Ca^{2+}$-A based $\mu$ISE, 3 days for $Ca^{2+}$-B based $\mu$ISE, when preconditioned in $10^{-4}$ M $Ca^{2+}$), the detection limit rises to the values encountered for electrodes having a high primary ion concentration internal solution, as shown in figure 3.9. The conditioning of these "old" calcium-selective electrodes in a solution of low primary ion and high interfering ion concentrations (in our case $10^{-7}$ M $CaCl_2$ + 150 mM KCl) allowed to restore a super-Nernstian response. Optimization of this process has however not been performed.

Table 3.5: Detection limit and sensitivity of calcium-selective microelectrodes after 3 days ($Ca^{2+}$-A) or 1 day ($Ca^{2+}$-B) preconditioning in $CaCl_2$ $10^{-4}$ M.

| IS-membrane | J | n | Detection limit log $a_{K^+,DL}$ [-] | Sensitivity [mV $dec^{-1}$] |
|---|---|---|---|---|
| $Ca^{2+}$-A | $K^+$ 150 mM | 12 | -8.00 ± 0.04 | 59 ± 2 |
| | $Na^+$ 15 mM | 12 | -8.05 ± 0.02 | 85 ± 2 |
| | $Mg^{2+}$ 5 mM | 12 | -7.83 ± 0.05 | 45 ± 1 |
| $Ca^{2+}$-B | $K^+$ 150 mM | 5 | -9.2 ± 0.4 | 35 ± 2 |
| | $Na^+$ 15 mM | 13 | -9.52 ± 0.05 | 30.8 ± 0.6 |
| | $Mg^{2+}$ 5 mM | 15 | -9.0 ± 0.1 | 40.0 ± 0.2 |

Other possibilities for regenerating the IS-membrane by reversing the primary ionic flux, for example by conditioning the platform in a solution of chelating agent [101] or by applying a current [75], have not been investigated, but would be an interesting possibility.

Interference of $H^+$ has not been tested in the present case, since it has been reported that the effect of pH in the $Ca^{2+}$ millimolar range is negligible even at pH 2. The reported selectivities indicate that for a detection limit of $a_{Ca^{2+}}$=$10^{-9}$ M, $H^+$ interference takes place when pH $\leq$5 [53]. As both in intracellular and extracellular environments the pH is around 7, the $H^+$ interference is negligible.

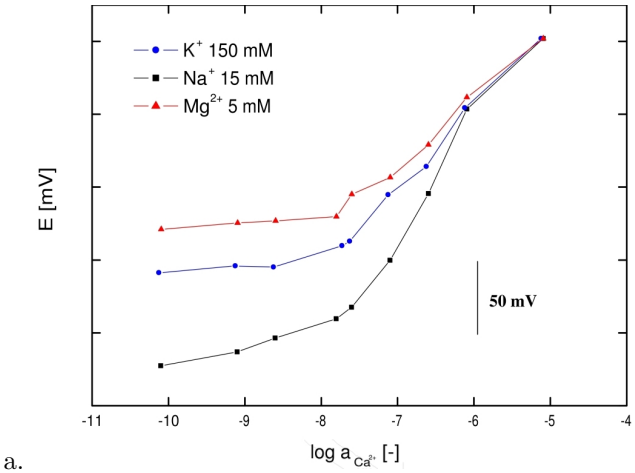


a.

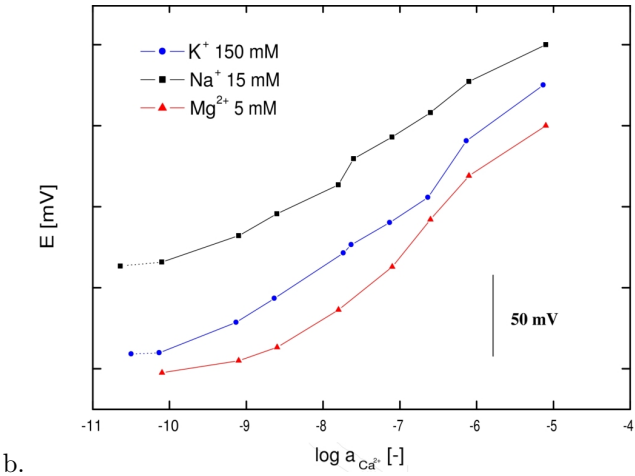


b.

Figure 3.10: Calcium calibration curves for 1.5 $\mu$m diameter microelectrodes. The calcium activity is measured in presence of intracellular levels of the main interfering ions. a. Membrane $Ca^{2+}$-A, conditioned during three days in a $10^{-4}$ M $CaCl_2$ solution. b. Membrane $Ca^{2+}$-B, conditioned during one day in a $10^{-4}$ M $CaCl_2$ solution. The curves are offset for the sake of clarity. The electrode characteristics are summarized in table 3.5

### 3.3.4 Drift

Coated wire type electrodes are known to suffer from potential instabilities due to the formation of a thin water layer at the metal/IS-membrane interface, responding to sample changes in oxygenation [13] or ionic concentration changes [78]. In our case, the bubbling of nitrogen into the sample solution in contact with a glass micropipette potassium-selective microelectrode lead to a measured potential difference of 1.2 mV. For calcium-selective electrodes, this corresponds to 0.04 units of pCa, which is an acceptable measurement error.
If the presence of a water layer between the membrane and the internal metallic electrode is assumed, it has been demonstrated that the preconditioning in a solution of primary ions alone is beneficial to lower the drift [78]. After preconditioning in a solution of primary ions, the main ionic species in this inner water layer will be primary ions. As the presence of primary ions in the IS-membrane phase is more favourable than the presence of interfering ions, when interfering species will reach the IS-membrane/inner layer interface, they will rapidly be exchanged with the primary ions. This induces a rapid drift, but the final equilibrium is approached much faster than in the case where interfering ions are present in the inner layer, and should be exchanged with primary ions to reach an equilibrium [64, 78].

Thus, in the present case, the potassium-selective electrodes were preconditioned in $10^{-3}$ M KCl solutions, and calcium-selective electrodes in $10^{-4}$ M $CaCl_2$ solutions.

To overcome the observed instabilities, the sensors were allowed to stabilize for 30 min to 60 min in the concentration range of interest before starting the measurements [102]. After the stabilization time, drifts for electrode arrays filled with the different ion-selective cocktails had similar values, typically $5\pm3$mV $h^{-1}$. It has been observed that drift in cell culture media were comparable to those observed in simple electrolyte solutions.

On the timescale of the calibration of the electrodes, the drift is limited, and thus does not influence in an important way the characterization

of the electrodes. The cell assays targeted in this work are also limited to a few hours, so the drift is not an issue. In contrast, for long-time monitoring, stabilization procedures should be implemented. In cellular assays, the signal stabilization is not only dependent from the intrinsic properties of the electrodes, but is also influenced by the biofouling of organic material on the electrodes surface.

### 3.3.5 Response time and hysteresis

The response time is defined here as the time necessary to obtain a slope of 1.2 mV $min^{-1}$ on dynamic response curves of potassium-selective electrodes, after a step from pK 3 to pK 2, and a variation of 0.6 mV $min^{-1}$ for calcium selective electrodes, for a step from pCa 6 to pCa 5. As the response time is partially dependent upon the fluidics, the reported values correspond to the overall system response time, and not to the intrinsic sensor response time. The observed response time for both potassium and calcium-selective electrodes vary between 40 s and 120 s, depending on the composition of the calibration solution, the response time being longer in solutions without background electrolyte. The use of the plasticizer DOS, having a lower polarity than DMNB, decreases the response time of $K^+$-selective membranes [42]. Theoretical models [42] also indicate that a lowering of the diffusion coefficients into the membrane phase, for example by addition of PVC, should ameliorate the response time, but in the present case, no difference was observed between liquid or PVC-based membranes. With the sensor aging, the potentiometric signal becomes more sensitive to streaming potentials and other parasitic signals, but the response time is unaffected.

Hysteresis is a critical issue in the use of the present platform, especially for calcium-selective arrays, due to the very broad ion concentration span tested and the low detection limit required. Potassium-selective electrode arrays are less affected by hysteresis effects, especially when the low dielectric constant plasticizer DOS is present. Near zero hysteresis was observed for electrodes prepared with membrane $K^+$-B, without PVC. Figures of a non optimized potassium response versus an optimized response are presented in figure 3.11. The improvement of the

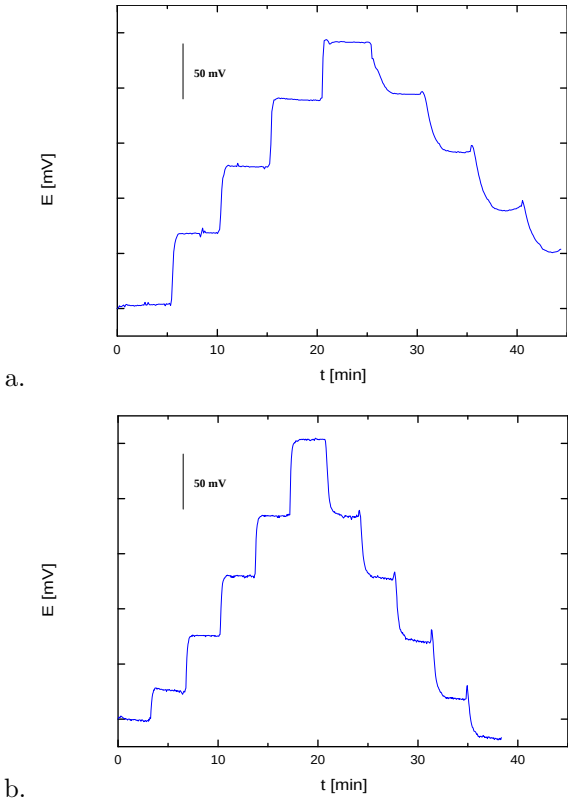


Figure 3.11: Non optimized versus optimized potassium response curves. See text for details.

response characteristics of the potassium sensitive platform in respect to both the response time and the hysteresis has been achieved by optimization of different parameters of the setup, such as: the change of the ion-selective membrane plasticizer from the polar DMNB to the apolar DOS, an appropriate design of the microwell aimed at the reduction of its dead volume, a higher calibration solution flow rate, from 15 $\mu$l s$^{-1}$ to 47 $\mu$l s$^{-1}$. The optimization has allowed to lower the hysteresis ob-

served between pK 2 and pK 1 from 6 mV (corresponding to 0.1 units of pK) to less than 1 mV (corresponding to 0.01 units of pK).
Measurement errors due to hysteresis for optimized sensors have been estimated to 0.01 units of pK, and from 0.01 units of pCa for high concentrations of calcium, 0.1 units of pCa for low concentrations.
Hysteresis effects are more enhanced in low conductivity solutions. From the obtained results it has been observed that, to minimize the hysteresis an ionic background of at least 10 mM should be present. To avoid uncertainties due to the hysteresis effect, the electrodes should be equilibrated in a solution mimicking the sample immediately before the assay, and the measurements should be effectuated in a limited concentration range.

### 3.3.6 Lifetime

In the present case two different lifetimes will be considered. The storage lifetime is defined as the time during which the sensors present a sensitivity more than 70% of the Nernstian value. The functional lifetime, has an additional criterion: the electrodes must present a detection limit of at least pK 4 and pCa 8, adapted for the use in cellular concentration ranges.
The storage lifetime of the 1.5 $\mu$m-diameter electrode arrays varies from 1 to 2.5 months, when stored in a chloride solution of the primary ion, i.e. 1 mM for $K^+$ or $10^{-4}$ M for $Ca^{2+}$. For potassium-sensitive electrodes, the detection limit generally increases gradually from pK 5 to pK 4 during the sensor lifetime and the loss of functionality is given by a loss of sensitivity. The storage lifetime and functional lifetime are in this case identical. In contrast, while the response of calcium-selective electrodes also takes 2.5 months to fall under the of 60% of the Nernstian slope, the detection limit rises above the limiting value of pCa 8 in a short time (see section 3.3.3), reducing the functional lifetime to 1 day for membrane $Ca^{2+}$-A and 3 days for membrane $Ca^{2+}$-B.

Table 3.6: Storage and functional lifetime of the $\mu$ISE.

| IS-membrane | $K^+$-A | $K^+$-B | $Ca^{2+}$-A | $Ca^{2+}$-B |
|---|---|---|---|---|
| Storage lifetime [months] | 1 | 1.5 | 2.5 | 2 |
| Functional lifetime [days] | 30 | 45 | 1 | 3 |

### 3.3.7 Yield, reproducibility, cross-talk

The yield of functional chips is high: 80% of the $K^+$-selective chips and 70% of the $Ca^{2+}$-selective chips are functional. Several of the 30% $Ca^{2+}$-selective chips that are considered non functional do not present a response adequate for intracellular measurements, but present a response above pCa 6, adequate for extracellular measurements. As each chip has its own characteristics, especially $Ca^{2+}$-selective chips, which change with time, it is important to calibrate the platform before use, and follow the response evolution by regular recalibrations.

On a functional chip, the reproducibility of measurements of electrodes on a same array is excellent, as shown on figure 3.12. Typically, 13 out of the 16 electrodes on the chip present a similar behaviour in the first 10 days of use (if stored in 1 mM KCl, $10^{-4}$ M $CaCl_2$, respectively).

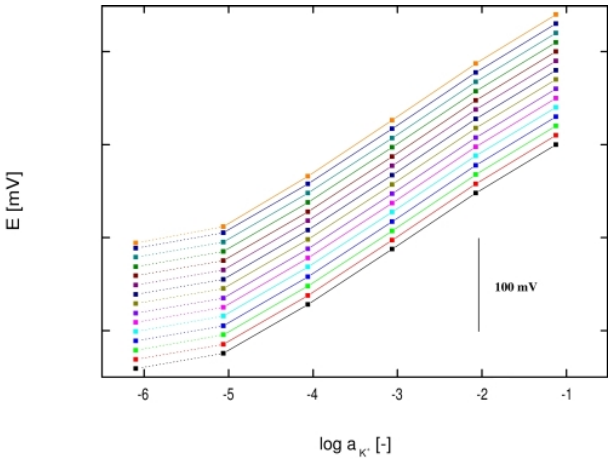


Figure 3.12: Calibration curves of a $K^+$-selective ISE array. Here the responses of 15 $\mu$ISE on a same platform are reported, showing an excellent response homogeneity over the whole array. The curves are offset for the sake of clarity.

After this time, the response of several electrodes, typically 5, starts to deviate, mainly by a loss of sensitivity, and the response homogeneity over the chip lowers. This development of slightly different responses over the same chip suggests the absence of cross-talk between the electrodes: each electrode has its history and evolutes individually.

### 3.3.8 Experiments in cell culture environment

The simplest method of using the platform is with an on-chip cell culture. To this aim, the biocompatibility of the platform has been successfully verified by culturing primary rat cardiomyocytes for 2 days and HepG2 human hepatoma cells for 6 days on arrays of $Ca^{2+}$-selective electrodes. Images of viable cultures are presented in figure 3.13.

The presence of organic material on the sensor surfaces in implantable devices, leading to biofouling, is a well-known problem [103, 104]. From these observations, it may be expected that the organic material present in the culture medium (e.g. serum) as well as the contact with the cells

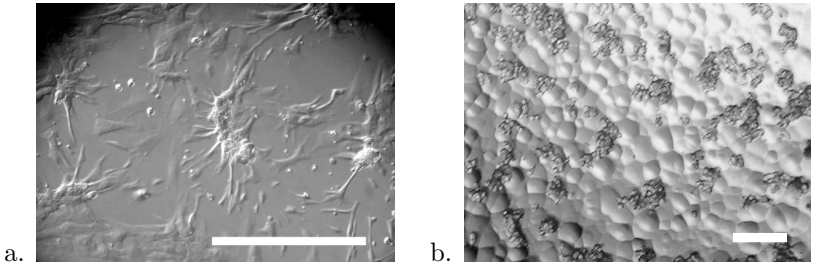

Figure 3.13: a. A 48 hours old culture of primary rat cardiomyocytes directly grown on the surface of the $\mu$ISE platform. Courtesy of Prof S. Rohr, University of Bern, Switzerland. b. A 3 days old culture of HepG2 human hepatoma cell culture on the platform. Courtesy of Prof. J-F. Dufour, University of Bern, Switzerland. Scale bars are 150 $\mu$m.

will lead to a degradation of the signal. The prolonged contact with organic material revealed to strongly affect the electrodes. The functional lifetime of the 1.5 $\mu$m diameter $K^+$-A microelectrodes is considerably shortened down to 6 days when the sensors are kept in a solution of intracellular concentrations of ions + HEPES, i.e. 150 mM NaCl, 5 mM KCl, 1.5 mM $MgCl_2$, 1.5 mM $CaCl_2$, 5 mM HEPES, and even shorter when the sensors are exposed to a culture medium supplemented with 5% foetal bovine serum (FBS). In this latter case, after 3 days the signal of 13 out of 15 sensors is completely lost, the remaining two presenting a sensitivity of 50.7 and 30.0 mV $dec^{-1}$. On the other hand, the 6 $\mu$m diameter $K^+$-B membrane electrodes seem to be less affected by biofouling in a serum-containing solution. After 1 day in Dulbeccos modified Eagle medium (DMEM) culture medium + 5% FBS + 1% penicillin-streptomycin, the sensors present a nearly Nernstian response of 57.0 $\pm$ 1.5 mV $dec^{-1}$, which lowers to 53.7 $\pm$ 7.0 mV $dec^{-1}$ after a supplementary day in a solution containing 5% serum and remains constant at 54.1 $\pm$ 6.5 mV $dec^{-1}$ after an additional day in contact with a solution containing 10% serum [93]. The observed difference might be simply due to the difference in ISE diameter, as the larger electrodes seem to be less affected by biofouling.

## 3.4 Summary

Potassium and calcium selective $\mu$ISE based on microfabricated protruding micropipettes of 50 $\mu$m height and 1.5 $\mu$m diameter have been characterized. As the platform is aimed at *in vitro* applications, the characterization has been performed using intracellular ionic concentrations for $Ca^{2+}$-selective electrodes and intra- and extracellular concentrations for $K^+$-selective electrodes.

The best membrane composition tested for potassium sensing was the following: 5 wt% valinomycin, 1 wt% potassium tetrakis[3,5-bis(trifluoromethyl)phenyl]borate, 89 wt% DOS, 5 wt% PVC; 100 mg membrane components dissolved in 210 $\mu$l cyclohexanone. The larger interference when working in cell cultures with valinomycin-based membranes is expected to be due to sodium ions. Calibrations of $\mu$ISE in 150 mM

NaCl background (extracellular concentration), showed a detection limit of pK 5.8, demonstrating that the interferences are negligible, and that the electrodes are adapted for both intra- and extracellular studies. The interference of $Mg^{2+}$ was also shown to be negligible. The lifetime is around a month. Typical drift values for both $K^{+}$- and $Ca^{2+}$-selective microelectrodes is around $5\pm3$ mV $h^{-1}$ after stabilization of the signal for 30 to 60 min.

The optimized $Ca^{2+}$-selective cocktail had the following composition: 0.46 wt% ETH 129, 0.09 wt% potassium tetrakis(4-chlorophenyl)borate, 85.45 wt% o-NPOE, 14 wt% PVC; 105 mg membrane components dissolved in 100 $\mu$l cyclohexanone (membrane $Ca^{2+}$-B). After 24 hours preconditioning in $CaCl_2$ $10^{-4}$ M, these electrodes present a nearly Nernstian or slightly super-Nernstian response and a detection limit of $10^{-9}$ M $Ca^{2+}$ in presence of intracellular concentrations of interfering ions. The presence of 14 wt% PVC permits a slowing of the diffusion of ions through the IS-membrane, inducing a more stable and nearly Nernstian response and the reaching of an extremely low detection limit. The extremely low detection limit is due to the utilization of the electrodes in non-equilibrium conditions, which however limits the lifetime to a few days of use. The detection limit subsequently rises to $10^{-6}$ M. For extracellular measurements, where the calcium concentration is in the millimolar range, the lifetime is in the order of two months.

# Bibliography

[1] Ammann D. *Ion-selective microelectrodes, principles, design and application.* Springer-Verlag, 1986. ISBN 0-387-16222-4.

[2] Wuhrmann P, Ineichen H, Riesen-Willi U, and Lezzi M. Change in nuclear potassium electrochemical activity and puffing of potassium-sensitive salivary chromosome regions during *Chironomus* development. *PNAS*, 76:806–808, 1977.

[3] Fry CH and Langley SEM. *Ion-selective electrodes for biological systems.* Harwood Academic Publishers, 2001. ISBN: 9058231070.

[4] Tsien RY and Rink TJ. Neutral carrier ion-selective microelectrodes for measurement of intracellular free calcium. *Biochim. Biophys. Acta*, 599:623–638, 1980.

[5] Marban E, Rink TJ, Tsien RW, and Tsien RY. Free calcium in heart muscle at rest and during contraction measured with $Ca^{2+}$-sensitive microelectrodes. *Nature*, 286:845–850, 1980.

[6] Thomas RC, Pagnotta SE, and Nistri A. Whole-cell recording of intracellular pH with silanized and oiled patch-type single or double-barreled microelectrodes. *Pflügers Arch. - Eur. J. Physiol.*, 447:259–265, 2003.

[7] Smith PJS, Hammar K, Porterfield HD, Sanger RH, and Trimarchi JR. Self-referencing, non-invasive, ion-selective electrode for single cell detection of trans-plasma membrane calcium flux. *Microsc. Res. Tech.*, 46:398–417, 1999.

[8] Kang TM, Markin VS, and Higelmann DW. Ion fluxes in giant excised cardiac membrane patches detected and quantified with ion-selective microelectrodes. *J. Gen. Physiol.*, 121:325–347, 2004.

[9] Uhlig A, Lindner E, Teutloff C, Schnakenberg U, and Hintsche R. Miniaturized ion-selective chip electrode for sensor application. *Anal. Chem.*, 69:4032–4038, 1997.

[10] Zhu JZ, Xie JF, Lu DR, Zhang GX, and Zhang ZR. Micromachined glucose sensor and $K^+$ ISE based on containment array. *Sens. Actuators B*, 65:157–159, 2000.

[11] Scheipers A, Wassmus O, Sundermeier C, Eshold J, Weiss Th, Gitter M, Ross B, and Knoll M. Potentiometric ion-selective silicon sensors for the on-line monitoring of blood electrolytes. *Anal. Chim. Acta*, 439:29–38, 2001.

[12] Yoon HJ, Shin JH, Lee SD, Nam H, Cha GS, Strong TD, and Brown RB. Solid-state ion sensors with a liquid junction-free polymer membrane-based reference electrode for blood analysis. *Sens. Actuators B*, 64:8–14, 2000.

[13] Gyurcsányi RE, Rangisetty N, Clifton S, Pendley BD, and Lindner E. Microfabricated ISEs: critical comparison of inherently conducting polymer and hydrogel based inner contacts. *Talanta*, 63:89–99, 2004.

[14] Lauks IR. Microfabricated biosensors and microanalytical systems for blood analysis. *Acc. Chem. Res.*, 31:317–324, 1998.

[15] Liao WY, Weng CH, Lee GB, and Chou TC. Development and characterization of an all-solid-state potentiometric biosensor array microfluidic device for multiple ion analysis. *Lab Chip*, 6:1362–1368, 2006.

[16] Hisamoto H, Yasuoka M, and Terabe S. Integration of multiple-ion-sensing on a capillary-assembled microchip. *Anal. Chim. Acta*, 556:164–170, 2006.

[17] Lenihan JS, Ball C, Gavalas VG, Lumpp JK, Hines J, Daunert S, and Bachas LG. Microfabrication of screen-printed nanoliter vials with embedded surface-modified electrodes. *Anal. Bioanal. Chem.*, 387:259–265, 2007.

[18] Lindner E and Umezawa Y. Performance evaluation criteria for preparation and measurement of macro- and microfabricated ion-selective electrodes. *Pure Appl. Chem.*, 80:85–104, 2008.

[19] Paciorek R, Bieganowski P, and Maj-Zurawska M. Miniature planar chloride electrodes. *Sens. Actuators B*, 108:840–844, 2005.

[20] Cosofret VV, Erdösy M, Johnson TA, Buck RP, Ash RB, and Neuman MR. Microfabricated sensor arrays sensitive to pH and $K^+$ for ionic distribution measurements in the beating heart. *Anal. Chem.*, 97:1647–1653, 1995.

[21] Lindner E and Buck RP. Microfabricated potentiometric electrodes and their in-vivo applications. *Anal. Chem.*, 72:336A–345A, 2000.

[22] ul Haque A, Rokkama M, De Carlo AR, Wereley ST, Rouxe SJ, Irazoqui PP, and Porterfield DM. A MEMS fabricated cell electrophysiology biochip for *in silico* calcium measurements. *Sens. Actuators B*, 123:391–399, 2007.

[23] Bakker E, Bühlmann P, and Pretsch E. Carrier-based ion-selective electrodes and bulk optodes. 1. General characteristics. *Chem. Rev.*, 97:3083–3132, 1997.

[24] Pioda LAR, Stankova V, and Simon W. Highly selective potassium ion responsive liquid-membrane electrode. *Anal. Lett.*, 2:665–674, 1969.

[25] Meier PC, Morf WE, Läubli M, and Simon W. Evaluation of the optimum composition of neutral-carrier membrane electrodes with incorporated cation-exchanger sites. *Anal. Chim. Acta*, 156:1–8, 1984.

[26] Wang CY, Hu XY, and Leng ZZ Jin GD. Nanomolar detection of amitriptyline by potentiometry with ion exchanger based PVC membrane ISEs. *Electroanalysis*, 15:709–714, 2003.

[27] Telting-Diaz M and Bakker E. Effect of lipophilic ion-exchanger leaching on the detection limit of carrier-based ion-selective electrodes. *Anal. Chem.*, 73:5582–5589, 2001.

[28] Berrocal MJ, Badr IHA, Gao D, and Bachas LG. Reducing the thrombogenicity of ion-selective electrode membranes through the use of a silicone-modified segmented polyurethane. *Anal. Chem.*, 73:5328–5333, 2001.

[29] Lindner E, Cosofret VV, Ufer S, Buck RP, Kao WJ, Neuman MR, and Anderson JM. Ion-selective membranes with low plasticizer content: electroanalytical characterization and biocompatibility studies. *J. Biomed. Mater. Res.*, 28:591–601, 1994.

[30] Yun SY, Hong YK, Oh BK, Cha GS, Nam H, Lee SB, and Jin J-L. Potentiometric properties of ion-selective electrode membranes based on segmented polyether urethane matrices. *Anal. Chem.*, 69:868–873, 1997.

[31] Cha GS, Meyerhoff ME, Cantor HC, Midgley AR, Goldberg HD, and Brown RB. Electrochemical performance, biocompatibility, and adhesion of new polymer matrices for solid-state ion sensors. *Anal. Chem.*, 63:1666–1672, 1991.

[32] Heng LY and Hall EAH. Producing "self-plasticizing" ion-selective membranes. *Anal. Chem.*, 72:42–51, 2000.

[33] Torres KYC, Garcia CAB, Fernandes JCB, de Oliveira Neto G, and Kubota LT. Use of self-plasticizing EVA membrane for potentiometric anion detection. *Talanta*, 53:807–814, 2001.

[34] Wydgladacz K, Durnas M, Parzuchowski P, Brzózka Z, and Malinowska E. Miniaturized sodium-selective sensors based on silicon back-side contact structure with novel self-plasticizing ion-selective membranes. *Sens. Actuators B*, 95:366–372, 2003.

[35] Reinhoudt DN, Engbersen JFJ, Brzózka Z, van den Vlekkert HH, Honlg GWN, Holterman HAJ, and Verkerk UH. Development of durable $K^+$-selective chemically modified field-effect transistors with functionalized polysiloxanes membranes. *Anal. Chem.*, 66:3618–3623, 1994.

[36] Bakker E and Pretsch E. Modern potentiometry. *Angew. Chem. Int. Ed.*, 46:5660–5668, 2007.

[37] Ceresa A, Sokalski T, and Pretsch E. Influence of key parameters on the lower detection limit and response function of solvent polymeric membrane ion-selective electrodes. *J. Electroanal. Chem.*, 501:70–76, 2001.

[38] Fouskaki M and Chaniotakis NA. Thick membrane, solid contact ion selective electrode for the detection of lead at picomolar levels. *Anal. Chem.*, 77:1780–1784, 2005.

[39] Zhu Z, Zhang J, Zhu J, Lu W, and Zi J. Fabrication and characterization of potassium ion-selective electrode based on porous silicon. *IEEE Sensors J.*, 7:38–42, 2007.

[40] Nägele M, Mi Y, Bakker E, and Pretsch E. Influence of lipophilic inert electrolytes on the selectivity of polymer membrane electrodes. *Anal. Chem.*, 70:1686–1691, 1998.

[41] Vigassy T, Gyurcsányi RE, and Pretsch E. Influence of incorporated lipophilic particles on ion fluxes through polymeric ion-selective membranes. *Electroanalysis*, 15:375–382, 2003.

[42] Morf WE. *The principles of ion-selective electrodes and of membrane transport.* Elsevier, 1981. ISBN 0-444-99749-0.

[43] Robinson RA and Stokes RH. *Electrolyte solutions.* Dover Publications Inc., second revised edition edition, 2002. ISBN 0-486-42225-9.

[44] Haase EA. *Untersuchung der Wechselwirkungen zwischen ionenselektiven Flüssigmembranen und Messgut im Hinblick auf die kontinuierliche Erfassung von Kationen im Vollblut.* PhD thesis, Swiss Federal Institute of Technology, 1993. Ph. D. Dissertation No. 10453.

[45] Meier PC. Two-parameter Debye-Hückel approximation for the evaluation of mean activity coefficients of 109 electrolytes. *Anal. Chim. Acta*, 136:363–368, 1982.

[46] Buck RP and Lindner E. Recommendations for nomenclature of ion-selective electrodes. *Pure Appl. Chem.*, 66:2527–2536, 1994.

[47] Bakker E. Determination of unbiased selectivity coefficients of neutral carrier-based cation-selective electrodes. *Anal. Chem.*, 69:1061–1069, 1997.

[48] Sokalski T, Zwickl T, Bakker E, and Pretsch E. Lowering the detection limit of solvent polymeric ion-selective electrodes. 1. Modeling the influence of steady-state ion fluxes. *Anal. Chem.*, 71:1204–1209, 1999.

[49] Naẅgele M, Bakker E, and Pretsch E. General description of the simultaneous response of potentiometric ionophore-based sensors to ions of different charge. *Anal. Chem.*, 71:1041–1048, 1999.

[50] Bakker E, Pretsch E, and Bühlmann P. Selectivity of potentiometric ion sensors. *Anal. Chem.*, 72:1127–1133, 2000.

[51] Umezawa Y, Umezawa K, and Sato H. Selectivity coefficients for ion-selective electrodes: recommended methods for reporting $K_{AB}^{pot}$ values. *Pure Appl. Chem.*, 67:507–518, 1995.

[52] Maccà C. The current usage of selectivity coefficients for the characterization of ion-selective electrodes. A critical survey of the 2000/2001 literature. *Electroanalysis*, 15:997–1010, 2003.

[53] Schefer U, Ammann D, Pretsch E, Oesch U, and Simon W. Neutral carrier based $Ca^{2+}$ selective electrode with detection limit in the sub-nanomolar range. *Anal. Chem.*, 58:2282–2285, 1986.

[54] Ceresa A. *Ion-selective polymeric membrane electrodes for potentiometric trace level measurements*. PhD thesis, Swiss Federal Institute of Technology, 2000. Ph. D. Dissertation No. 14209.

[55] Fu B, Bakker E, Yun JH, Yang VC, and Meyerhoff ME. Response mechanism of polymer membrane-based potentiometric polyion sensors. *Anal. Chem.*, 66:2250–2259, 1994.

[56] Sokalski T, Ceresa A, Zwickl T, and Pretsch E. Large improvement of the lower detection limit of ion-selective polymer membrane electrodes. *J. Am. Chem. Soc.*, 119:11347–11348, 1997.

[57] Mathison S and Bakker E. Effect of transmembrane electrolyte diffusion on the detection limit of carrier-based potentiometric ion sensors. *Anal. Chem.*, 70:303–309, 1998.

[58] Qin W, Zwickl T, and Pretsch E. Improved detection limits and unbiased selectivity coefficients obtained by using ion-exchange resins in the inner reference solution of ion-selective polymeric membrane electrodes. *Anal. Chem.*, 72:3236–3240, 2000.

[59] Sokalski T, Ceresa A, Fibbioli M, Zwickl T, Bakker E, and Pretsch E. Lowering the detection limit of solvent polymeric ion-selective membrane electrodes. 2. Influence of composition of sample and internal electrolyte solution. *Anal. Chem.*, 71:1210–1214, 1999.

[60] Morf WE, Badertscher M, Zwickl T, de Rooij NF, and Pretsch E. Effects of ion transport on the potential response of ionophore-based membrane electrodes: a theoretical approach. *J. Phys. Chem. B*, 103:11346–11356, 1999.

[61] Sokalski T and Lewenstam A. Application of Nernst-Planck and Poisson equations for interpretation of liquid-junction and membrane potentials in real-time and space domains. *Electrochem. Commun.*, 3:107–112, 2001.

[62] Sokalski T, Lingenfelter P, and Lewenstam P. Numerical solution of the coupled Nernst-Planck and Poisson equations for liquid junction and ion selective membrane potentials. *J. Phys. Chem. B*, 107:2443–2452, 2003.

[63] Lingenfelter P, Bedlechowicz-Sliwakowska I, Sokalski T, Maj-Zurawska M, and Lewenstam A. Time-dependent phenomena in the potential response of ion-selective electrodes treated by the Nernst-Planck-Poisson model. 1. Intramembrane processes and selectivity. *Anal. Chem.*, 78:6783–6791, 2006.

[64] Bakker E, Bühlmann P, and Pretsch E. The phase-boundary potential model. *Talanta*, 63:3–20, 2004.

[65] Bereczki R, Takács, Langmaier J B, Neely M, Gyurcsányi RE, Tóth K, Nagy G, and Lindner E. How to assess the limits of ion-selective electrodes: method for the determination of the ultimate span, response range, and selectivity coefficients of neutral carrier-based cation selective electrodes. *Anal. Chem.*, 78:942–950, 2006.

[66] Shultz MM, Stefanova OK, Mokrov SB, and Mikhelson KN. Potentiometric estimation of the stability constants of ion-ionophore complexes in ion-selective membranes by the sandwich membrane method: theory, advantages and limitations. *Anal. Chem.*, 74:510–517, 2002.

[67] Ceresa A, Sokalski T, and Pretsch E. Rational design of potentiometric trace level ion sensors. A $Ag^+$-selective electrodes with a 100 ppt detection limit. *Anal. Chem.*, 74:4027–4036, 2002.

[68] Morf WE, Pretsch E, and de Rooij NF. Computer simulation of ion-selective membrane electrodes and related systems by finite-difference procedures. *J. Electroanal. Chem.*, 602:43–54, 2007.

[69] Ceresa A, Pretsch E, and Bakker E. Direct potentiometric information on total ionic concentration. *Anal. Chem.*, 72:2050–2054, 2000.

[70] Shvarev A and Bakker E. Pulsed galvanostatic control of ionophore-based polymeric ion sensors. *Anal. Chem.*, 75:4541–4550, 2003.

[71] Shvarev A and Bakker E. Distinguishing free and total calcium with a single pulsed galvanostatic ion-selective electrode. *Talanta*, 63:195–200, 2004.

[72] Vigassy T, Morf WE, Badertscher M, Ceresa A, de Rooij NF, and Pretsch E. Making use of ion fluxes through potentiometric sensor membranes: ISEs with step responses at critical ion activities. *Sensors Actuators B*, 76:477–482, 2001.

[73] Morf WE, Badertscher M, Zwickl T, de Rooij NF, and Pretsch E. Effects of controlled current on the response behavior of polymeric membrane ion-selective electrodes. *J. Electroanal. Chem.*, 526:19–28, 2002.

[74] Tompa K, Birbaum K, Malon A, Vigassy T, Bakker E, and Pretsch E. Ion-selective supported liquid membranes placed under steady-state diffusion control. *Anal. Chem.*, 77:7801–7809, 2005.

[75] Bedlechowicz I, Sokalski T, Lewenstam A, and Maj-Zurawska M. Calcium ion-selective electrodes under galvanostatic current control. *Sens. Actuators B*, 108:836–839, 2005.

[76] Malon A, Bakker E, and Pretsch E. Backside calibration potentiometry: ion activity measurements with selective supported liquid membranes by calibrating from the inner side of the membrane. *Anal. Chem.*, 79:632–638, 2007.

[77] Buck RP. Ion selective electrodes. *Anal. Chem.*, 48:23R–39R, 1976.

[78] Fibbioli M, Morf WE, Badertscher M, de Rooij NF, and Pretsch E. Potential drifts of solid-contacted ion-selective electrodes due to zero-current ion fluxes through the sensor membrane. *Electroanalysis*, 12:1286–1292, 2000.

[79] Paciorek R, van der Wal PD, de Rooij NF, and Maj-Zurawska M. Optimization of the composition of interfaces in miniature planar chloride electrodes. *Electroanalysis*, 15:1314–1318, 2003.

[80] van der Wal PD, Zielinska-Paciorek R, and de Rooij NF. Covalently bound plasticized PVC membranes for solid state ion-selective devices. *Chimia*, 57:643–645, 2003.

[81] Bobacka J. Conducting polymer-based solid-state ion-selective electrodes. *Electroanalysis*, 18:7–18, 2006.

[82] Michalska A. Optimizing the analytical performance and construction of ion-selective electrodes with conducting polymer-based ion-to-electron transducers. *Anal. Bioanal. Chem.*, 384:391–406, 2006.

[83] Grygolowicz-Pawlak E, Wygladacz K, Sek S, Bilewicz R, Brzózka Z, and Malinowska E. Studies on ferrocene organothiol monolayer as an intermediate phase potentiometric sensor with gold inner contact. *Sens. Actuators B*, 111:310–316, 2005.

[84] Grygolowicz-Pawlak E, Plachecka K, Brzózka Z, and Malinowska E. Further studies on the role of redox-active monolayer as intermediate phase of solid-state sensors. *Sens. Actuators B*, 123:480–487, 2007.

[85] Mamińska R, Dybko A, and Wróblewski W. All-solid-state miniaturised planar reference electrodes based on ionic liquids. *Sens. Actuators B*, 115:552–557, 2006.

[86] Mamińska R, Kucharek M, Jozwiak P, Garbarczyk J, Dybko A, and Wróblewski W. AgI-$Ag_2O$-$V_2O_5$ glasses as ion-to-electron transducers for the construction of all-solid-state microelectrodes. *Microchim. Acta*, 159:311–318, 2007.

[87] Buck RP and Shepard R. Reversible metal/salt interfaces and the relation of second kind and "all-solid-state" membrane electrodes. *Anal. Chem.*, 46:2097–2103, 1974.

[88] Dybko A. Errors in chemical sensor measurements. *Sensors*, 1:29–37, 2001.

[89] van den Winkel P, Mertens J, and Massart DL. Streaming potentials in automatic potentiometric systems. *Anal. Chem.*, 46:1765–1768, 1974.

[90] Purves R D. *Microelectrode methods for intracellular recording and ionophoresis*. Academic Press, 1981.

[91] Patton C, Thompson S, and Epel D. Some precautions in using chelators to buffer metals in biological solutions. *Cell Calcium*, 35:427–431, 2004.

[92] Bers DM, Patton CW, and Nuccitelli R. *A practical guide to the preparation of $Ca^{2+}$ buffers*, volume 40 of *Methods in Cell Biology*. Academic Press, 1994. ISBN 0-12-164717-X.

[93] Guenat OT, Generelli S, de Rooij NF, Koudelka-Hep M, Berthiaume F, and Yarmush ML. Development of an array of ion-selective microelectrodes aimed for the monitoring of extracellular ionic activities. *Anal. Chem.*, 78:7453–7460, 2006.

[94] Knowles A and Shabala S. Overcoming the problem of non-ideal liquid ion-exchanger selectivity in microelectrode ion flux measurements. *J. Membrane Biol.*, 202:51–59, 2004.

[95] Oehme M, Kessler M, and Simon W. Neutral carrier $Ca^{2+}$-microelectrode. *Chimia*, 30:204–206, 1976.

[96] Ammann D, Güggi M, Pretsch E, and Simon W. Improved calcium ion-selective electrode based on a neutral carrier. *Anal. Lett.*, 8:709–720, 1975.

[97] Pretsch E, Ammann D, Osswald HF, Güggi M, and Simon W. Ionophore vom Typ der 3-oxapentandiamide. *Helv. Chim. Acta*, 63:191–196, 1980.

[98] Armstrong RD and Todd M. Study of calcium ion selective electrodes containing Simon ionophores using impedance methods. Interfacial properties. *J. Electroanal. Chem.*, 266:175–177, 1989.

[99] Södergård M, Csóka, Nagy G, and Ivaska A. Lowering the detection limit of solvent polymeric ion-selective membrane electrodes. An experimental study with calcium-selective micropipette electrodes. *Anal. Lett.*, 36:2909–2923, 2003.

[100] Qin Y and Bakker E. Quantification of the concentration of ionic impurities in polymeric sensing membranes with the segmented sandwich technique. *Anal. Chem.*, 73:4262–4267, 2001.

[101] Konopka A, Sokalski T, Lewenstam A, and Maj-Zurawska M. The influence of the conditioning procedure on potentiometric characteristics of solid contact calcium-selective electrodes in nanomolar concentration solutions. *Electroanalysis*, 22:2232–2242, 2006.

[102] Moss SR, Janata J, and Johnson CC. Potassium ion-sensitive field effect transistor. *Anal. Chem.*, 47:2238–2243, 1975.

[103] Li CM, Dong H, Cao XD, Luong JHT, and Zhang XJ. Implantable electrochemical sensors for biomedical and clinical applications: progress, problems, and future possibilities. *Curr. Med. Chem.*, 14:937–951, 2007.

[104] Wisniewski N and Reichert M. Methods for reducing biosensor membrane biofouling. *Colloids Surfaces B: Biointerfaces*, 18:197–219, 2000.

# Chapter 4

# Cellular potassium efflux quantification

## 4.1 Introduction

In this chapter, the feasibility of using $K^+$-selective microelectrode arrays for monitoring an induced $K^+$ efflux in kidney cells is evaluated. The potassium efflux was induced by a lowering of osmolarity in the medium where cells were suspended. The hypo-osmotic shock first causes swelling of the cells and then cell lysis. Thus potassium, which is present at high levels in intact viable cells, leaks out of dying cells and rises the extracellular potassium concentration.

Cellular death can follow two different pathways: necrosis or apoptosis. Necrosis is induced by accidental cell damage, due to an acute toxic event. It brings a loss of regulation of ion homeostasis, and the subsequent cell swelling, followed by the loss of cell membrane integrity and cell lysis. Apoptosis, also called programmed cell death, is a process occurring under normal physiological conditions, and occurs to eliminate unnecessary or unwanted cells. Apoptotic cells are active participants of the death process. Apoptosis is characterized by cell shrinkage, and ends

with the fragmentation of cells in smaller bodies, the apoptotic bodies, rapidly eliminated by the organism. *In vitro*, the apoptotic bodies and the remaining cell fragments swell, and finally lyse [1].

In apoptosis, $K^+$ loss occurs in the early stage of the death pathway, prior to caspase activation, which is considered the point of no return of apoptosis [2]. In a similar way, cells exposed to a lowering in medium osmolarity will swell and, in response to the volume change, a $K^+$ efflux will start. This ionic efflux is a protective mechanism of the cell to balance the osmolarity between intra- and extracellular spaces and to prevent cell breakdown caused by excessive swelling. However, if the lowering of osmolarity becomes critical, the cell will lyse, liberating the totality of the intracellular potassium. Despite the fundamental differences between necrosis and apoptosis, both hypoosmotic shock-induced necrosis and apoptosis rely on the similar mechanism of cell volume regulation inducing a $K^+$ cellular efflux [3].

Because of its simplicity, the hypo-osmotic shock assay, with the subsequent intracellular potassium release, was used to test the applicability of the $\mu$ISE array to the use with biological samples. The potassium-selective $\mu$ISE have been used as a cell death indicators by monitoring in real time the potassium concentration increase in extracellular environment. As the osmolarity in the cell culture microwell lowers gradually, the cells start to release potassium ions. When the osmolarity becomes critically low, lysis occurs (see also figure 4.2).

Microfluidic toxicological assays have gained importance in these last years. Some examples can be found in very recent publications [4, 5, 6, 7, 8, 9]. They mostly rely on the observation of cell lysis, by fluorescence. The methodology based on the identification of $K^+$ cell efflux can be considered as complementary to fluorescence. As $K^+$ efflux begins before cellular membrane disruption, the cellular disease is detectable before the complete cellular lysis.
Potassium ion fluxes in cellular cultures are mainly traced using radioactive tracers, for example $^{42}K$, $^{68}Rb$ [10, 11, 12]. Alternative methods for the quantification of cellular ion fluxes are fluorescence techniques

[13, 14] and patch clamp [14]. Recently, the realization of several microfabricated patch clamp arrays has been reported [15, 16, 17] (the latter also used as electroporation device [18]), rendering the technique more interesting for high throughput toxicology aims. Glass capillary ion-selective microelectrodes have been employed in measurement of potassium efflux during apoptosis (see for example [3, 19, 20]). Some of the possible improvements of this technique through microfabrication are multiple parallel recordings, integration of a microfluidic system to easily switch between different sample solutions and cellular samples and system automation.

In order to assess the performance of the platform, the release of the intracellular potassium monitored by potassium-selective microelectrodes was completed by cell lysis observation by fluorescence microscopy.

## 4.2 Materials and methods

### Chemicals

The potassium-selective membrane, whose characterization is presented in chapter 3, had the following composition: 5 wt% ionophore valinomycin, 1 wt% (potassium tetrakis[3,5-bis(trifluoromethyl)phenyl]borate, 89 wt% plasticizer bis(2-ethylhexyl) sebacate (DOS), 5 wt% membrane matrix high molecular weight PVC. The membrane components (totaling 200 mg) were dissolved in 420 $\mu$l cyclohexanone. All the membrane cocktail components were Selectophore grade, from Fluka. NaCl salt was of Suprapur quality, Merck. Aqueous solutions were prepared with biology grade deionized water (>18.3 M$\Omega$ cm specific resistance).
Hybridoma serum free medium (Hyridoma-SFM, Formula 03-5106RH) and geneticin (G418, Cat# 10131-027) were from Gibco, Invitrogen. Fortified bovine calf serum (Cat# SH3008703) was from HyClone and HEPES ($\geq$98 %) from Fisher BioReagents. D-glucose ($\geq$99.5 %, mouse embryo tested), sodium bicarbonate ($\geq$99.5 %, cell culture tested), L-glutamine ($\geq$99%, cell culture tested) and Pluronic F68 (cell culture tested) were all from Sigma.

### Microfabricated platforms

The MGH platforms were used (see chapter 2 for details). The array comprised 6 $\mu$m diameter, 50 $\mu$m long protruding micropipettes, located in a 360 $\mu$m deep microwell. The ISEs were preconditioned in 1 mM KCl solution for 1 day before use, and subsequently stored in this same solution in between experiments. The electrodes functionality was tested by recording a calibration curve in the absence of cells with calibration solutions going from $10^{-7}$ M to $2{\cdot}10^{-1}$ M $K^+$ in 150 mM NaCl background (1 point/decade). Calibration curves were recorded under flow conditions, using a flow rate of 21 $\mu$l $s^{-1}$. Each calibration solution was pumped for 5 minutes. Data were recorded during the last 10 s before switching to the next solution. Chips presenting a linear response, a sensitivity comprised between 50 mV $pK^{-1}$ and 60 mV $pK^{-1}$ and a detection limit near $10^{-5}$ M $K^+$ in 150 mM NaCl background were considered to be functional.

### Cell culture medium and conditions

Human embryo kidney cells (293-EBNA cells) were kindly provided by Dr. Yves Durocher from Biotechnology Research Institute (Canada National Research Council, Montreal, Canada). Cells were maintained in hybridoma serum free medium (HSFM) supplemented with 1% fortified bovine calf serum, 25 mM D-glucose, 30 mM sodium bicarbonate, 6 mM L-glutamine, 10 mM HEPES, 0.05 mg $ml^{-1}$ geneticin and 0.1% Pluronic F68. After 3 months of maintenance (30 passages), the cells were discarded and a new aliquot was thawed out of the Master Cell Bank (kept in liquid nitrogen). Cells were maintained in 75 $cm^2$ T-flasks with vented cap (Corning Life Sciences) at 37°C and 5% $CO_2$ atmosphere and were subcultured every 2 to 3 days. Cells were inoculated at $1.5{\cdot}10^5$ cells $ml^{-1}$ to $2{\cdot}10^5$ cells $ml^{-1}$ in their exponential growth phase, and harvest was assured at a density inferior to $10^6$ cells $ml^{-1}$. The cells concentration was determined by a hemacytometer, and cell viability was determined by Trypan blue exclusion method.

### Experimental setup

Fluorescence microscopy observations and ISE recordings have been performed in a microfluidic measuring chamber comprising two sub-chambers: a 650 nl cell culture microwell (MGH design chip), etched in silicon and a PDMS flow-through chamber, having a volume of 30 $\mu$l for microscopy assays and 11 $\mu$l for electrochemical tests. The cell suspension was pipetted into the microwell where cells were confined with the help of a PET microporous membrane (Becton Dickinson, 1 $\mu$m pore size PET membrane, # 353102). This membrane separates the microwell and the flow-through chamber and traps the suspended cells in the microwell, while permitting the ionic diffusion between the two sub-chambers (figure 4.1). At the bottom of the figure 4.1 is shown the silicon based microwell with two micropipettes filled with ion-selective membrane. The upper PDMS flow-through chamber is closed by a PMMA fixture.

The potentiometric measurement and the microscopic observation could not be performed simultaneously, since the microscope was not equipped with a Faraday cage (needed for potentiometric measurement) and the flow-through manifold used for the potentiometric measurement was too large to fit on the microscope. Notwithstanding the differences between

a.

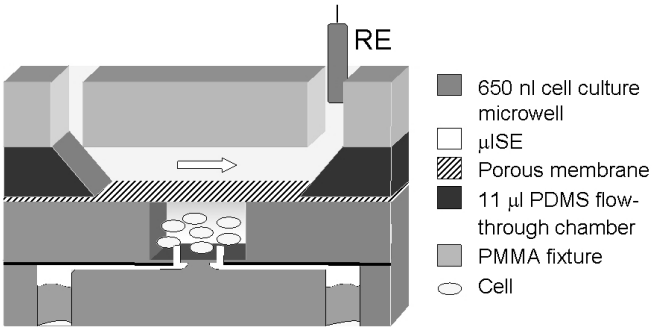


Figure 4.1: a. Schematic cross-section of the potentiometric experimental set-up. In the microscopy setup, the PMMA fixture is replaced by a coverglass.

the potentiometric and fluorescence microscopy setups, there is no significant difference in concentration gradients, thus for the same cellular concentration the lysis kinetics in the two experimental setups is equivalent.

## Experimental procedure

*Fluorescence microscopy.*
The fluorescence images were obtained with a Zeiss AxioImager D1 upright microscope equipped with a 20x long working distance objective, coupled to a Zeiss AxioCam HRm cooled monochrome digital camera and the AxioVision v. 4.6 software.
Methods: The cells were harvested during 24 hours post inoculation, at a density of $5{\cdot}10^5$ cells $ml^{-1}$ to guarantee a similar physiological state throughout all experiments. To eliminate the culture medium, the cells were centrifuged using a Durafuge Precision centrifuge (Thermo Electron Corporation) at 200 g, 4°C, for 5 min. The cell pellets were resuspended to a concentration of circa 4 millions $ml^{-1}$ in a solution of 2 $\mu$M calcein AM (live/dead assay) and 150 mM NaCl, and incubated for 15 min at ambient temperature. The excess calcein AM was eliminated by centrifugation and the cells resuspended in the same volume of a solution of 4 $\mu$M ethidium homodimer-1 and 150 mM NaCl. The cells were then transferred to the microwell and trapped with the microporous membrane. Cell lysis was induced by adding a drop of water into the PDMS chamber of 30 $\mu$l volume, subsequently covered with a coverglass. Only calcein AM was useful to follow the cell lysis, ethidium homodimer was used exclusively to verify the culture viability.

*Potentiometric recordings.*
Potentiometric measurements were performed with a home made high-impedance input amplifier, in combination with a data acquisition system controlled with the Labview software. The details of the experimental set-up and of the acquisition system are described in section 3.3.1. The whole microfluidic measuring chamber was mounted in a PMMA flow-through manifold that integrated a mini reference electrode (DRIREF-2, World Precision Instruments), located downstream (figure 4.1). The flow-through manifold and the amplifier were placed in a Fara-

day cage in order to avoid external perturbations and light interferences. Methods: The cells were harvested during 24 hours post inoculation, at a density of $5{\cdot}10^5$ cells $ml^{-1}$ to guarantee a similar physiological state throughout all experiments. Cell concentration was realized by centrifugation at 200 g, 4°C, for 5 min. The cells were rinsed twofold in 1.8 ml of freshly prepared 150 mM NaCl, followed by centrifugation and elimination of the supernatant solution. The cells pellet was then resuspended in 150 mM NaCl, diluted to the desired concentration and transferred into the cell culture microwell. Before the measurement, to stabilize the potentiometric response for low concentrations, the chips were conditioned for 1h in 150 mM NaCl + $10^{-7}$ M KCl. Reproducibility of the measuring conditions was achieved by following a strict experimental procedure. The experiment was divided in four parts (also reported in table 4.1):

1. Rinsing: elimination of the remaining extracellular potassium by rinsing the flow-through manifold with a 150 mM NaCl solution. The microwell and flow-through chamber are allowed to equilibrate, the extracellular components remaining in the microwell diffuse through the porous membrane. Two pumping-rest cycles were allowed to improve the purge.

2. Lysis assay: injection of deionized water during 1.5 min and initiation of the cell lysis that was monitored for the subsequent 15 min. The pumping time needed for the solutions to reach the flow-through chamber being 30 s, the effective water flowing time in the chamber is 1 min. The potentiometric data used for the potassium corresponding activity calculations were collected after 4 min and 15 min of osmolarity diminution, during a 10 s interval.

Table 4.1: Hypo-osmotic shock ISE recording, experimental procedure.

| | Rinsing | | | | | Lysis assay | | Rinsing | | | Calibration |
|---|---|---|---|---|---|---|---|---|---|---|---|
| Solution | NaCl 150 mM | | | | | $H_2O$ | | $H_2O$ | NaCl 150 mM | | Standard solutions |
| t [min] | 3 | 4 | 3 | 2 | 3 | 1.5 | 15 | 3 | 3 | 10 | 7x5 |
| Mode | D | S | D | S | D | D | S | D | D | S | D |

S: static mode, no solution is pumped through the system.

D: dynamic mode, pumping rate 21 $\mu l\ s^{-1}$.

3. Rinsing of the flow-through manifold with $H_2O$ and 150 mM NaCl, followed by 10 min resting time to allow the diffusion of the remaining ions/molecules out of the microwell.

4. Calibration of the microelectrodes is performed by continuous injection of standard solutions of increasing concentrations. After 5 min an interval of 10 s is recorded, and the solution is changed to the next. The slopes of the calibration curves were calculated in the linear concentration range between $10^{-4}$ M and 0.2 M KCl. The activity coefficients were calculated based on the modified Debye-Hückel theory (see section 3.2.3).

During the whole of the experiment, the flow rate was either at 21 $\mu$l $s^{-1}$ or zero, as given in table 4.1. All measurements were carried out at room temperature (22±3°C).

## 4.3 Results and discussion

The hypoosmotic shock procedure was carried out by first allowing the cells to equilibrate their osmotic pressure in a 150 mM NaCl medium, and then rapidly replacing the sodium chloride solution in the flow-through chamber with deionized water. Sodium chloride diffuses out of the microwell through the porous membrane, which results in an overpressure of the cytosol, causing the cells to swell, and finally to lyse.

### 4.3.1 Fluorescence microscopy

Cellular lysis was observed by fluorescence microscopy by using a live/dead assay. Calcein AM readily penetrates cells and is cleaved by intracellular esterases into a fluorescent analogue only in viable cells. The suspended cells slowly decant at the bottom of the microwell, allowing the observation of all the trapped cells. The fluorescent observation can thus be compared to the potentiometric assay. Figure 4.2 shows fluorescence images of the cells at three different times: at the beginning of the experiment, after 4 min and after 15 min from the start of osmolarity decrease in the microwell. The swelling of the cells due to the osmotic pressure

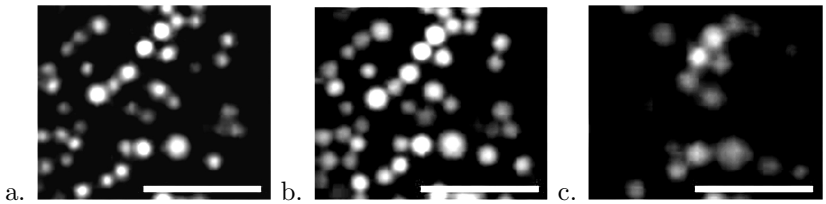


Figure 4.2: Fluorescence microscopy images of cell lysis in the microwell at three different times: a. start. b. after 4 min of medium dilution. c. after 15 min. Scale bars are 100 $\mu$m.

difference can clearly be seen along the whole process. As cells burst, calcein abruptly leaks out and the cell disappears from the fluorescence image.

The efficiency of cell lysis was quantified by counting the remaining intact cells in the microwell at different times during the lysis process. The results presented in figures 4.2.a-b and 4.4 demonstrate that the lysis process starts 5 minutes after the beginning of the NaCl diffusion out of the microwell, suggesting that the viability of the cells is not immediately affected by the decrease of medium osmolarity.

### 4.3.2 Potentiometric recordings

Figure 4.3 shows potentiometric signals recorded during the overall lysis assay. The different phases of the experimental procedure are indicated. In the beginning, while sodium chloride is flowing through the manifold, the potassium concentration is at its lowest level. As soon as deionized water replaces the background electrolyte in the upper chamber at the start of the lysis assay, a peak is seen for both assays (with and without cells). This increase of the potential response of the ISE is systematically observed when pumping occurs. Then, as the medium osmolarity decreases, the potassium concentration increases proportionally to the amount of cells present in the microwell. In parallel, the assay in absence of cells stayed at a low potassium concentration level during the whole

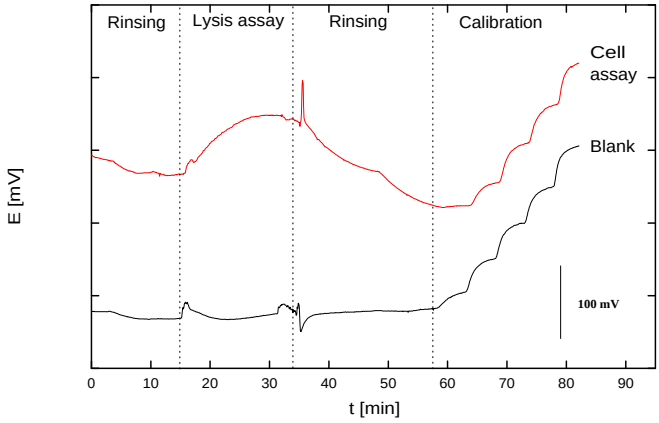


Figure 4.3: Potentiometric recordings of the cell lysis assay. The $K^+$ concentration increase due to cell lysis is clearly visible on the cell-containing assay (top curve), while no potential increase is registered in the blank assay.

period. The electrodes being insensitive to $Na^+$ changes in this concentration range (see section 3.3.3) the potential remains stable. After cell lysis, the potassium concentration decreases to its initial level due to the rinsing of the manifold with water and 150 mM NaCl. Finally the microelectrodes are calibrated with 150 mM NaCl background electrolyte standard solutions. The presence of multiple electrodes in the microwell allows a statistically more precise concentration measurement. It must be pointed out that the sensitivity of the microelectrodes remained unchanged before and after the experiment.

In figure 4.4, the lysis kinetics based on fluorescence observation and potentiometric signal recorded during the lysis assay are compared. While the potentiometric potassium signal increases very rapidly immediately after the pumping of water in the flow-though chamber the cell lysis starts only after several minutes. The plateau visible on the potentiometric signal in figure 4.4 between minutes 1 and 2 is an artefact coming probably from the formation of a junction potential caused by water

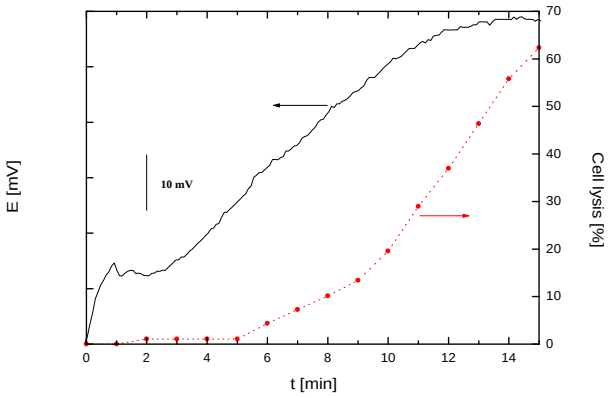


Figure 4.4: Cell lysis quantification based on fluorescence imaging (dotted line) versus potentiometric $K^+$ signal (continuous line).

pumping. The important potassium efflux which takes place even in the absence of cell lysis is induced by a mechanism of cell volume regulation, known as regulatory volume decrease (RVD) [11, 21] used by cells to prevent lysis in hypotonic media.

The lysis assay was repeated for several cell concentrations. The corresponding potassium activity in the microwell was evaluated by matching the potential recorded during the lysis assay with the calibration curve. As expected, a linear relation between the number of cells in the microwell and the potassium release was found (figure 4.5). The potassium activity was evaluated before the start of cell lysis and after the lysis of the majority of the cells, where the potassium signal is near its maximum. This corresponds to respectively 4 min and 15 min after the injection of water in the flow-through chamber. The possibility of cell quantification from the $K^+$ efflux prior to cell lysis suggests the possibility to apply the platform to detect and quantify cellular apoptosis in its early stage, before the death of the cell.
The linearity of the response indicates that the microelectrodes are not affected by the presence of cellular debris. After a dozen assays the

quality of the signal is not degraded, giving evidence of an easy removal of cellular debris by water rinsing. On the other hand, the calibration recordings in figure 4.3 show a detection limit slightly different in presence or in absence of cells, meaning that the presence of cellular material biases the detection limit. In the present tests this phenomenon is negligible, but it could be a limiting factor in the case of an apoptosis assay, where the death of a small fraction of cells could be masked by the background signal.

Under the present experimental conditions, after 15 minutes the potassium signal is at its maximum, and in the case presented in figure 4.5, it corresponds to a detection limit of 200 cells. The cellular quantification with the data collected before the start of cell lysis, i.e. 4 min after the start of osmolarity diminution in the microwell, is limited to 1000 cells. The detection limit of the platform is limited by the dilution of the potassium in the microwell. With a redesign of the microwell avoiding the dilution of the $K^+$, the efflux of a single cell is expected to

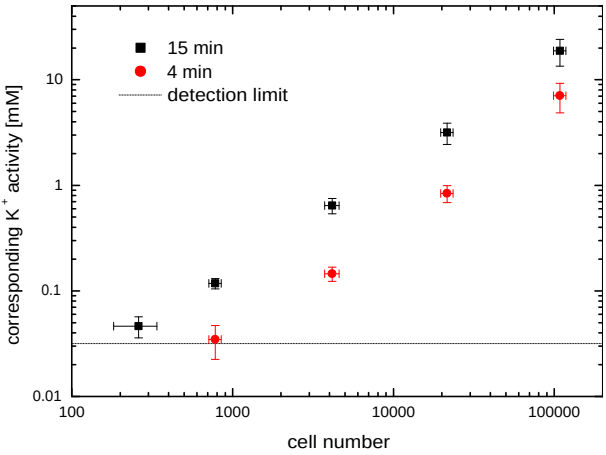


Figure 4.5: Corresponding measured potassium activity in function of the cell sample concentration, calculated at 4 min (circles) or 15 min (squares) after the start of the lysis assay. The line represents the detection limit of the ISE.

be measurable.
It must be pointed out that the detection limit can vary between two series of measurements. Differences can come from both the cell culture and the $\mu$ISE. We expect a different reaction for every cell type, but also mutations leading to a change in sensitivity to osmotic shocks on the same cell culture. Similarly, as every chip present slightly different characteristics, the detection limit and sensitivity need to be tested prior to use.

## 4.4 Summary

Potassium ion is one of the key cellular components. Its fluxes can be used to study many different cellular processes such as lysis, apoptosis and necrosis and exploited for example in toxicological screening assays. The sensitivity of the developed $K^+$-selective microelectrode platform allows to detect, in the actual non-optimal setup geometry, the lysis of only 200 cells. With an adequate redesign of the platform providing an automatic sample loading and especially smaller chamber volume avoiding the dilution of potassium released by the cells, the detection of a single cell lysis should be possible. Furthermore, the pre- and post-lysis calibration curves have shown that the cellular debris did not cause the fouling of the ion-selective microelectrodes allowing thus the platform to be used for a number of experiments.

# Bibliography


[1] Roche Diagnostics AG. *Apoptosis, cell death and cell proliferation manual*, $3^{rd}$ edition.
http://www.roche-applied-science.com/sis/apoptosis/docs/manual_apoptosis.pdf.

[2] Hughes F and Cidlowski J. Potassium is a critical regulator of apoptotic enzymes *in vitro* and *in vivo*. *Adv. Enzyme Regul.*, 39:157–171, 1999.

[3] Trimarchi JR, Liu L, Smith PJS, and Keefe DL. Apoptosis recruits two-pore domain potassium channels used for homeostatic volume regulation. *Am. J. Cell Physiol.*, 282:C588–C594, 2002.

[4] Baudoin R, Corlu A, Griscom L, Legallais C, and Leclerc E. Trends in development of microfluidic cell biochips for *in vitro* hepatotoxicity. *Toxicol. in Vitro*, 21:535–544, 2007.

[5] Wang Z, Kim M-C, Marquez M, and Thorsen T. High-density microfluidic arrays for cell cytotoxicity analysis. *Lab Chip*, 7:740–745, 2007.

[6] Ceriotti L, Ponti J, Colpo P, Sabbioni E, and Rossi F. Assessment of cytotoxicity by impedance spectroscopy. *Biosens. Bioelectronics*, 22:3057–3063, 2007.

[7] Eisenbrand G, Pool-Zobel B, Baker V, Balls M, Blaauboer BJ, Boobis A, Carere A, Kevekordes S, Lhuguenot J-C, Pieters R, and Kleiner J. Methods of *in vitro* toxicology. *Food and Chemical Toxicology*, 40:193–236, 2002.

[8] Marentis TC, Kusler B, Yaraliglu GG, Liu S, Haeggstrom EO, and Khuri-Yakub BT. Microfluidic sonicator for real-time disruption of eukaryotic cells and bacterial spores for DNA analysis. *Ultrasound in Med. and Biol.*, 31:1265–1277, 2005.

[9] Irimia D, Tompkins RG, and Toner M. Single-cell chemical lysis in picoliter-scale closed volumes using a microfabricated device. *Anal. Chem.*, 76:6137–6143, 2004.

[10] Junankar PR, Karjalainen A, and Kirk K. Osmotic swelling activates two pathways for $K^+$ efflux in a rat hepatoma cell line. *Cell. Physiol. Biochem.*, 14:143–154, 2004.

[11] Pesantes-Morales H, Lezama RA, Ramos-Mandujano G, and Tuz KL. Mechanisms of cell volume regulation in hypo-osmolality. *Am. J. Med.*, 119:S4–S11, 2006.

[12] Gill S, Gill R, Wicks D, and Liang D. A cell based $Rb^+$ flux assay of the Kv1.3 potassium channel. *Assay Drug Deliv. Technol.*, 5:373–380, 2007.

[13] Beeton C, Wulff H, Singh S, Botsko S, Crossley G, Gutman CA, Cahalan MD, Pennington M, and Chandly KG. A novel fluorescent toxin to detect and investigate Kv1.3 channel up-regulation in chronically activated T lymphocytes. *J. Biol. Chem.*, 278:9928–9937, 2003.

[14] Xu J, Wang X, Ensign B, Li M, Wu L, Guia A, and Xu J. Ion-channel assay technologies: *quo vadis ? Drug Disc. Today*, 6:1278–1287, 2001.

[15] Finkel A, Wittel A, Yang N, Handran S, Hughes J, and Costantin J. Population patch clamp improves data consistency and success rates in measurement of ionic current. *J. Biomolec. Screening*, 11:488–496, 2006.

[16] Klemic KG, Klemic JF, Reed MA, and Sigworth FJ. Micromolded PDMS planar electrode allows patch clamp electrical recordings from cells. *Biosens. Bioel.*, 17:597–604, 2002.

[17] Seo J, Ionescu-Zanetti C, Diamond J, Lal R, and Lee LP. Integrated multiple patch-clamp array chip via lateral cell trapping junctions. *Appl. Phys. Lett.*, 84:1973–1975, 2004.

[18] Khine M, Lau A, Ionescu-Zanetti C, Seo J, and Lee LP. A single cell electroporation chip. *Lab Chip*, 5:38–43, 2005.

[19] Hrabetova H, Chen KC, Masri D, and Nicholson C. Water compartmentalization and spread of ischemic injury in thick-slice ischemia model. *J. Cereb. Blood Flow Metabol.*, 22:80–88, 2002.

[20] Kang TM, Markin VS, and Higelmann DW. Ion fluxes in giant excised cardiac membrane patches detected and quantified with ion-selective microelectrodes. *J. Gen. Physiol.*, 121:325–347, 2004.

[21] Cheung RK, Grinstein S, Dosch H-M, and Gelfand EW. Volume regulation by human lymphocytes: characterization of the ionic basis for regulatory volume decrease. *J. Cell. Physiol.*, 112:189–196, 1982.

# Chapter 5

# A $\mu$ISE-electroporation hybrid platform

## 5.1 Introduction

One of the main interests of microfabrication technologies is the possibility to integrate all necessary functionalities to load, manipulate and analyze the sample on the same platform [1, 2]. As the study of intracellular components is of particular interest, preliminary tests of cellular lysis by irreversible electroporation have been performed.
Intracellular measurements using glass capillary $\mu$ISE are performed by manually inserting the electrode in the cells. As the present silicon based platform is not adapted for cell impalement, two other alternatives to access the intracellular medium have been considered: cell membrane opening by electroporation induced cell lysis and perforated patch clamp.

Practical difficulties in implementing a patch clamp system in parallel with the $\mu$ISE (discussed in more detail in section 5.7) have lead us to choose a method for cell membrane rupture based on electrical pulses. Electroporation is a technique using electrical pulses to destabilize the cellular membrane. Cell lysis by electroporation can be induced in the

immediate vicinity of the ionic sensor, thus allowing measurements on the intracellular material. Electroporation can not only induce the cellular lysis (irreversible electroporation), but can also open transient pores in the cell membrane, that will reseal without cell death (reversible electroporation). The reversible electroporation phenomenon is widely used in cell manipulation, especially in genetic engineering, to introduce cellular impermeant molecules in cells. An interesting application is *in vivo* drug delivery in cancerous cells of relatively impermeable drugs or therapeutic genes [3].

The applicability of spatially controlled electroporation in parallel to potentiometric recordings has been investigated. Local electroporation is realized by metallic electrodes patterned at the surface of the platform. To this aim, the $\mu$ISE sensor array has been combined with an array of thin film Pt microelectrodes surrounding the ion-selective electrodes. The geometry of a combined $\mu$ISE-Pt electrode is illustrated in figure 5.3, for other illustrations on the array geometry, refer to chapter 2. The presence of a metallic thin film electrode array opens further possibilites for cellular manipulations and study. Metallic electrode array applications found in the literature comprise the attraction of cells by dielectrophoresis [4], electrophysiological studies, electrical activity monitoring of a cell culture [5], pseudo-reference electrode, local electroporation of cells for plasmids transfection (genetic engineering) or to facilitate drug delivery [6].

## 5.2 Microfabricated devices for electroporation

In a classical electroporation scheme, in order to have a homogeneous electric field, two parallel planar electrodes are immersed in the cell-containing medium, at a distance going typically from some mm to 1 cm. A large potential difference is then applied between the electrodes, to reach an electric field strength in the order of 1 kV $cm^{-1}$. This type of setup allows a batch of cells to be electroporated. To pass from a batch process to a continuous process, microfluidic electroporation chambers,

where the cell suspension is continuously flowing, have been realized and commercialized [7, 8, 9]. Recently, electroporation has found applications in lab-on-chip devices, to perform in situ cell lysis, followed by intracellular constituents separation and detection [10, 11]. Electroporation is well adapted for *in situ* cell lysis due to its rapidity and the absence of added chemicals.

Targeting of single cells is possible by using microneedles as the electroporation electrodes [12]. The major drawback of this technique is the need to place the needles in the vicinity of every target cell. On the other hand, if a microneedle is replaced by a microcapillary as the electroporation electrode [13], local delivery of chemicals in selected target cells with high spatial resolution is possible. Hybrid systems exist, where microneedle electrodes are combined with microfabricated platforms comprising planar electrodes, where cells are cultured [14]. An automated system allowing local electroporation of adherent cells by scanning of the culture surface with an electroporation microcapillary has been recently presented [15].

Microfabricated electroporation platforms allow single or multiple-site single cell electroporation. As the electroporation site is fixed, the challenge of these systems is to correctly position the target cell. The first chip-based single cell electroporation devices were dedicated to cells in suspension, and were formed by a micro hole in a thin dielectric membrane separating two microfluidic chambers. The pressure difference between the microfluidic chambers will partially trap the cell in the micrometer-size hole, as shown in figure 5.1. Electroporation is performed by electrodes placed in the microfluidic chambers [16]. Since then, all microfabricated single cell electroporation devices are largely based on this same principle [7]. Two microfluidic chambers are separated by a thin dielectric membrane, where a micron-size hole is etched.

Adherent cells were observed to be transfected more efficiently and with a higher cell viability than suspended cells [17]. To maximize the spatial resolution and lower the required applied potential, the cell to be electroporated should be as near as possible to the electroporation electrode.

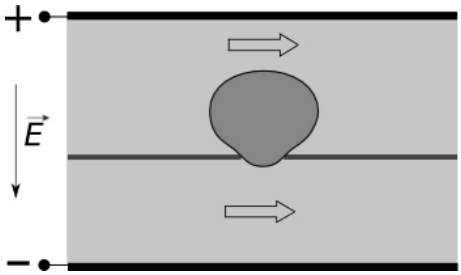


Figure 5.1: Schematic view of the first type of microfabricated electroporation device (adapted from [16]).

When electrodes are submitted to large potential differences, electrolytic reactions take place at the electrode surface. When the electroporation electrodes are not in direct contact with the target cells, toxic products due to electrolytic reactions are not a problem [18]. In contrast, direct contact of the cell culture with the electroporation electrodes can cause cell damage. The electrolysis reactions can be partially reversed by applying bipolar pulses instead of unipolar pulses. The electrolysis itself can be reduced by applying short (in the order of $\mu$s) pulses and by increasing the resistance of the medium between the electroporation electrodes [7]. Despite of this problem, many devices using cells directly cultured on electroporation electrodes have been reported [19, 20, 21, 22, 23, 24]. Recently, to overcome this problem, a porous membrane where cells are cultured has been used as a spacer between the electroporation electrodes and the adherent cells [25, 26]. This approach is similar to the "two-chamber" approach described earlier [16] (figure 5.1). The presence of a porous material between the cell culture and the electroporation electrodes is beneficial in several ways. For example, pores in a non conducting membrane material will act as constrictions, inducing a local rise in the electrical field. This phenomenon lowers the needed voltage and allows the cell patterning and the modulation of the electric field strength as a function of the pores size [26]. To the best of our knowledge, no single cell electroporation devices have been reported using micrometer size patterned electrodes, neither with cells directly grown on their surface nor using a removable porous membrane insert.

## 5.3 Principles of electroporation

Electroporation is a technique using high electric fields to induce a transient permeability increase of the cell membrane. The steps involved in reversible electroporation are [27]:

**The application of electrical pulses** of micro- to millisecond duration. Rest transmembrane potential $\Delta\varphi$ is normally between -50 mV and -100 mV for mammalian cells, the interior of the cell being at a lower potential. When an external electric field is applied, the transmembrane potential is altered. If the electrical field is sufficiently strong to rise the $\Delta\varphi$ to 0.2 V to 1 V, pores will form [18].

**Charging of the cell membrane** due to ionic fluxes.

**Rearrangement of the molecular structure** of the cell membrane.

**Formation of pores** in the nanoscale range [28], filled by water molecules (hydrophilic pores).

**Membrane recovery.** After the removing of the electrical field, pores reseal. This process can take seconds to minutes [29, 30]. After pore resealing, the membrane structural and physiological properties recovery takes a much longer time, in the order of hours. Although pores reseal, cellular alterations can lead to cell death [29].

To date, theoretical models are restricted to descriptions of planar bilayer models and spherical single cells. Experiments have been mainly performed on planar lipid bilayers, cell suspensions and individual cells [27]. Very little is known about the response mechanism of a cell culture, or a whole tissue. For this reason, electroporation remains mostly an empirical technique, and *in vivo* applications are limited [27]. Further information on the theoretical modelling of electroporation can be found in the following articles [27, 29, 30, 31, 32, 33].

## 5.4 Materials and methods

To test the feasibility of on-chip electroporation, first the stability of the platinum thin film electrodes upon the application of series of electrical pulses has been verified, then electroporation tests with on-chip cell cultures have been performed. The ion-selective electrodes sensitivity to electrical shunts, due to the high ion-selective membrane resistivity [34], is a potential problem. The $\mu$ISE array might thus be affected by the strong electrical pulses needed for electroporation, and its functionality after the application of the electroporation protocol had to be tested.

### Chemicals

Potassium hydrogen phosphate of p.a. quality, $MgCl_2$ of Fractopur quality and all the other metal chloride salts of Suprapur quality were from Merck. The ionophores valinomycin, the ionic additive potassium tetrakis[3,5-bis(trifluoromethyl)phenyl]borate (KTFPB), the membrane matrix high molecular weight poly(vinyl chloride) (PVC), the plasticizers bis(2-ethylhexyl) sebacate (DOS) and the membrane solvent cyclohexanone were of Selectophore quality, the pH buffer N-(2-hydroxyethyl)-piperazine-N'-(2-ethanesulfonic acid) (HEPES), BioUltra, for molecular biology, fluorescein sodium salt was of standard quality, for fluorescence, and D(+)-glucose was of BioChemika Ultra quality, all from Fluka. Aqueous solutions were prepared with cleanroom grade deionized water (>20 M$\Omega$ cm specific resistance).
Hanks balanced salt solution (HBSS, without $Ca^{2+}$ and $Mg^{2+}$) was from Bioconcept, trypsin and neonatal calf serum were from Boehringer. Collagen type IV, from human placenta was of BioChemika grade, from Fluka. Pancreatin (4 USP specifications, cell culture tested), medium M199 with Hanks salts, vitamin B12 (99%, cell culture tested), bromodeoxyuridine ($\geq$99%, SigmaUltra grade), L-glutamine ($\geq$99%, meets USP testing specifications, cell culture tested) were all from Sigma. Penicillin and streptomycin were from Seromed Fakola.

### Microfabricated platforms

*On-chip electroporation.*
A glass-based platform comprising 5500 $\mu m^2$ Pt thin film electrodes was microfabricated for the electroporation assays. A glass substrate was chosen for this assay because of its transparency, allowing observations with an inverted microscope. A photograph of the platform and a schematic view of eletroporation electrodes are presented in figure 5.2. The Pt counter electrode was placed by a PDMS spacer at 100 $\mu$m to the chip surface.

a. 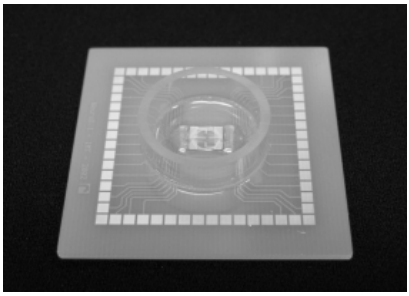 b. 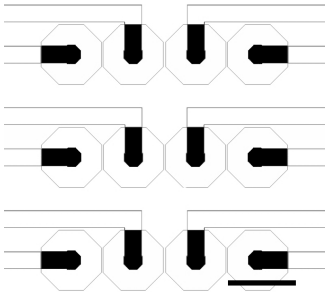

Figure 5.2: a. Photograph of the device used for on-chip electroporation assay. b. Schematic view of a section of the Pt electrode array. The Pt electrodes are marked in black. Scale bar is 200 $\mu$m.

*$\mu$ISE stability assay.*
SQUARE design chips (see chapter 2 and figure 5.3), comprising 5 $\mu$m diameter ion-selective microelectrodes were used. The composition of the ion-selective membrane was the following : 5 wt% valinomycin, 1 wt% KTFPB, 89 wt% DOS, 5 wt% PVC (membrane $K^+$-B, see section 3.3.2). The electrodes were preconditioned during one night in 1 mM KCl prior to the tests.

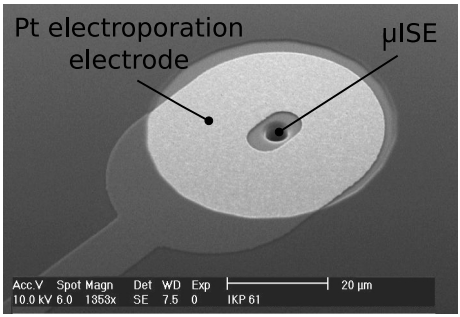


Figure 5.3: SEM photograph of a 3 $\mu$m diameter ion-selective microelectrode surrounded by a 45 $\mu$m diameter Pt thin film microelectrode (light grey area).

### Experimental setup and procedure

*On-chip electroporation.*
The electroporation assay was performed by applying a series of monophasic electroporation pulses of 250 $\mu$s between the on-chip thin film Pt electrodes and a Pt counter electrode placed at 100 $\mu$m from the chip surface.
Prior to the cell electroporation assay, the stability of the Pt thin film electrodes to the electroporation pulses was tested. The quality of the Pt electrodes was tested prior to and after the application of the pulses by cyclic voltammetry in a phosphate buffer solution (pH 7) and by optical inspection. Electric pulse assays were performed in the same phosphate buffer solution. Series of 5 to 50 pulses with an amplitude between 5 V and 80 V were applied.
The cell electroporation assay was performed on rat cardiomyocytes cultured on the surface of the chip. Primary cultures of neonatal rat ventricular cardiomyocytes were obtained using established procedures [35]. Hearts from 4 to 6 neonatal rats (Wistar, 1 to 2 days old) were excised, the ventricles were minced with scissors, and the resulting small tissue pieces were dissociated in Hanks balanced salt solution (HBSS, without $Ca^{2+}$ and $Mg^{2+}$) containing 0.1% trypsin and 60 $\mu$g ml$^{-1}$ pan-

creatin. The dispersed cells were centrifuged and resuspended in medium M199 with Hanks salts. The medium was supplemented with 20 U $ml^{-1}$ penicillin, 20 $\mu$g $ml^{-1}$ streptomycin, 20 $\mu$g $ml^{-1}$ vitamin B12, 100 $\mu$M bromodeoxyuridine, $\mu$g $ml^{-1}$ L-glutamine, and 10% neonatal calf serum. The cell suspension was preplated in a large culture flask and incubated for 2 hours at 35°C in a humidified atmosphere containing 1.2% $CO_2$. This procedure served to enrich the cardiomyocyte fraction.

Prior to cell seeding, the surface of the microfabricated platforms was sterilized by rinsing 5 min with bleach (NaClO + NaCl solution), followed by rinsing with deionized water and ethanol 70%. The glass surface was treated with a solution of collagen (collagen type IV, human placenta, Sigma) for 5 min, followed by rinsing with HBSS and UV sterilization.
The cardiomyocytes were seeded at a density of $1.4{\cdot}10^3$ cells $mm^{-2}$. Medium exchanges were performed on the first day after seeding with supplemented M199 containing a reduced concentration of calf serum (5%) and lacking bromodeoxyuridine.

After 2 days of on-chip culturing, cell cultures were washed three times using a HEPES buffer saline solution (HBS, 21 mM HEPES, 137 mM NaCl, 5 mM KCl, 0.7 mM $Na_2HPO_4$, 6 M glucose, pH 7.5). A solution of HBS + 5 $\mu$M fluorescein was then added, and the electroporation assay was performed at room temperature (20°C). Single electroporation pulses of between 1 V to 10 V were generated by an Agilent 33120A function generator. After the electroporation pulse, 15 min rest time was allowed to pore resealing. The cell culture was washed three times with HBS, to eliminate excess fluorescein [36]. The fluorescein intake was observed with a microscope equipped for epifluorescence (Axiovert 135 M, Zeiss).

*$\mu$ISE stability assay.*
Calibration of the potassium-selective platform with KCl solutions comprising 150 mM NaCl background was performed prior to and after the electroporation pulse assay, to verify the functionality of the electrodes. The electrical pulse assays were performed in a phosphate buffer saline

solution (PBS: 7.7 mM $Na_2HPO_4$, 2.7 mM $NaH_2PO_4$, 154 mM NaCl, pH adjusted to 7.4 with NaOH). Monophasic single electroporation pulses of 250 $\mu$s, 10 V were applied between two adjacent on-chip electroporation electrodes (gap 150 $\mu$m, for a schematic view of the geometry of the electrode array, see figure 2.2). A single pulse and series of 5 and 10 pulses, with 1 s between each pulse, were applied.

## 5.5 Results and discussion

### 5.5.1 On-chip electroporation

The stability of thin film Pt microelectrodes upon pulses up to 40 V was verified by cyclic voltammetry and optical inspection.

The applicability of electroporation to adherent cell cultures was tested with this assay. The effectiveness and the reversibility of the electroporation process were tested by observation of the accelerated intake of fluorescein by the cells. Fluorescein is a hydrophilic fluorescent dye that under normal cell culture conditions penetrates slowly in the cells. Figure 5.4.b-c shows an example of an electroporation test performed with a single square pulse of 250 $\mu$s and 8 V amplitude. These experiments showed that the cells in the immediate vicinity of the electrodes have been exposed to an excessively high electric field, inducing irreversible electroporation, and the subsequent cell lysis (in figure 5.4.a: EP non viable). The cells located further away from the electrodes clearly showed the fluorescein intake, obtained by reversible electroporation (EP viable). Cells located at a larger distance from the electroporation electrodes have not been exposed to a sufficiently high electric field, and thus have not been affected by the electric pulse (viable). The results thus confirm the possibility of using Pt planar microelectrodes for performing the electroporation of cells.

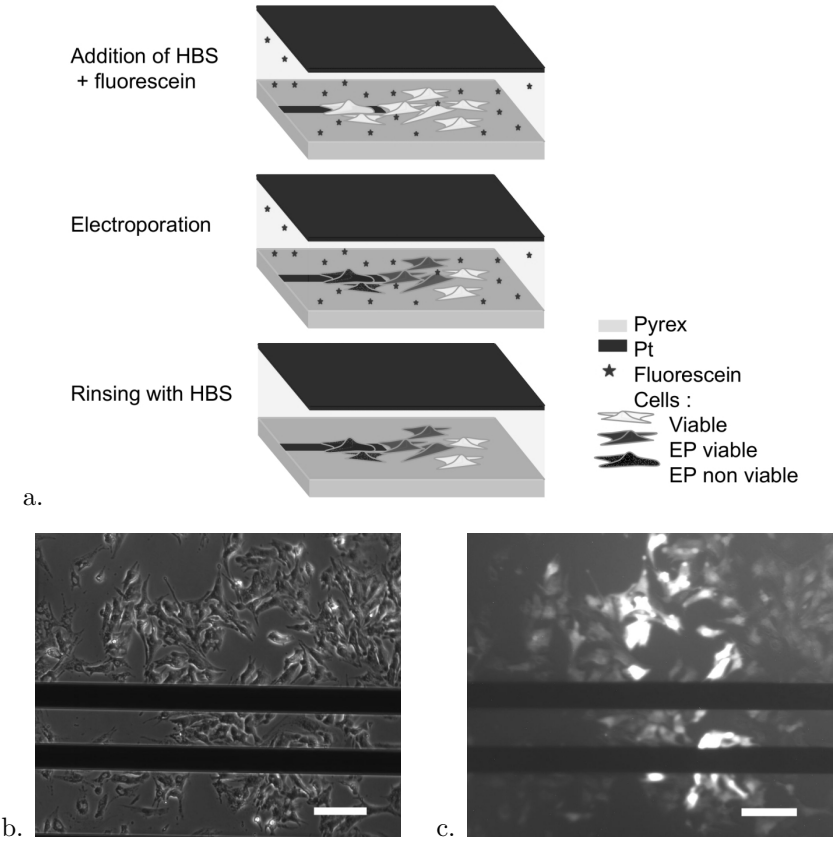


Figure 5.4: Electroporation on cardiomyocytes cultured on-chip. Electroporation (EP) was performed in HBS + 5 $\mu$M fluorescein, with a single monophasic pulse of 250 $\mu$s, 8 V. Gap between the electrodes: 100 $\mu$m. a. Schematic view of the electroporation procedure. After the application of the electroporation pulse, a fraction of the cells is irreversibly electroporated and lysed (EP non viable), a fraction is reversibly electroporated and show an increased fluorescein intake (EP viable), and the remaining are not affected by the electroporation pulse (viable). b. Optical image of the cardiomyocyte culture after electroporation. The cells in the bottom left corner of the image have been lysed, while the others are intact. c. Fluorescence image of the same cells shown in b., showing fluorescein intake of a part of the cells. Scale bars are 100 $\mu$m.

### 5.5.2 $\mu$ISE stability assay

The functionality of the $\mu$ISE array after the application of an electroporation pulse was tested. Based on the results of the on-chip electroporation assay, single monophasic pulses of 10 V, 250 $\mu$s, inducing cellular lysis in the vicinity of the electrodes were applied.

Figure 5.5 illustrates the response of a $K^+$-selective $\mu$ISE prior to and after the application of a series of electrical pulses. After the application of 5 pulses, only a small increase in the detection limit is observed, and after 10 pulses, the $\mu$ISE are still responsive in the high concentration range. Usually, the ion-selective microelectrodes revealed to be strongly affected by the application of a series of 10 pulses: the electrode response was completely lost, and the ion-selective membrane was expelled from the micropipette. Covalent bonding of the membrane with the micropipettes wall could be beneficial for the ISE stability. In contrast, the application of up to 5 pulses affected the electrode response only slightly.

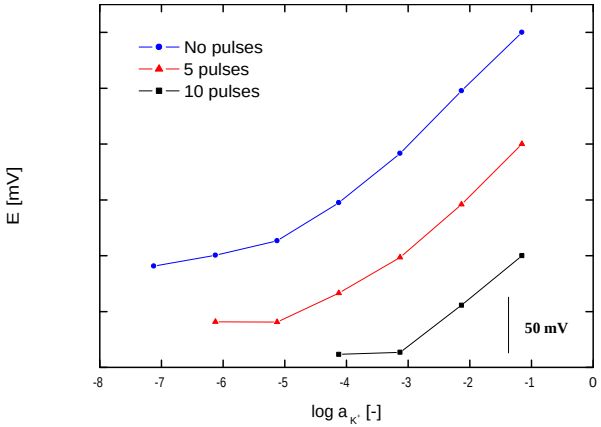


Figure 5.5: Calibration curves of a $K^+$-selective microelectrode recorded prior to and after the application of a series of 5 and 10 single monophasic 10 V, 250 $\mu$s electrical pulses. The curves are offset for the sake of clarity.

It should be stressed that the applied pulse is the upper limit necessary for a complete lysis of a number of cells. For local lysis, pulses of lower amplitude, and a short pulse time will be applied. Lysis of the entire cell population obtained by application of simultaneous pulses from the whole Pt electrode array also needs a weaker pulse amplitude.
The potentiometric signal of the $\mu$ISE array recorded during the application of the pulses did not suffer from drift, potential steps or other artefacts induced by the electroporation pulses.

Reversible local electroporation will need a fine control of the electroporation conditions. Jain et al. have reported an optimal viability after electroporation of adherent cells cultured on 100 $\mu$m square gold microelectrodes (100 $\mu$m interelectrode gap) after pulses of 20 ms (1-8 pulses, 1'sec between pulses) and 3 V amplitude [24]. Figure 5.6 reports results of a simulation of the electric field values in an aqueous solution (conductivity 1.6 $\mu$S, similar to PBS [24]) induced by a difference in potential

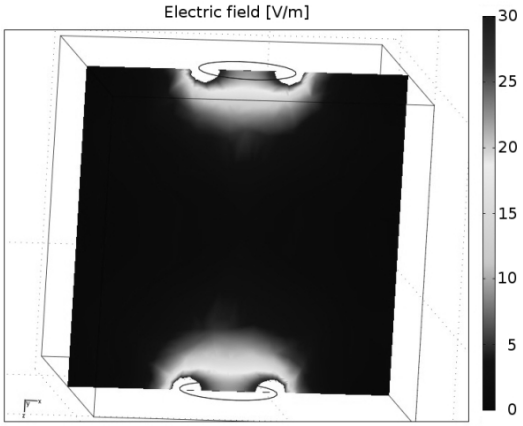


Figure 5.6: Electric field intensity between two 45 $\mu$m diameter Pt electrodes in water (conductivity 1.6 $\mu$S), interelectrode gap: 100 $\mu$m, potential difference: 10 V. Courtesy of L. MacQueen, Polytechnique de Montréal, Canada.

of 10 V between two circular Pt electrodes of 45 $\mu$m diameter divided by a 100 $\mu$m gap. The simulation was performed with the COMSOL Multiphysics software. It can be noticed that the electric field is strong only in the vicinity of the electrodes and decays rapidly in the bulk of the solution. Consequently, to have a very local electroporation, a low pulse amplitude should be sufficient. Obviously, the parameters are dependent on the cell culture type.

## 5.6 Summary

The realization of a combined $\mu$ISE/Pt electrode array has been proven to be feasible. Both irreversible and reversible electroporation of adherent cells, cultured on a microfabricated glass chip have been performed with a single monophasic pulse of 8 V and 250 $\mu$s applied between two Pt electrodes divided by a gap of 100 $\mu$m. It has been shown that such electrical stimuli do not affect the functionality of $\mu$ISE filled with membrane $K^+$-B (see table 3.2). The potentiometric signal starts to degrade after a series of 5 pulses, and in general is lost after 10 pulses. As the electric field strength decays rapidly with the distance from the electrodes surface, a lower pulse amplitude should be sufficient to induce local electroporation. We can thus expect that $\mu$ISE would be less affected.

As the $\mu$ISE can withstand these stimuli, other cell manipulations using electrical forces could be implemented in parallel with $\mu$ISE. An interesting idea to be tested is the feasibility to achieve intracellular measurements by electroporation-assisted impalement. Electrical pulses destabilize the cell membrane, and thus facilitate the cell impalement by a micropipette. Combined mechanical/electroporation microinjection methods have been used to impale liposomes with a 2 $\mu$m diameter glass capillary micropipette, too large to enter the liposome only by mechanical impalement [37].

## 5.7 Epilogue: a $\mu$ISE-patch clamp hybrid platform

Patch clamp is a technique allowing the study of ionic current through the cell membrane [38]. Classical patch clamp uses electrolyte filled glass capillary micropipettes that adhere to the cell membrane, forming a seal. In the whole cell patch clamp configuration, the cell membrane is subsequently opened by suction, allowing the access to intracellular space and the recording of electrical current flowing through the cell membrane. The main issue in patch clamp is the ability to realize a good seal between the patch clamp pipette and the cell membrane. For measurements on transmembrane ion fluxes, the seal resistance must be greater than 1 G$\Omega$. Good results are obtained with glass micropipettes, but the seal is of a less good quality when using silicon-based materials or plastics, as well as when the geometry of the patch clamp aperture is planar [39]. The quality of the seal decays rapidly with the increase of the patch clamp apertures [40], especially for apertures above 5 $\mu$m. The success rate of the seal varies widely, going from 75% (60% guaranteed by the producer) for the coated glass biochips offered by Aviva Biosciences [39, 41], to 24% for the PDMS devices of Sigworth′s group [42].

### 5.7.1 Implementation of a patch clamp microchannel on the $\mu$ISE platform

In our micropipette-based $\mu$ISE design, the micropipette could in theory be coupled to a microfluidic channel, in a similar design as the one used by the "Cytocentering" chip [43, 44], schematically shown in figure 5.7. The outer aperture, of 10 $\mu$m diameter is used to trap the cell, the smaller channel is used as the patch pipette. In our case, as shown in figure 5.7, the pipette would have been filled with IS-membrane and the outer aperture used for both cell trapping and patch clamp.

To adapt a geometry similar to the one presented in figure 5.7 to a combined $\mu$ISE-patch clamp platform, an array of micron size channels, combined with openings for cell positioning and opening of 5 $\mu$m to 10 $\mu$m diameter, and internal electrodes, to monitor the seal resistance,

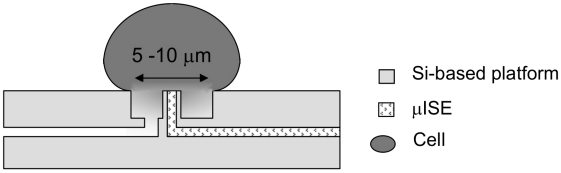


Figure 5.7: Schematic view of a coupled $\mu$ISE-patch clamp platform.

has to be implemented. To date, an established technology allowing the direct on wafer patterning of micron size open channels is not available. An interesting approach based on non standard multidirectional photolithography has been proposed by Suzuki et al. [45, 46]. The process is based on SU-8 processing with backside exposure through a glass substrate. The substrate is exposed twice with different incident angles, as illustrated in figure 5.8. The incidence angle of the UV light and the width of the Al photomask can be varied to fabricate closed channels or holes. Moreover, the Al (or other metal) photomask could be used as an internal patch clamp electrode.

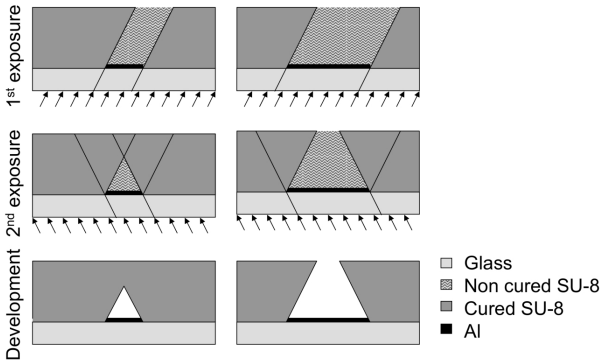


Figure 5.8: Microchannels and apertures fabrication process by multidirectional photolithography. Adapted from [45].

As the realization of the patch clamp channel array would require a long development, a solution for the use of patch clamp in combination with the ionic measurements would be to use the silicon-based micropipettes for both patch clamp and potentiometry. A similar study, where double barreled glass capillary $\mu$ISE have been used as patch clamp pipettes has been published several years ago [47]. Although possibilities of having patch clamp and $\mu$ISE measurements without the need of a modification of the platform are interesting, their feasibility has not been verified.

### 5.7.2 The perforated patch technique

Amphotericin B is an antifungal drug that has been observed to lead to $K^+$ efflux when brought in contact with the cell membrane. A modified ion-selective membrane containing amphotericin B has been prepared to test the interference of this compound with the IS-membrane functionality.

The cross-sectional area of amphotericin B channels has been reported to be 0.5 $nm^2$ [48]. Successful perforated patch experiments have required the presence of pores on 0.16% of the total patch area [48]. For the preparation of the modified ion-selective membrane cocktail, we assumed that 1% of the amphotericin B molecules present in the silicon nitride micropipette would migrate in the cell membrane, and form pores. In this case, to obtain pores on 0.16% of the area in contact with a 1.5 $\mu$m diameter, 50 $\mu$m long micropipette, the formation of 5'600 pores is necessary. This corresponds to an amphotericin B concentration in the IS-membrane of $1.05 \cdot 10^{-5}$ M.
Amhotericin B (Vetranal analytical standard, Riedel -de Haën) is dissolved in N,N-dimethylformamide (DMF; 99.8%, ACS reagent, from Aldrich) to a concentration of $3.41 \cdot 10^{-3}$ M. Subsequently, the DMF solution is diluted in cyclohexanone on a ratio 1:99, and 15.4 $\mu$l of this new cyclohexanone solution are added to 150 $\mu$l of the $K^+$-B IS-membrane cocktail (see table 3.2 for composition).

We observed that the addition of $5{\cdot}10^{-5}$ M amphotericin B to the potassium-selective membrane $K^+$-B does not influence the response of the electrodes in calibration solutions.

### 5.7.3 Implementation of other functionalities on the $\mu$ISE platform

The geometry of the planar SQUARE platform has been designed to facilitate further implementation of other functionalities, in parallel with the ion-selective microelectrode array. The planar design allows the microstructuring of the surface, and the large surface of the chip, 18x20 $mm^2$, allows to adapt the size of the fluidic cell culture chamber according to the needs of the cell culture in use. The realized platform is flexible to the completion by other functionalities, and thus enlarges the possibilities of adaptation for specific applications.

# Bibliography

[1] Sims CE and Allbritton N. Analysis of single mammalian cells on-chip. *Lab Chip*, 7:423–440, 2007.

[2] El-Ali J, Sorger PK, and Jensen KF. Cells on chip. *Nature*, 442:403–411, 2006.

[3] Byrne CM and Thompson JF. Role of electrochemotherapy in the treatment of metastatic melanoma and other metastatic and primary skin tumors. *Exp. Rev. Anticancer Ther.*, 6:671–678, 2006.

[4] Voldman J. Electrical forces for microscale cell manipulation. *Annu. Rev. Biomed. Eng.*, 8:425–454, 2006.

[5] Morin FO, Takamura Y, and Tamiya E. Investigating neuronal activity with planar microelectrode arrays: achievements and new perspectives. *J. Biosci. Bioeng.*, 100:131–143, 2005.

[6] Gehl J. Electroporation: theory and methods, perspectives for drug delivery, gene therapy and research. *Acta Physiol. Scand.*, 177:437–447, 2003.

[7] Fox MB, Esveld DC, Valero A, Luttge R, Mastwijk HC, Bartels PV, van den Berg A, and Boom RM. Electroporation of cells in microfluidic devices: a review. *Anal. Bioanal. Chem.*, 385:474–485, 2006.

[8] Shin YS, Cho K, Kim JK, Lim SH, Park CH, Lee KB, Park Y, Chung C, Han D-C, and Chang JK. Electrotransfection of mammalian cells using microchannel-type electroporation chip. *Anal. Chem.*, 76:7045–7052, 2004.

[9] Lu KY, Wo AM, Lo YJ, Chen KC, Lin CM, and Yang CR. Three dimensional electrode array for cell lysis via electroporation. *Biosens. Bioel.*, 22:568–574, 2006.

[10] McClain MA, Culbertson CT, Jacobson SC, Allbritton NL, Sims CE, and Ramsey JM. Microfluidic devices for the high-throughput chemical analysis of cells. *Anal. Chem.*, 75:5646–5655, 2003.

[11] Gao J, Yin XF, and Fang ZL. Integration of single cell injection, cell lysis, separation and detection of intracellular constituents on a microfluidic chip. *Lab Chip*, 4:47–52, 2004.

[12] Lundqvist JA, Sahlin FA, Aberg MAI, Strömberg A, Eriksson PS, and Orwar O. Altering the biochemical state of individual cultured cells and organelles with ultramicroelectrodes. *Proc. Natl. Acad. Sci.*, 95:10356–10360, 1998.

[13] Nolkrantz K, Farre C, Brederlau A, Karlsson RID, Brennan C, Eriksson PS, Weber SG, Sandberg M, and Orwar O. Electroporation of single cells and tissues with an electrolyte-filled capillary. *Anal. Chem.*, 73:4469–4477, 2001.

[14] Han F, Wang Y, Sims CE, Bachman M, Chang R, Li GP, and Allbritton NL. Fast electrical lysis of cells for capillary electrophoresis. *Anal. Chem.*, 75:3688–3696, 2003.

[15] Oloffson J, Levin M, Stromberg A, Weber SG, Ryttsen F, and Orwar O. Scanning electroporation of selected areas of adherent cell cultures. *Anal Chem.*, 79:4410–4418, 2007.

[16] Huang Y and Rubinski B. Micro-electroporation: improving the efficiency and understanding of electrical permeabilization of cells. *Biomed. Microdev.*, 2:145–150, 1999.

[17] Zheng Q and Chang DC. High efficiency gene transfection by in situ electroporation of cultured cells. *Biochim. Biophys. Acta*, 1088:104–110, 1991.

[18] Oloffson J, Nolkrantz K, Ryttsén Lambie BA, Weber SG, and Orwar O. Single-cell electroporation. *Curr. Opinion Biotechnol.*, 14:29–34, 2003.

[19] Yamauchi F, Kato K, and Iwata H. Spatially and temporally controlled gene transfer by electroporation into adherent cells on plasmid DNA-loaded electrodes. *Nucl. Acids Res.*, 32:e187, 2004.

[20] Lin YC, Li M, Fan CS, and Wu LW. A microchip for electroporation of primary endothelial cells. *Sens. Actuators A*, 108:12–19, 2003.

[21] He H, Chang DC, and Lee YK. Using a micro electroporation chip to determine the optimal physical parameters in the uptake of biomolecules in HeLa cells. *Bioelectrochem.*, 70:363–368, 2007.

[22] Kieswetter L, Zhang JM, Houdeau D, and Steckenborn A. Determination of Young's moduli of micromechanical thin film using resonance method. *Sens. Actuators A*, 35:153–159, 1992.

[23] Johnson L, Scribner D, and Pancrazio J. Microelectronic cell electroporation array. Patent, 2005. no. 20050070018.

[24] Jain T and Muthuswamy J. Microsystem for transfection of exogenous molecules with spatio-temporal control into adherent cells. *Biosens. Bioel.*, 22:863–870, 2007.

[25] Müller EKJ, Horbaschek M, Lucas K, Zimmermann U, and Sukhorukov VL. Electrotransfection of anchorage-dependent mammalian cells. *Exp. Cell Res.*, 288:344–353, 2003.

[26] Ishibashi T, Takoh K, Kaji H, Abe T, and Nishizawa M. A porous membrane-based culture substrate for localized in situ electroporation of adherent mammalian cells. *Sens. Actuators B*, 128:5–11, 2007.

[27] Chen C, Syme SW, Robinson MP, and Evans JA. Membrane electroporation theories: a review. *Med. Biol. Eng. Comput.*, 44:5–14, 2006.

[28] Tieleman DP. The molecular basis of electroporation. *BMC Biochem.*, 5, 2004. http://www.biomedcentral.com/1471-2091/5/10.

[29] Teissie J, Golzio M, and Rols MP. Mechanisms of cell membrane electropermeabilization: a minireview of our present (lack of ?) knowledge. *Biochim. Biphys. Acta*, 1724:270–280, 2005.

[30] DeBruin KA and Krassowska W. Modeling electroporation in a single cell: I. Effects of field strength and rest potential. *Biophys. J.*, 77:1213–1224, 1999.

[31] Weaver JC and Chizmadzhev YA. Theory of electroporation: a review. *Bioelectrochem. Bioenerg.*, 41:135–160, 1996.

[32] DeBruin KA and Krassowska W. Modeling electroporation in a single cell: II. Effects of ionic concentrations. *Biophys. J.*, 77:1225–1233, 1999.

[33] Bilska AO, DeBruin KA, and Krassowska W. Theoretical modeling of the effects of shock duration, frequency, and strength on the degree of electroporation. *Bioelectrochem.*, 51:133–143, 2000.

[34] Ammann D. *Ion-selective microelectrodes, principles, design and application.* Springer-Verlag, 1986. ISBN 0-387-16222-4.

[35] Rohr S, Flückiger-Labrada R, and Kucera J. Photolitographically defined deposition of attachment factors as a versatile method for patterning the growth of different cell types in culture. *Eur. J. Physiol.*, 446:125–132, 2003.

[36] Wu JC, Tsai RY, and Chung TH. Role of catenins in the development of gap junctions in rat cardiomyocytes. *J. Cell. Biochem.*, 88:823–835, 2003.

[37] Karlsson M, Nolkrantz K, Davidson MJ, Strömberg A, Ryttsén F, Åkerman B, and Orwar O. Electroinjection of colloid particles and biopolymers into single unilamellar liposomes and cells for bioanalytical applications. *Anal. Chem.*, 72:5857–5862, 2000.

[38] Neher E. *Ion channels for communication between and within cells*, pages 10–25. Nobel Lectures, Physiology or Medicine 1991-1995. World Scientific Publishing Co., 1997.

[39] Sigworth FJ and Klemic KG. Microchip technology in ion-channel research. *IEEE Trans. Nanobiosci.*, 4:121–127, 2005.

[40] Lehnert T, Gijs MAM, Netzer R, and Bischoff U. Realization of hollow $SiO_2$ micronozzles for electrical measurements on living cells. *Appl. Phys. Lett.*, 81:5063–5065, 2002.

[41] http://avivabio.com.

[42] Li X, Klemic KG, Reed MA, and Sigworth FJ. Microfluidic system for planar patch clamp electrode arrays. *Nano Lett.*, 6:815–819, 2006.

[43] Stett A, Burkhardt C, Weber U, van Stiphout P, and Knott T. Cytocentering: a novel technique enabling automated cell-by-cell patch clamping with the CytoPatch$^{TM}$ chip. *Receptors Channels*, 9:59–66, 2003.

[44] http://www.cytocentrics.com.

[45] Suzuki T, Tokuda T, Fujiwara N, Yamamoto H, Kanno I, Washizu M, and Kotera H. Single-mask fabrication process for high aspect-ratio embedded microchannels with openings. *9$^{th}$ Intl. Conf. Miniaturized Systems for Chemistry and Life Science, μTAS, Boston, USA*, 2:1183–1185, 2005.

[46] Suzuki T, Yamamoto H, Ohoka M, Kanno I, Washizu M, and Kotera H. A low-damage cell trapping array fabricated by single mask multidirectional photolithography with equivalent circuit analysis. *11$^{th}$ Intl. Conf. Miniaturized Systems for Chemistry and Life Science, μTAS, Paris, France*, 2:1765–1767, 2007.

[47] Thomas RC, Pagnotta SE, and Nistri A. Whole-cell recording of intracellular pH with silanized and oiled patch-type single or double-barreled microelectrodes. *Pflügers Arch. - Eur. J. Physiol.*, 447:259–265, 2003.

[48] Rae J, Cooper K, Gates, and P Watsky M. Low access perforated patch recordings using amphotericin B. *J. Neurosci. Methods*, 37:15–26, 1991.

# Chapter 6

# Conclusion

In the course of this work, several platforms based on microfabricated ion-selective microelectrode ($\mu$ISE) arrays were realized and validated for recordings of $K^+$ and $Ca^+$ activities in cell cultures. While two platforms comprise an array of protruding micropipette electrodes, planar $\mu$ISE electrodes were implemented on the third one. The platform allows parallel measurements on 16 completely independent electrodes of 1.5 $\mu$m to 6 $\mu$m diameter with an interelectrode gap of 150 $\mu$m or 300 $\mu$m. The detection limits of pK 5.8 and pCa 9 were achieved in background solutions with cellular concentrations of interfering ions, which makes the platforms suitable for investigations for both intra- and extracellular concentration ranges.

In order to assess the performance of the platforms in biological assays, a $K^+$-selective microelectrode array was used for monitoring the release of intracellular potassium upon cell lysis. Kidney cell lysis was induced by a hypo-osmotic shock inducing a mechanism of cell volume regulation wich relies on cellular $K^+$ efflux. Since this mechanism is similar to what is observed in apoptotic cells, this test is of large interest for both fundamental and applied (for example toxicity) investigations on cellular physiology.
A detection limit of 200 cells was achieved. This detection limit is essen-

tially determined by the current setup geometry: with a partial redesign of the cell culture microwell, the detection of a single cell can be envisaged. It was also shown, that the presence of cells and cell debris did not seem to interfere with the $K^+$ sensors or to induce a degradation of the sensor signal, allowing thus multiple uses of the platform.

In a further step, the $\mu$ISE arrays were integrated with Pt microelectrodes. This hybrid $\mu$ISE-Pt array allows in parallel to ionic activity measurements, electrical manipulation of cells. The first application of this $\mu$ISE-Pt hybrid platform was for *in situ* electroporation. The electroporation of cardiomyocytes was confirmed by fluorescence imaging. Importantly, these electroporation tests showed that $\mu$ISE maintained their functionality upon application of up to five pulses of 8 V.

The microelectrode array approach opens new horizons in physiological research, in particular the possibility to perform multiple local and spatially defined measurements of ionic activities in a cell culture, and thus gain information on the cellular network physiology. The flexibility of the developed technology allows further implementation of additional functionalities to yield a complete cell analysis system for fundamental and applied cellular physiology.

# Appendix A

# Symbols and abbreviations

**Symbols**

$a_X$: activity of ion X [M]
$c_X$: concentration of ion X [M]
$E$: potential difference, EMF [V]
$\vec{E}$: electric field [V $m^{-1}$]
F: Faraday constant: 96 485 C $mol^{-1}$
I: primary ion
$I$: ionic strength
J: interfering ion(s)
$K_{IJ}^{pot}$: potentiometric selectivity coefficient
$p_{IJ}$: highest tolerable measurement error of $a_I$ [%] (see eq. 3.12 )
pX := -$\log_{10}$ $a_X$
R: gas constant: 8.314 J $K^{-1}$ $mol^{-1}$
T: temperature [K]
$z_X$: charge number of the ion X
$\Delta\varphi$: cell transmembrane potential [mV]
$\gamma_X$: activity coefficient of the ion X
$\mu$: micro-, ($10^{-6}$)

### Abbreviations

| | |
|---|---|
| BHF: | buffered hydrofluoric acid |
| DL: | detection limit |
| DMEM: | Dulbecco's modified Eagle's medium |
| DMF: | N,N-dimethylformamide |
| DMNB: | 2,3-dimethyl nitrobenzene |
| DOS: | bis(2-ethylhexyl) sebacate |
| DRIE: | deep reactive ion etching |
| EGTA: | ethylene glycol o-o'-bis(2-aminoethyl)-N,N,N'-N'-tetra-acetic acid, calcium buffer |
| ETH 129: | N-N-N'-N'-tetracyclohexyl-3-oxapentanediamide |
| ETH 500: | tetradodecylammonium tetrakis(4-chlorophenyl)borate |
| FBS: | foetal bovine serum |
| HBS: | HEPES buffered saline |
| HBSS: | Hank's balanced salts solution |
| HEPES: | N-(2-hydroxyethyl)piperazine-N'-(2-ethanesulfonic acid), pH buffer, range 6.8-8.2 |
| HF: | hydrofluoric acid |
| HMDS: | hexamethyldisilazane |
| IKP: | ("Institut für Klinische Pharmakologie"), is the name of a microfabricated ion-selective platform comprising an array protruding microelectrodes, located in a 360 $\mu$m deep, 2x2 mm$^2$ square recess |
| IS: | ion-selective |
| ISE: | ion-selective electrodes |
| KOH: | potassium hydroxyde |
| KTClPB: | potassium tetrakis(4-chlorophenyl)borate |
| KTFPB: | potassium tetrakis[3,5-bis(trifluoromethyl)phenyl]borate |
| LPCVD: | low pressure chemical vapor deposition |
| MGH: | ("Massachussetts General Hospital"), is the name of a microfabricated ion-selective platform comprising an array protruding microelectrodes, located in a 360 $\mu$m deep, channel-based recess |
| o-NPOE: | 2-nitrophenyl octyl ether |
| PBS: | phosphate buffered saline |

**Abbreviations - continued**

| | |
|---|---|
| RE: | reference electrode |
| RIE: | reactive ion etching |
| SQUARE: | is the name of a microfabricated hybrid non protruding $\mu$ISE-Pt combined platform |

# Appendix B

# Fabrication processes

## B.1 IKP design

Wafer Si 390 $\mu$m thick, double side polished
Standard cleaning
Photolithography back side DRIE (micropipettes cavities opening).
Surface preparation: dehydration 30"@200°C, HMDS surface silanization
Spinning: AZ1518, 500 rpm (3"), 3000 rpm (40"), 1' hotplate @100°C
Exposition: 55 mJ $cm^2$, low vacuum contact mode. Mask cleaning every 2-3 exposures.
Development: 1', AZ351:water 1:4
Plasma $O_2$, 4'
Postbake 180' @85°C

1. DRIE etching 30 to 50 $\mu$m depth
   Photoresist stripping, plasma $O_2$, 100°C, 30'
   Standard cleaning
2. Thermal wet oxidation, 1100°C, thickness depends on the desired final micropipette diameter

3. LPCVD low stress silicon nitride deposition, 300 nm
   Photolithography top side (KOH opening).
   Surface preparation: dehydration 30" @200°C, HMDS surface silanization
   Spinning: AZ1518, 500 rpm (3"), 3000 rpm (40"), 1' hotplate @100°C
   Exposition: 55 mJ $cm^2$, low vacuum contact mode. Mask cleaning every 2-3 exposures.
   Development: 1', AZ351:water 1:4
   Postbake 35' @125°C
4. RIE opening of silicon nitride and silicon dioxide
   Photoresist stripping, plasma $O_2$, 100°C, 30'
5. KOH wet etch, 40% KOH, 60°C
6. BHF wet etch (BHF 7:1): etch of the oxide at the surface of the protruding micropipettes
7. RIE opening of the silicon nitride micropipettes
   Standard cleaning
8. Thermal wet oxidation, 1100°C, 200 nm
   Photolithography lift off (Pt ISE internal electrodes).
   Surface preparation: dehydration 30" @200°C, NO HMDS !
   Support for spinning: gelpack gel-film$^{TM}$, retention level X0 (see: www.gelpak.com)
   Spinning: LOR 3B, 500 rpm (10") dynamic photoresist dispensing, 4000 rpm (40"), 5' hotplate @190°C
   Spinning: S1813, 1000 rpm (3"), 5500 rpm (40"), 1' hotplate @115°C. Mask cleaning after each exposure.
   Exposition: 45 mJ $cm^2$, low vacuum contact mode
   Development: AZ400:water, three-steps development: 1:4, 44", very poor agitation; 1:4, 8", gentle agitation, 1:8, 8", gentle agitation; change the development baths every 3 wafers.
   Plasma $O_2$, 2'
9. Metal evaporation: 20 nm Ta + 120 nm Pt.
   Photoresist stripping: PG remover, 2 baths @60°C, 30' in the first bath, 60' in the second bath, MOS isopropanol, water, 2x semitool.
   Dicing
   Surface cleaning: $H_2SO_4$ 96% + $H_2O_2$ 30%, 10', immediately before anodic bonding
   Anodic bonding, 4', 1200 V

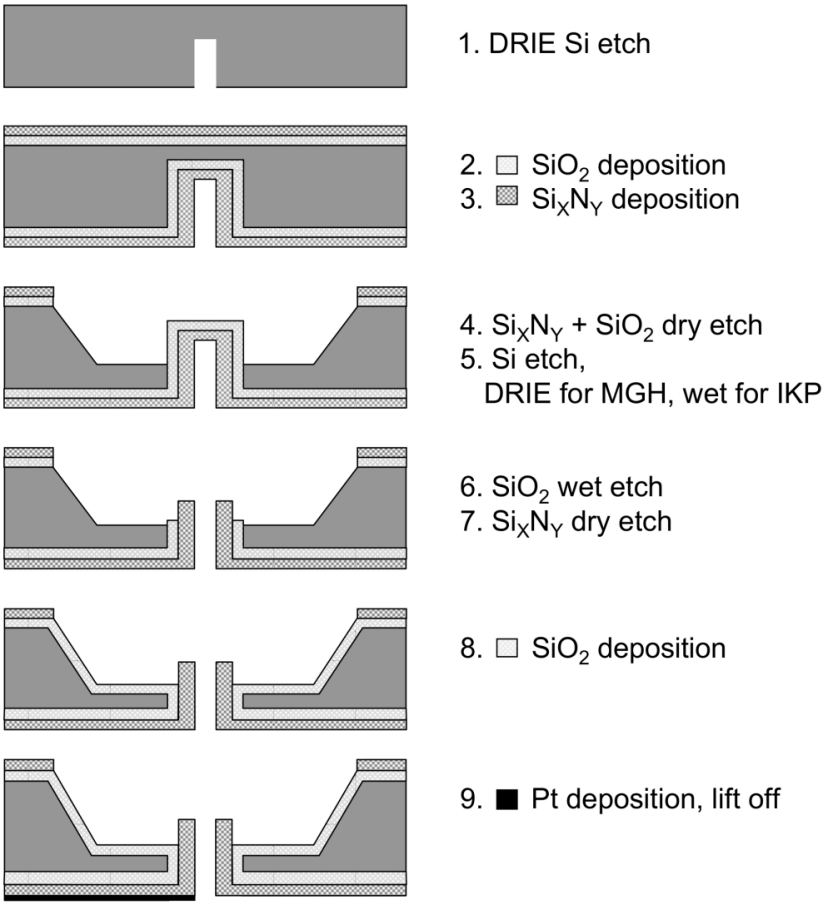


Figure B.1: IKP and MGH designs fabrication process.

## B.2 MGH design

Wafer Si 390 $\mu$m thick, double side polished
Standard cleaning
Photolithography back side DRIE (micropipettes cavities opening).
Surface preparation: dehydration 30" @200°C, HMDS surface silanization
Spinning: AZ1518, 500 rpm (3"), 3000 rpm (40"), 1' hotplate @100°C
Exposition: 55 mJ cm$^2$, low vacuum contact mode. Mask cleaning every 2-3 exposures.
Development: 1', AZ351:water 1:4
Plasma $O_2$, 4'
Postbake 180' @85°C

1. DRIE etching 30 to 50 $\mu$m depth
   Photoresist stripping, plasma $O_2$, 100°C, 30'
   Standard cleaning
2. Thermal wet oxidation, 1100°C, 800 nm
3. LPCVD low stress silicon nitride deposition, 800°C, 300 nm
   Photolithography top side DRIE (multichannel design opening).
   Surface preparation: dehydration 30" @200°C, HMDS surface silanization
   Spinning: AZ4562, 500 rpm (10"), 2000 rpm (40"), 10' hotplate @100°C
   Exposition: 3 x 45 mJ cm$^2$, low vacuum contact mode. Mask cleaning every 2-3 exposures.
   Development: 4', AZ351:water 1:3
   Postbake 900' @70°C
4. RIE opening of low stress silicon nitride and silicon dioxide
5. DRIE etching 350 $\mu$m depth
   Photoresist stripping, plasma $O_2$, 100°C, 30'
6. BHF wet etch (BHF 7:1): etch of the oxide at the surface of the protruding micropipettes
7. RIE opening of the silicon nitride micropipettes
   Standard cleaning

8. Thermal wet oxidation, 1100°C, 200 nm
   Photolithography lift off (Pt ISE internal electrodes).
   Surface preparation: dehydration 30" @200°C, NO HMDS !
   Support for spinning: gelpack gel-film$^{TM}$, retention level X0 (see: www.gelpak.com)
   Spinning: LOR 3B, 500 rpm (10") dynamic photoresist dispensing, 4000 rpm (40"), 5' hotplate @190°C
   Spinning: S1813, 1000 rpm (3"), 5500 rpm (40"), 1' hotplate @115°C. Mask cleaning after each exposure.
   Exposition: 45 mJ cm$^2$, low vacuum contact mode
   Development: AZ400:water, three-steps development: 1:4, 44", very poor agitation; 1:4, 8", gentle agitation, 1:8, 8", gentle agitation; change the development baths every 3 wafers.
   Plasma $O_2$, 2'
9. Metal evaporation: 20 nm Ta + 120 nm Pt.
   Photoresist stripping: PG remover, 2 baths @60°C, 30' in the first bath, 60' in the second bath, MOS isopropanol, water, 2x semitool.
   Dicing, fill the cavities with AZ1518 photoresist to protect the thin silicon membrane during the dicing.
   Photoresist stripping: acetone + isopropanol + water.
   Surface cleaning: $H_2SO_4$ 96% + $H_2O_2$ 30%, 10', immediately before anodic bonding
   Anodic bonding, 4', 1200 V

## B.3 SQUARE design

Wafer Si 390 $\mu$m thick, double side polished
Standard cleaning
Photolithography back side DRIE (microelectrodes cavities, 3-5 $\mu$m diameter).
Surface preparation: dehydration 30" @200°C, HMDS surface silanization
Spinning: AZ1518, 500 rpm (3"), 3000rpm (40"), 1' hotplate @100°C
Exposition: 55 mJ cm$^2$, low vacuum contact mode. Mask cleaning every 2-3 exposures.
Development: 1', AZ351:water 1:4
Plasma $O_2$, 4'
Postbake 180' @85°C

1. DRIE etching 50 $\mu$m depth
   Photoresist stripping, plasma $O_2$, 100°C, 30'
   Standard cleaning
2. Thermal wet oxidation, 1100°C, at least 1 $\mu$m
   Photolithography top side DRIE (microelectrodes cavities, 45 $\mu$m diameter).
   Surface preparation: dehydration 30" @200°C, HMDS surface silanization
   Spinning: AZ4562, 500 rpm (10"), 2000 rpm (40"), 10' hotplate @100°C
   Exposition: 3 x 45 mJ cm$^2$, low vacuum contact mode. Mask cleaning every 2-3 exposures.
   Development: 4', AZ351:water 1:3
   Postbake 900' @70°C
   RIE opening of silicon dioxide
3. DRIE etching 350 $\mu$m depth
   Photoresist stripping, plasma $O_2$, 100°C, 30'
   Surface cleaning: $H_2SO_4$ 96% + $H_2O_2$ 30%, dehydration 15' @ 200°C
4. HF vapour (50% HF) etch, 40°C, 210' at the back side + 90' at the top side.
   Standard cleaning

5. Thermal wet oxidation, 1100°C, thickness depends on the desired final micropipette diameter
   RIE backside etch, thinning of silicon dioxide to 200 nm
   Photolithography lift off (Pt metallic electrodes, wafer top side).
   Surface preparation : dehydration 30" @200°C, NO HMDS !
   Support for spinning: gelpack gel-film$^{TM}$, retention level X0 (see: www.gelpak.com)
   Spinning : LOR 3B, 500 rpm (10") dynamic photoresist dispensing, 4000 rpm (40"), 5' hotplate @190°C
   Spinning : S1813, 1000 rpm (3"), 5500 rpm (40"), 1' hotplate @115°C. Mask cleaning after each exposure.
   Exposition: 45 mJ cm$^2$, low vacuum contact mode
   Development: AZ400:water, three-steps development: 1:4, 44", very poor agitation; 1:4, 8", gentle agitation, 1:8, 8", gentle agitation; change the development baths every 3 wafers.
   Plasma $O_2$ 2'
6. Metal evaporation: 20 nm Ta + 120 nm Pt.
   Photoresist stripping: PG remover, 2 baths @60$^{<circ}$, 30' in the first bath, 60' in the second bath, MOS isopropanol, water, 2x semitool.
7. LPCVD low stress silicon nitride deposition, 800°C, 300 nm
   Photolithography passivation opening (Pt metallic electrodes, wafer top side).
   Surface preparation: dehydration 30' '@200°C, HMDS surface silanization
   Spinning: AZ1518, 500 rpm (3"), 3000 rpm (40"), 1' hotplate @100°C
   Exposition: 55 mJ cm$^2$, low vacuum contact mode.
   Development: 1', AZ351:water 1:4
   Plasma $O_2$, 4'
   Postbake 30' @125°C
   RIE opening of low stress silicon nitride
   Photoresist stripping, plasma $O_2$, 100°C, 30'

Photolithography lift off (Pt ISE internal electrodes, wafer back side).
Surface preparation: dehydration 30"@200°C, NO HMDS !
Support for spinning: gelpack gel-film$^{TM}$, retention level X0 (see: www.gelpak.com)
Spinning: LOR 3B, 500 rpm (10") dynamic photoresist dispensing, 4000 rpm (40"), 5' hotplate @190°C
Spinning: S1813, 1000 rpm (3"), 5500 rpm (40"), 1' hotplate @115°C. Mask cleaning after each exposure.
Exposition: 45 mJ cm$^2$, low vacuum contact mode
Development: AZ400:water, three-steps development: 1:4, 44", very poor agitation; 1:4, 8", gentle agitation, 1:8, 8", gentle agitation; change the development baths every 3 wafers.
Plasma $O_2$, 2'

8. Metal evaporation: 20 nm Ta + 120 nm Pt.
Photoresist stripping: PG remover, 2 baths @60°, 30' in the first bath, 60' in the second bath, MOS isopropanol, water, 2x semitool.
Dicing
Surface cleaning: $H_2SO_4$ 96% + $H_2O_2$ 30%, 10', immediately before anodic bonding
Anodic bonding, 4', 1200 V

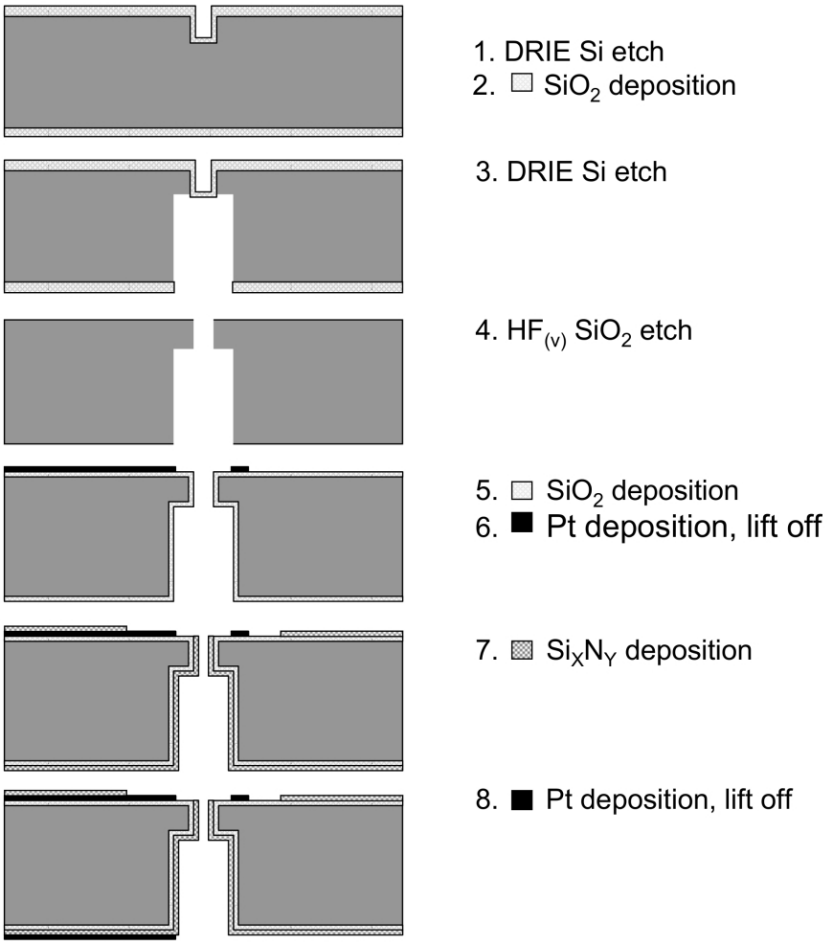


Figure B.2: SQUARE design fabrication process.

## B.4 Pyrex microchannels

Wafer Pyrex, 500 or 1000 $\mu$m thick, drilled, grid 3 mm x 4 mm, 1 mm diameter holes
Standard cleaning
LPCVD polysilicon deposition, 560°C, 2 x 200 nm
Photolithography microchannels.
Surface preparation: dehydration 30" @200°C, HMDS surface silanization
Support for spinning: non-drilled wafer, fixed with double sided tape
Spinning: AZ4562, dispensing on the entire surface, 500 rpm (3"), 1200 rpm (40"), 10' hotplate @100°C
Exposition: 5 x 36 mJ $cm^2$, low vacuum contact mode.
Development: 4', AZ351:water 1:3
Postbake 30' @125°C
RIE opening of polysilicon
Photoresist stripping: acetone + isopropanol + water
HF 20% Pyrex wet etch, 20 $\mu$m
Polysilicon mask stripping: KOH 40%, 60°C
Dicing
Surface cleaning: $HNO_3$, fuming, 30', immediately before anodic bonding
Anodic bonding, 4', 1200 V

# Appendix C

# $Ca^{2+}$ buffer solutions

The calibration solutions have different primary ion concentrations and a fixed interfering ion background. In all solution a background of 50 mM $K^+$ is present, coming from the EGTA salt. The pH was adjusted by HCl titration. All the calculations have been performed for a temperature of 25°C.

Table C.1: $Ca^{2+}$ + 150 mM $K^+$, 5 mM EGTA, 5 mM HEPES, I=0.218 N.

| -log $c_{Ca^{2+},free}$ | Total $c_{Ca^{2+}}$ [M] | pH |
|---|---|---|
| 4 | $5.10 \cdot 10^{-3}$ | 7.4 |
| 5 | $4.97 \cdot 10^{-3}$ | 7.4 |
| 6 | $4.67 \cdot 10^{-3}$ | 7.4 |
| 6.5 | $4.07 \cdot 10^{-3}$ | 7.4 |
| 7 | $2.91 \cdot 10^{-3}$ | 7.4 |
| 7.5 | $1.52 \cdot 10^{-3}$ | 7.4 |
| 7.6 | $1.29 \cdot 10^{-3}$ | 7.4 |
| 8.5 | $1.91 \cdot 10^{-3}$ | 8.0 |
| 9 | $2.48 \cdot 10^{-3}$ | 8.4 |
| 10 | $1.98 \cdot 10^{-3}$ | 9.0 |

Table C.2: $Ca^{2+}$ + 15 mM $Na^{+}$, 50 mM $K^{+}$, 5 mM EGTA, 5 mM HEPES, I=0.133 N.

| -log $c_{Ca^{2+},free}$ | Total $c_{Ca^{2+}}$ [M] | pH |
|---|---|---|
| 4 | $5.10 \cdot 10^{-3}$ | 7.4 |
| 5 | $4.98 \cdot 10^{-3}$ | 7.4 |
| 6 | $4.71 \cdot 10^{-3}$ | 7.4 |
| 6.5 | $4.18 \cdot 10^{-3}$ | 7.4 |
| 7 | $3.09 \cdot 10^{-3}$ | 7.4 |
| 7.5 | $1.69 \cdot 10^{-3}$ | 7.4 |
| 7.7 | $1.21 \cdot 10^{-3}$ | 7.4 |
| 8.5 | $2.11 \cdot 10^{-3}$ | 8.0 |
| 9 | $2.73 \cdot 10^{-3}$ | 8.4 |
| 10 | $2.36 \cdot 10^{-3}$ | 9.0 |

Table C.3: $Ca^{2+}$ + 5 mM free $Mg^{2+}$, 50 mM $K^{+}$, 5 mM EGTA, 5 mM HEPES, I=0.083 N.

| -log $c_{Ca^{2+},free}$ | Total $c_{Ca^{2+}}$ [M] | Total $c_{Mg^{2+}}$ [M] | pH |
|---|---|---|---|
| 4 | $5.10 \cdot 10^{-3}$ | $5.00 \cdot 10^{-3}$ | 7.4 |
| 5 | $4.97 \cdot 10^{-3}$ | $5.02 \cdot 10^{-3}$ | 7.4 |
| 6 | $4.59 \cdot 10^{-3}$ | $5.16 \cdot 10^{-3}$ | 7.4 |
| 6.5 | $3.90 \cdot 10^{-3}$ | $5.43 \cdot 10^{-3}$ | 7.4 |
| 7 | $2.65 \cdot 10^{-3}$ | $5.92 \cdot 10^{-3}$ | 7.4 |
| 7.5 | $1.31 \cdot 10^{-3}$ | $6.44 \cdot 10^{-3}$ | 7.4 |
| 7.7 | $9.20 \cdot 10^{-4}$ | $6.59 \cdot 10^{-3}$ | 7.4 |
| 8.5 | $6.21 \cdot 10^{-4}$ | $8.65 \cdot 10^{-3}$ | 8.0 |
| 9 | $2.94 \cdot 10^{-4}$ | $9.50 \cdot 10^{-3}$ | 8.4 |
| 10 | $3.60 \cdot 10^{-5}$ | $9.93 \cdot 10^{-3}$ | 9.0 |

# Publications

## List of publications

Guenat OT, Generelli S, Dadras M, Berdondini L, de Rooij NF and Koudelka-Hep M. Generic technological platform for microfabricating silicon nitride micro- and nanopipette arrays, *J. Micromech. Microeng.*, 15:2372-2378, 2005.

Berdondini L, Generelli S, Kraus T, Guenat OT, Koster S, Linder V, Koudelka-Hep M and de Rooij NF. Microfabricated platforms for the study of neuronal and cellular networks, *J. Phys. Conf. Series*, 34:1-6, 2006.

Guenat OT, Generelli S, de Rooij NF, Koudelka-Hep M, Berthiaume F and Yarmush MT. Development of an array of ion-selective microelectrodes aimed for the monitoring of extracellular ionic activities, *Anal. Chem.*, 78:7453-7460, 2006.

Generelli S, Jacquemart R, Jolicoeur M, Koudelka-Hep M and Guenat OT. Potentiometric platform for the quantification of cellular potassium efflux, submitted.

# Contributions to conferences

Guenat OT, Berdondini L, Generelli S, de Rooij NF and Koudelka-Hep M. Microsystems for bioanalytical applications, 19th Seminar in Pharmaceutical Sciences, Zermatt, Switzerland, 1.10.2004. Oral presentation (invited).

Guenat OT, Generelli S, Clerc P-A, de Rooij NF, Koudelka-Hep M, Berthiaume F and Yarmush ML. Development of a platform for microscale monitoring of cell function and differentiation, 3rd Int. IEEE-EMBS Special Topic Conference on Microtechnologies in Medicine and Biology, Oahu, Hawaii, USA, 12-14.5.2005. Oral presentation.

Generelli S, Guenat OT, Berdondini L, van der Wal PD, Dadras M, de Rooij NF and Koudelka-Hep M, Microfabrication of $Si_XN_Y$ micropipettes for biochemical applications, Mátrafüred 2005, International Conference on Electrochemical Sensors, Mátrafüred, Hungary, 13-18.11.2005. Poster presentation.

de Rooij NF, Berdondini L, Generelli S, Kraus T, Guenat OT, Koster S, Linder V and Koudelka-Hep M. Microfabricated platforms for the study of neuronal and cellular networks, International MEMS Conference 2006, Singapore, Singapore, 9-12.5.2006. Oral presentation and extended abstract in: J. Phys. Conf. Series, vol. 34, 1-6.

Guenat OT, Generelli S, de Rooij NF, Koudelka-Hep M, Berthiaume F and Yarmush ML. Development of a platform for the monitoring of extracellular ionic activities, NanoBio Europe 2006, Grenoble, France, 14-16.6.2006. Oral presentation.

Guenat OT, Generelli S, de Rooij NF, Koudelka-Hep M, Berthiaume F and Yarmush ML. Development of a platform for the monitoring of extracellular ionic activities, 1st Annual Conf. Methods in Bioengineering, MIT, Cambridge, USA, 17-18.7.2006. Poster presentation.

Generelli S, Guenat OT, van der Wal PD, de Rooij NF and Koudelka-Hep M, Micropipette-based $K^+$ and $Ca^{2+}$ selective electrodes, 11th International Meeting on Chemical Sensors, Brescia, Italy, 16-19.7.2006. Oral presentation.

Guenat OT, Generelli S, de Rooij NF, Koudelka-Hep M, Berthiaume F and Yarmush ML. Development of a platform for the monitoring of extracellular ionic activities, AiChE06 Annual Meeting, San Francisco, USA, 12-17.11.2006. Oral presentation.

Generelli S, Guenat OT, van der Wal PD, de Rooij NF and Koudelka-Hep M. Potassium and calcium-selective microelectrode arrays, Pittcon 2007, Chicago, USA, 25.2-2.3.2007. Poster presentation.

Generelli S, Guenat OT, de Rooij NF, Koudelka-Hep M, Berthiaume F and Yarmush ML. Development of a platform for the monitoring of extracellular ionic activities, RQMP Annual Meeting, Montral, Canada, 14.5.2007. Poster presentation.

Generelli S, Miville-Godin C, Thomas M, St.Georges A and Guenat OT, Functionalized microfluidic platforms for cell culture, NAMIS International Autumn School 2007, Tokyo, Japan, 1-5.10.2007. Poster presentation.

Generelli S, Berthiaume F, Yarmush ML, Jolicoeur M, Koudelka-Hep M and Guenat OT, Microfluidic toxicological platform for the monitoring of extracellular ionic activities, MicroTAS 2007, Paris, France, 11-20.10.2007. Poster presentation.

Generelli S, Miville-Godin C, Thomas M, St.Georges A and Guenat OT. Functionalized microfluidic platforms for cell culture, ECS Canadian Section Fall Symposium, Electrochemistry in Biomedical Engineering and Biotechnology, Montral, Canada, 3.11.2007. Poster presentation.

Generelli S, Berdondini L, Imfeld K, Bornat Y, van der Wal PD, Guenat OT and Koudelka-Hep M. Microarray-based neurointerfaces, IV World Congress on Biomimetics, Artificial Muscles and Nano-Bio 2007, Torre Pacheco, Spain, 6-9.11.2007. invited oral presentation.

# Acknowledgements

I would like to thank

Prof. Milena Koudelka-Hep for her scientific guidance and for the freedom she gave me in carrying out this work.

Prof. Nico de Rooij, for the opportunity to work in his research group.

Prof. Olivier Guenat, for so many reasons, but especially for his endless enthousiasm.

Prof. Jean-Franǫis Dufour and Dr. Peter van der Wal for accepting the co-examination of this doctoral thesis and for their scientific (and moral) support during all the project.

Rana Afshar, Karin Schmidt, Prof. Stephan Rohr, Gaetan Boulard, Luke MacQueen, for their collaboration during the project.

The Swiss National Science Foundation (project nr. 205321-103961), for the financial support of the project.

The other BioMEMS group members in Neuchâtel Dr. Luca Berdondini, Dr. Anna-Maria Spehar, Olivier Frey, and in Montréal Caroline Miville-Godin, Maryline Thomas, Dr. Benyounes Bouabdallaoui.

The COMLAB technical staff Edith Millotte, Sylviane Pochon, Nicole Hegelbach, Sabina Jenny, Gianni Mondin, Pierre-André Clerc, Giovanni Bergonzi, Rémy Fournier, Stéphane Ischer, Sylvain Jeanneret, Eduardo Santoli, José Vaquera. Claudio Novelli for his absolutely necessary technical support. Karine Frossard and Florence Rohrbach for their secretarial work and their kindness.

The best office colleagues I could have, Mireille Leboeuf and Dr. Massoud Dadras, with his "Massoudian humor", for their encouragement.

The nine o′clock coffee team, and the Lausanne-Neuchâtel train friends, especially Alexandra Homsy, Arianna and Mattia Bertschi, Jérôme Courbat, Remo Kaempfer.

Everyone in the SAMLab group, and also Isabella Dioli, Diego Dioli, Feride Cengelli, Daniela Silvano, Stéphane Bedwani for their friendship.

And Claudio Valerio for his patience and support.